PHOTOGRAPHIC FILM AND ITS INTERACTION WITH LIGHT

DETECTION OF DUST AND SCRATCHES FOR IMAGE RESTORATION

Inauguraldissertation

zur

Erlangung der Würde eines Doktors der Philosophie
vorgelegt der
Philosophisch-Naturwissenschaftlichen Fakultät
der Universität Basel

von

Giorgio Trumpy

aus Italien

Basel, 2013

Genehmigt von der Philosophisch-Naturwissenschaftlichen Fakultät auf Antrag von

- Prof. John P. Maier
- Prof. Rudolf Gschwind
- Prof. Sabine Süsstrunk

Basel, den 17. September 2013

Prof. Jörg Schibler

(Dekan)

Attribution-Noncommercial-No Derivative Works 2.5 Switzerland

You are free:

to Share — to copy, distribute and transmit the work

Under the following conditions:

Attribution. You must attribute the work in the manner specified by the author or licensor (but not in any way that suggests that they endorse you or your use of the work).

Noncommercial. You may not use this work for commercial purposes.

No Derivative Works. You may not alter, transform, or build upon this work.

- For any reuse or distribution, you must make clear to others the license terms of this work. The best way to do this is with a link to this web page.
- Any of the above conditions can be waived if you get permission from the copyright holder.
- Nothing in this license impairs or restricts the author's moral rights.

Your fair dealing and other rights are in no way affected by the above.

This is a human-readable summary of the Legal Code (the full license) available in German:
http://creativecommons.org/licenses/by-nc-nd/2.5/ch/legalcode.de

Disclaimer:
The Commons Deed is not a license. It is simply a handy reference for understanding the Legal Code (the full license) — it is a human-readable expression of some of its key terms. Think of it as the user-friendly interface to the Legal Code beneath. This Deed itself has no legal value, and its contents do not appear in the actual license. Creative Commons is not a law firm and does not provide legal services. Distributing of, displaying of, or linking to this Commons Deed does not create an attorney-client relationship.

Quelle: http://creativecommons.org/licenses/by-nc-nd/2.5/ch/deed.en Datum: 3.4.2009

you see things because of scattering

Acknowledgements

I share the credit of my work with the following people.

Rudolf Gschwind, mover of the project, and the staff of the *Digital Humanities Lab - University of Basel (ex- Imaging & Media Lab)*: Andreas Wassmer, who developed the software framework SAFRAN, Elias Kreyenbühl, Lukas Rosenthaler, Peter Fornaro, Tobias Schweizer, Ivan Subotic, André Kilchenmann and Alexandra Tschakert. Sabine Süsstrunk of the *Images and Visual Representation Group - EPFL*, partner of the project, together with Wojciech Makowiecki and Dominic Rüfenacht. John Paul Maier of the *Department of Chemistry - University of Basel*. James M. Reilly and Jean-Louis Bigourdan and the staff of the *Image Permanence Institute* in Rochester (NY). Kristina Kersels of the *Association of Moving Image Archivists* in Los Angeles. Joakim Reuteler of the *Center for Microscopy and Image Analysis - University of Zurich*. David Landolf and Mani Morgenthaler of the *Lichtspiel kinemathek* in Bern. Barbara Flückiger of the *Institute of Cinema Studies - University of Zurich*. David Pfluger *@saeure.ch*. Thomas Öhler of the *Le bon film kinemathek* in Basel. Reto Kromer of *reto.ch* in Écublens (CH-VD). Alessandro Rizzi, Carinna Parraman and the whole *CREATE* group. Mauro Bacci, Marcello Picollo and Franco Lotti of the *Institute of Applied Physics - CNR* in Florence. Alfredo Aldrovandi of the *Opificio delle Pietre Dure* in Florence. Elena Tammaccaro of *L'Immagine Ritrovata - Cineteca di Bologna*. Jürg Blaser of the *Zentrum elektronische Medien* in Bern. Peter Nussbaum and Aditya Suneel Sole of the the *Norwegian Colour and Visual Computing Laboratory* in Gjøvik. Laurence Stoll and Dan Tatut of *Marquise Technologies* in Gland (CH-VD). Lindsay Buffington.

Summary

A considerable portion of the cultural heritage of the last century is constituted by images impressed on photographic film, the majority of which are frames of motion picture films. At present time, a large part of this heritage is at risk of being lost; this loss would break historical links, which are important for the economic, social and cultural development of future generations. The current 'digital revolution' has already produced drastic changes in image production technology, and 'classical photography' is disappearing; this leaves the field open for new powerful technical opportunities, but, at the same time, poses huge dilemmas for long-term archiving [1]. The demise of classical photography is taking place in a precipitous and often ruinous way, causing several historied companies to go bankrupt [2, 3].

Today's information society needs efficient and economic solutions for the digitization of this photographic heritage. The costs of the processes determine the amount of films that can be digitized, restored and made available to the community [4].

Research about digital movie restoration began around 1990, when it became possible to scan movie films in 2K resolution, thus providing high enough quality for the digitized images of a 35mm movie film. The first full-length motion picture film was digitally restored in 1993 [5]. In recent years, several research projects about digital movie restoration have been undertaken. The research-project AURORA [6] concentrated on the real-time restoration of image defects, which are typical for old videotapes; the main partners were the INA (Institut National d'Audiovisuelle, Paris), BBC-London and Snell & Wilcox, UK. PRESTO (Preservation Technology for European Archives) and the subsequent project PRESTOSPACE [7], within European Commission 6th Framework Programme for Research, provided technical solutions and integrated systems for a complete digital preservation of all kinds of audiovisual collections.

Audiovisual archiving is a complex and multi-disciplinary domain including such diverse fields as chemistry, physics, imaging technology, signal processing, robotics, artificial intelligence and semantic interpretation. These EU-projects bring together participants including archive owners, broadcasters, research centers from archive institutions, general research centers and universities, industries, and international non-profit institutions.

An important result of the movie restoration research is the development of new software: e.g. FRAME and its further development DIAMANT. Several early movies were reconstructed using DIAMANT, the most famous being Metropolis in 2001 [8]. LIMELIGHT was a software project [9] that was further developed by the University of La Rochelle to become RETOUCHE [10].

In the period of 2010-2013, the Swiss National Science Foundation financed the project 'Dust BW: Detection of dust and scratches on photographic silver-halide (black/white) material by polarized dark-field illumination' [11, 12, 13, 14, 15, 16]. Partner of the project were

the Imaging & Media Lab of the University of Basel and the Audiovisual Communications Laboratory School of the EPFL (Ecole Polytechnique Fédérale de Lausanne). The present thesis reports the results of this research project.

Several factors are responsible for the deterioration of photographic material; we will only focus on dust and scratches. Different methods have been adopted up to now for the automatic detection of dust and scratches; each method has pros and cons, and a limited field of effectiveness. Infrared radiation (e.g. Digital ICE) and the spatio-temporal image analysis are among the most effective methods, although they have their limits. The infrared radiation only works for dye-based material and the spatio-temporal image analysis is not applicable for still images. The spatio-temporal image analysis is also limited due to motion in the scene and it is not effective for defects appearing in sequences spanning more than one frame (e.g. vertical scratches and lens dust). This thesis presents a comprehensive range of methods for optical flaw detection, applicable on any type of photographic film (both silver-based and dye-based material, as well as still images and moving images). It also presents innovative methods that combine different optical techniques and computational photography.

This thesis begins by describing the structure of a processed photographic film, analyzing its constitutive elements layer by layer (Chap. 1). Afterwards, we will provide a list of the most common types of decay affecting the photographic film, classified on the basis of the layer that is primarily affected (Chap. 2). This will be followed by a summary of the state-of-the-art strategies and solutions for the restoration of local flaws (Chap. 3). The analysis of the interaction between light and photographic film (Chap. 4) provides the scientific framework needed to understand the optical phenomena involved in the experiments. The following chapter (Chap. 5) explains the phenomena and the techniques involved in imaging photographic film. Chapter 6 surveys the optical methods available for flaw detection on any type of photographic transparency, including innovative solutions. The successive chapter (Chap. 7) defines the procedure we adopted for the numerical evaluation of the performances of the methods analyzed in the experiments. Prior to the conclusion chapter, the thesis finally addresses the experimental analysis, identifying the best parameters for the proposed methods (Chap. 8) and comparing the innovative methods with the most effective traditional ones (Chap. 9).

Contents

Chapter 1

Structure of photographic film

The notion of photography in a classical sense is inseparably related to the exceptional light sensitivity of silver halides. First attempts to use light sensitive substances to produce images were made before 1800, but photography is essentially a 19^{th} century technology [17]. It was only in the late 1800s that silver salts were suspended in gelatin, thus allowing photographic material to be produced industrially. Soon after, a flexible, transparent material became available to act as a support for the silver-gelatin emulsion. The Eastman Dry Plate and Film Company introduced rolls and sheets of clear, flexible nitrocellulose in 1889 [18]. Thanks to this innovation, photographic material could be wound on reels, granting it a great flexibility of use and leading to the invention of the motion picture: a high-rate sequence of photographs reproducing motion.

A succession of events, summarizable as *exposure* and *processing*, allow a photographic film to record an image, which can then be seen with backlighting [19]. During the manufacture of an emulsion, electron traps are formed within silver halide crystals by introducing impurities into the crystal lattice. The emulsion is kept in darkness until, during shooting with a camera, it is briefly exposed to light; in consequence, certain electrons acquire from photons the energy required to reach the conduction band, so that they can move freely within the lattice until they are captured by the electron traps. The negative charges that are built attract positive silver ions from the lattice and form a minute metallic silver deposit. The distribution of silver deposits constitutes the 'embryonic' *latent image*. The exposed photosensitive material is then immersed in the *developer*; this is a reducing medium that selectively reduces the silver halide crystals that contain metallic deposits and amplifies the latent image, thus making it visible.

In case of chromogenic processes, a chemical reaction known as *chromogenic development* produces a dye image [20]. As the developer reduces the exposed silver halide to form metallic silver, the developer itself is oxidized by the reaction; the developer can now combine with another chemical substance known as *coupler*, which is present in the emulsion. The product

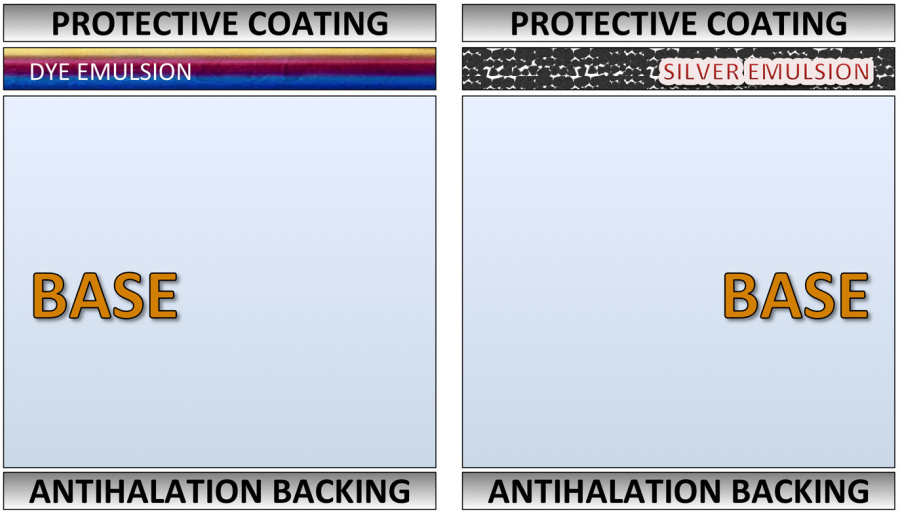

Figure 1.0.1: Sections of processed photographic films: a color film on the left and a black-and-white film on the right

of this secondary reaction is a colored compound, the dye, which is produced in proportion to the amount of silver developed. The black-and-white silver image is then removed by *bleaching* and the film finally carries a color image consisting only of organic dyes. Other methods have been developed to obtain color photographs on film (dye diffusion-transfer, silver dye-bleach, etc.), but the body of color photography on film is mainly constituted by chromogenic dyes [21].

Irrespective of the silver- or dye-nature of the image, the final step in the photographic processing of film is the *fixing*; the fixer stabilizes the image, removing the unexposed silver halide remaining on the photographic film, thus making it insensitive to further light.

The present thesis will now focus on the photographic film after the process of image formation: a "processed film".

Layers of processed film

Figure 1.0.1 sketches a typical layered section of a black-and-white photographic film; in the following paragraphs the heterogeneous structure of a processed photographic film is described layer by layer.

Emulsion

The fundamental layer is the emulsion, where the photographic image is impressed; its thickness is generally around $10\mu m$. The emulsion of a processed film consists of a dispersion of image particles in a transparent and flexible colloidal medium; thanks to its ideal properties, *gelatin* is by far the most common medium for classical photography. The image particles allow for the attenuance of visible light, which is the fundamental phenomenon of photography.

Photographic images may be formed by silver particles or dye clouds. Usually, silver particles are employed in black-and-white film, while dye clouds are employed in color film; however, chromogenic black-and-white film also exists. In color film, the gelatin emulsion is divided into separate layers containing cyan, magenta and yellow dyes. The size of image particles is variable, depending on the type of film and on its exposure and development; usually, silver particles span in size between $0.2 - 2.0\mu m$, while color dye clouds range from $10\mu m$ to $15\mu m$ [22].

Film base

The film base constitutes 90% of the thickness of the film, and it acts as a support for the emulsion. This layer has to be transparent, mechanically strong and flexible.

When motion picture film was introduced in the 1890s, *cellulose nitrate* was the only available transparent plastic durable enough for movie cameras and projectors. It was discontinued in the 1950s because it was highly flammable and caused several fires in the early decades of cinema.

Manufacturers found a safe substitute for cellulose nitrate by exploring plastics in the *cellulose acetate* family. Beginning in 1909, a number of new acetate bases were introduced, starting with *cellulose diacetate*, followed by *cellulose acetate propionate* and *cellulose acetate butyrate* in the 1930s, and, finally, by *cellulose triacetate* in the late 1940s. Although they are safe, the cellulose acetates do have stability problems. The deterioration of cellulose acetate is autocatalytic, like that of cellulose nitrate; once deterioration has begun the products of degradation induce further deterioration (sec. 2.1).

In the mid 1950s Kodak began selling a new type of safety film made of polyester (*Estar*). Polyester bases are made in an entirely different manner; these are manufactured by extruding the heated polyester material through a slot, stretching it in a longitudinal direction. This orients the molecules of plastic, yielding a base material that is free from stresses and strains, and that has very good dimensional stability. However, polyester films also have a greater tendency to generate static electricity and this makes them more susceptible to picking up dust and fibers from the atmosphere. They are also more susceptible to scratching.

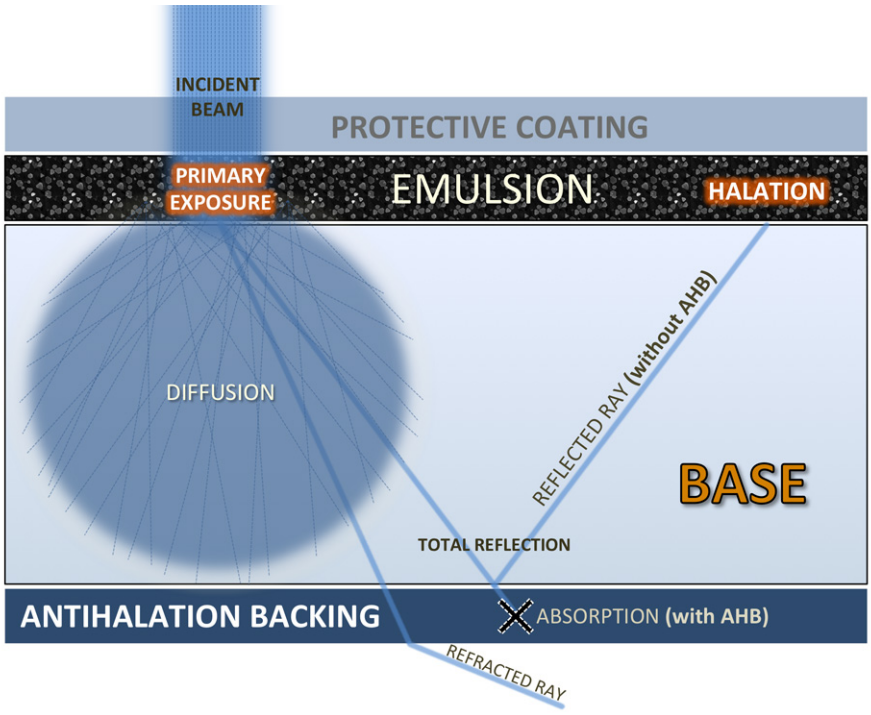

Figure 1.0.2: The mechanism of halation and its prevention through antihalation backing (AHB)

Protective coating

The top layer of the film is a protective coating (*supercoat*). The purpose of this clear layer of hardened gelatin is to protect the emulsion from damage during its passage through the camera.

Antihalation backing

An antihalation layer is often present on photographic films. During exposure (Fig. 1.0.2), light penetrates through the emulsion layer into the base; the silver halide crystals of the emulsion cause scattering phenomena and the incident beam is diffused. At the base-air interface, the rays that are deviated at an angle greater than the '*critical angle*' are reflected back towards the emulsion, causing a secondary exposure (*halation*). This secondary exposure appears as a glow around bright objects (Fig. 1.0.3).

The antihalation layer is a dyed gelatin coating on the film base that absorbs light and minimizes this reflection. The dye is removed during processing and the layer becomes transparent. Following processing, the thickness of the gelatin layer that remains on the

Figure 1.0.3: Halation (image source: Digital Humanities Lab)

backside of the film is similar to the thickness of the emulsion layer on the front. Both the emulsion and the backing can soak up moisture and dilate. The presence of this second gelatin layer helps the film to stay flatter than if the gelatin was only applied to one side; this useful effect is called '*anticurl*'.

Chapter 2

Decay of photographic film

Photographic film is not made to last; created on perishable plastic, film decays with the passage of time if it is not properly stored. The present chapter reports some of the most common types of decay affecting photographic film, classified by the layer that is primarily affected. Dust and scratches, the main focus of the present work, are described separately as they may occur indiscriminately on both sides of the film.

2.1 Base decay

Nitrate decay

Nitrate film degrades because of its chemistry; its decay can be retarded by improving storage but cannot be in any way reversed [23]. When the deterioration is initiated, the successive autocatalytic phase promotes a relentless deterioration of the cellulose polymer, the softening of the gelatin and the oxidation of the silver. As the exothermic process evolves, the metal cans in which motion picture films are often stored close in acidity and heat, further speeding up the deterioration process. According to the stage reached, the following detrimental effects can be observed, and in this order: image fading, brownish discoloration of emulsion (Fig. 2.1.1), the emulsion becomes sticky, the formation of blisters with gas bubbles, the film congeals into a solid mass, and lastly, the film disintegrates into brownish powder.

Vinegar syndrome

The term "*vinegar syndrome*" refers to a series of phenomena occurring on acetate film during its decay [24]. Acetic acid is released during the initial acetate base deterioration,

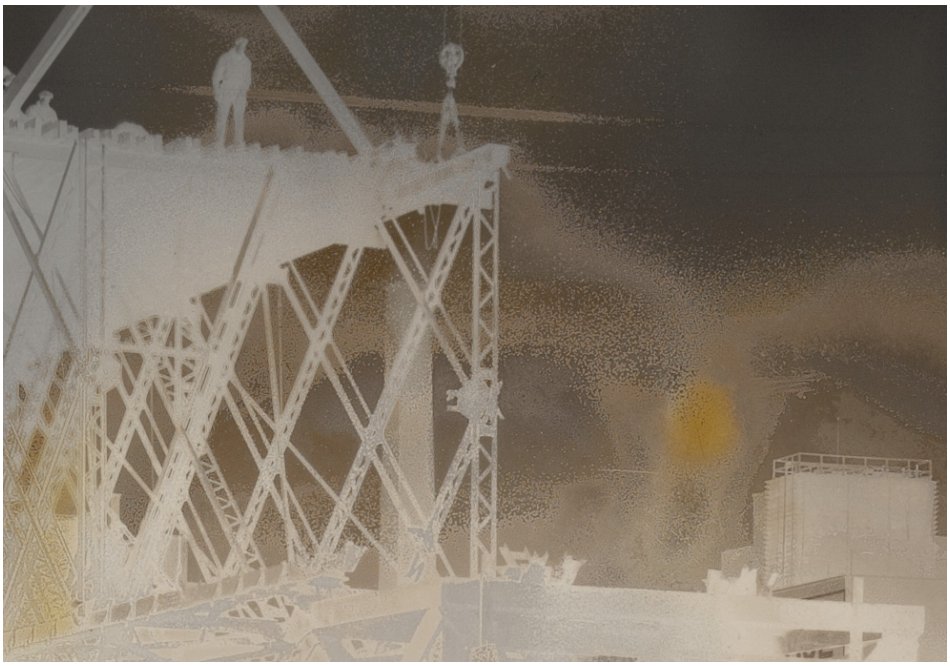

Figure 2.1.1: Nitrate decay (sample source: Image Permanence Institute - digitized by the author)

leading to the characteristic vinegar odor. The acidic environment encourages the polymer chains of cellulose acetate to break down and, in consequence, the film becomes brittle. Shrinkage also occurs during this process. As the acetate base shrinks, the gelatin separates from its base and wavy grooves appear; this effect is known as "*channeling*" (Fig. 2.1.2).

A sign of an advanced stage of vinegar syndrome is the formation of crystalline deposits or liquid-filled bubbles; the *plasticizers*, additives to the plastic base, become incompatible with the cellulose acetate and ooze out on the surface, where they then remain between the base and the emulsion as clumps of crystals or bubbles (Fig. 2.1.3).

2.2 Emulsion decay

Mold and insects

Gelatin is at risk of decay because its proteic nature makes it attractive for organisms. A film stored in humid conditions can become a host for mold, mildew, and fungus [23]. Generally, the organisms start their attack from the outside edge and make their way into the film roll. These biological agents can cause significant damage to the emulsion. The growth initially appears in the form of matte-white spots and eventually grows into a web-like pattern.

Figure 2.1.2: Channeling (sample source: Image Permanence Institute - digitized by the author)

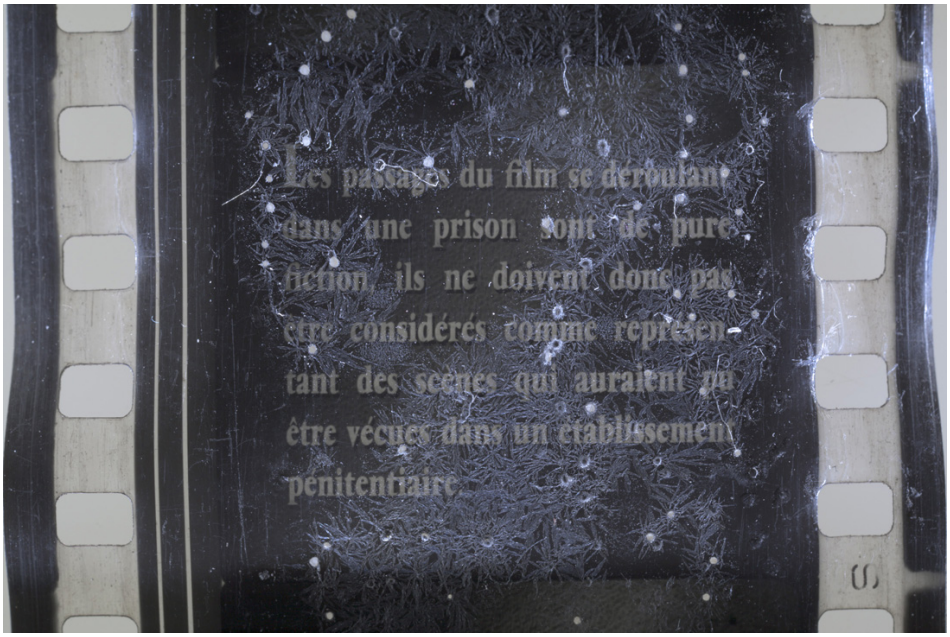

Figure 2.1.3: Plasticizer oozing (sample source: Image Permanence Institute - digitized by the author)

Figure 2.2.1: Ferrotyping (sample source: Image Permanence Institute - digitized by the author)

Insects also find gelatin to be a good food source. The marks they leave look like irregular holes or channels, and are wider than mold marks. Cleaning the film and then moving it to a cold and dry environment can help to stop the invasion.

Ferrotyping

The term "*ferrotyping*" originally refers to an voluntary treatment carried out on prints to give them a gloss [17]. In this technique, the photograph is dipped into an aqueous solution and then squeegeed onto a very smooth surface, upon which the photograph dries on contact.

The term is also used for an involuntary change in the optical characteristics of the gelatin emulsion of a film. When the film undergoes fluctuations in humidity and is in close contact with a very smooth surface, the emulsion can gain gloss (Fig. 2.2.1). The change in glossiness is due to the diminishment of surface irregularities on a microscopic level.

However, ferrotyping does not severely degrade a film since its effects are not visually remarkable when the film is illuminated in transmission (which is actually its proper utilization).

Figure 2.2.2: Silver mirroring: the emulsion side (left) and the base side (right) (sample source: Image Permanence Institute - digitized by the author)

Silver mirroring

Silver mirroring is a bluish metallic sheen that appears on the emulsion surface of silver-based photographs as a result of aging. Mirroring can be caused by noxious atmospheric gases (e.g. *sulfur dioxide*, oxides of nitrogen, *ozone*) or compounds present in the filing enclosures in contact with the photograph [25]. The widely accepted model for silver mirroring is a three-step process in which the silver in the emulsion is oxidized, its ions migrate on the emulsion surface, and they reduce into metallic silver again. The result is an increase in the reflective component of the emulsion side of the photograph.

This increment of reflection is proportional to the amount of silver present at the specific point; therefore, in certain conditions, the image impressed becomes visible in reflection, but its brightness is inverted (Fig. 2.2.2). In fact, a film affected by silver mirroring is very reflective where the silver is highly concentrated, and that point appears bright in reflection. However, as the high silver concentration of the same point causes low transmission, little light reaches the observer in a transmission visualization.

In spite of this, the transmission component of the film remains dominant, and thus the effect of mirroring is minor when the film is illuminated in transmission. Hence, the degradation of the photographic image is not severe, since its proper use in not compromised.

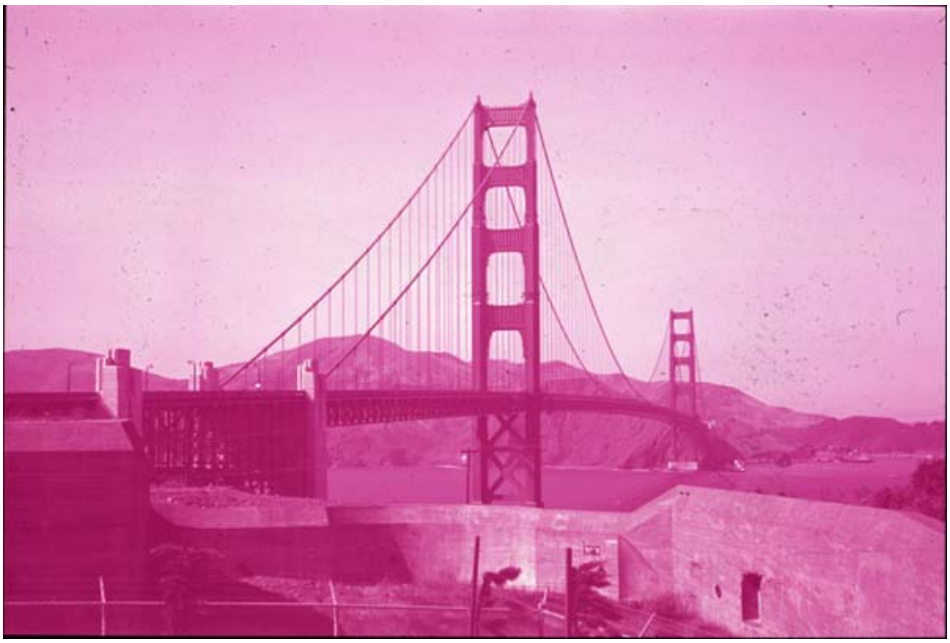

Figure 2.2.3: Typical purplish cast of a faded slide (image source: Digital Humanities Lab)

Dye fading

The dyes of photographic film have poor stability when exposed to light, chemicals, heat and humidity. As a consequence, the color of photographs deteriorates with time [26]. Many older films have taken on a distinct purplish cast, caused by the rapid fading of the cyan and yellow image dyes (Fig. 2.2.3).

Negatives, interpositives and prints are all affected in the same way. While earlier generations of color films would fade in just a few years when kept at room temperature, modern films are more stable, with significant fading will occur in about 40 years at standard room conditions [21].

2.3 Dust and scratches

Dust and scratches, although two completely different phenomena, are often categorized together. The reason of this connection is, at least, twofold: the cause of both dust and scratches is mechanical (it involves contact with foreign matter and movement of solid material on a macroscopic scale) and the effect of both of them is small local alterations of image brightness (Fig. 2.3.1).

From the creation to the utilization of a photographic film, during all of the stages of its life, mechanical movement is fundamental and therefore, mechanical damage is inevitable. Films

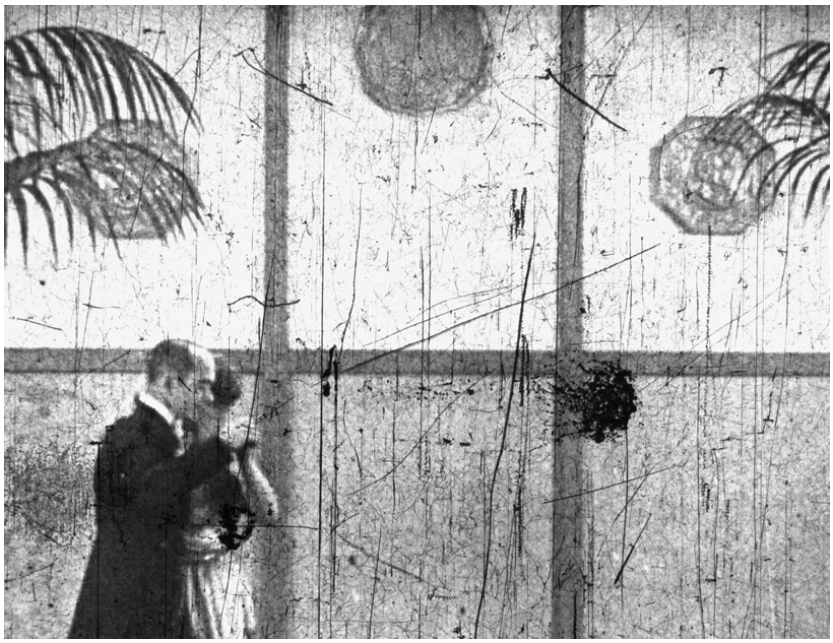

Figure 2.3.1: The appearance of dirt, dust and scratches on a photographic film (sample source: David Pfluger - digitized by the author)

are handled, transported through rollers and sprockets, pulled and blocked, pressed and bent, spooled and unspooled; during all of these actions, the film may pick up dust, dirt, scratches, and abrasions that blemish the image it carries. The visualization of a photographic image generally entails a large magnification and in turn, the flaws are magnified together with the image. For this reason, even small blemishes can have a strong impact on the photographic image.

Dust and scratches are two different types of irregularity of film surfaces (Fig. 2.3.2). "*Dust*" can refer to any small foreign body that is accidentally lying on the film surface; generally, when the foreign material adheres to the surface, the term "*dirt*" is used. When dust or dirt are present on the emulsion side of the film, they are almost in contact with the image particles. In contrast, when dust or dirt lie on the base side, the transparent base is holding a distance between them and the emulsion. On the other hand, in the case of a scratch, the film material is missing. Scratches can be only superficial or they may penetrate the emulsion layer, completely obliterating parts of the image impressed in it; a deep scratch on the emulsion side is likely to destroy the corresponding part of the photographic image.

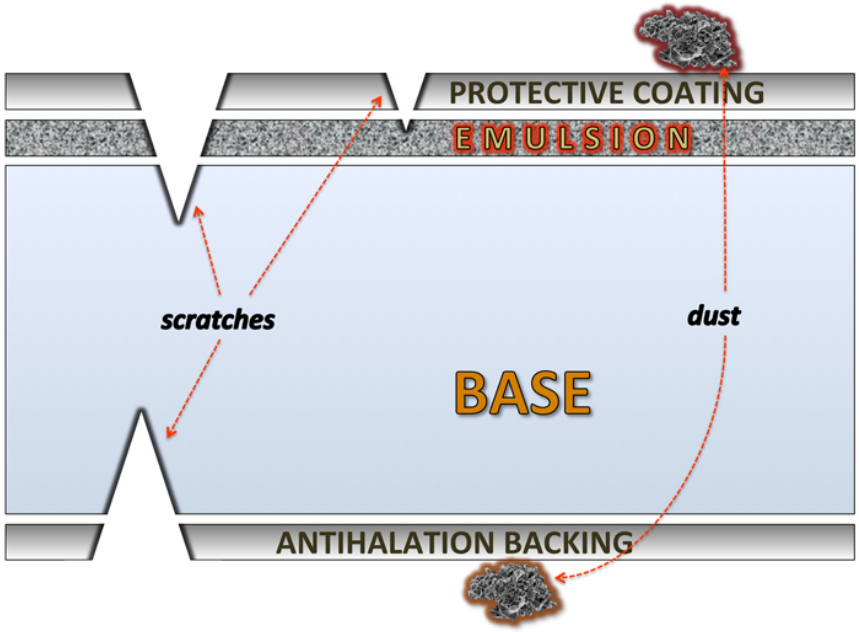

Figure 2.3.2: Dust and scratches on photographic film

Chapter 3

Restoration of local flaws in film

Two main courses of action can be taken by archivists and curators to preserve their photographic collections. It is essential to understand the functional context of a photograph, not considering it as a mere image, but rather as a 'document' [27]. In this respect, the preservation effort must also consider the material and the contextual features connected with the photograph; thus, the restoration has to focus on the physical integrity of the film (*object-oriented interventions*). On the other hand, the reproducibility intrinsic in photography has limited the importance of physical film as the focal object of the preservation effort, and has shifted the focus of this effort to its visual content (*content-oriented interventions*). The introduction of the negative/positive process transformed photographs from being unique items to being reproducible [28, 29], and the concept of 'original' became for film more flexible than other works of fine art (e.g. paintings). These characteristics led to a quite extensive applicability of digital restoration. in this respect, the preservation efforts are now focused on the image, and the film itself is considered to be simply a "*carrier*". The image can be copied onto a new support when the original is damaged.

3.1 Digital restoration

Digital restoration is the epitome of content-oriented restoration: it eliminates the appearance of degradation by processing the visual information (Fig. 3.1.1) acquired in digital form [30]. During the last years of innovation in digital imaging technologies, digital methods for the restoration of motion picture films have become more and more widespread [31, 32].

Prior to digital restoration, it is necessary to acquire the visual information of the original object; we refer to the product of this operation, which will be discussed extensively in Chapter 5, with the term '*digital reproduction*'. It is in the following step that the actual digital restoration takes place, as flaws are removed from the digital reproduction. If desired,

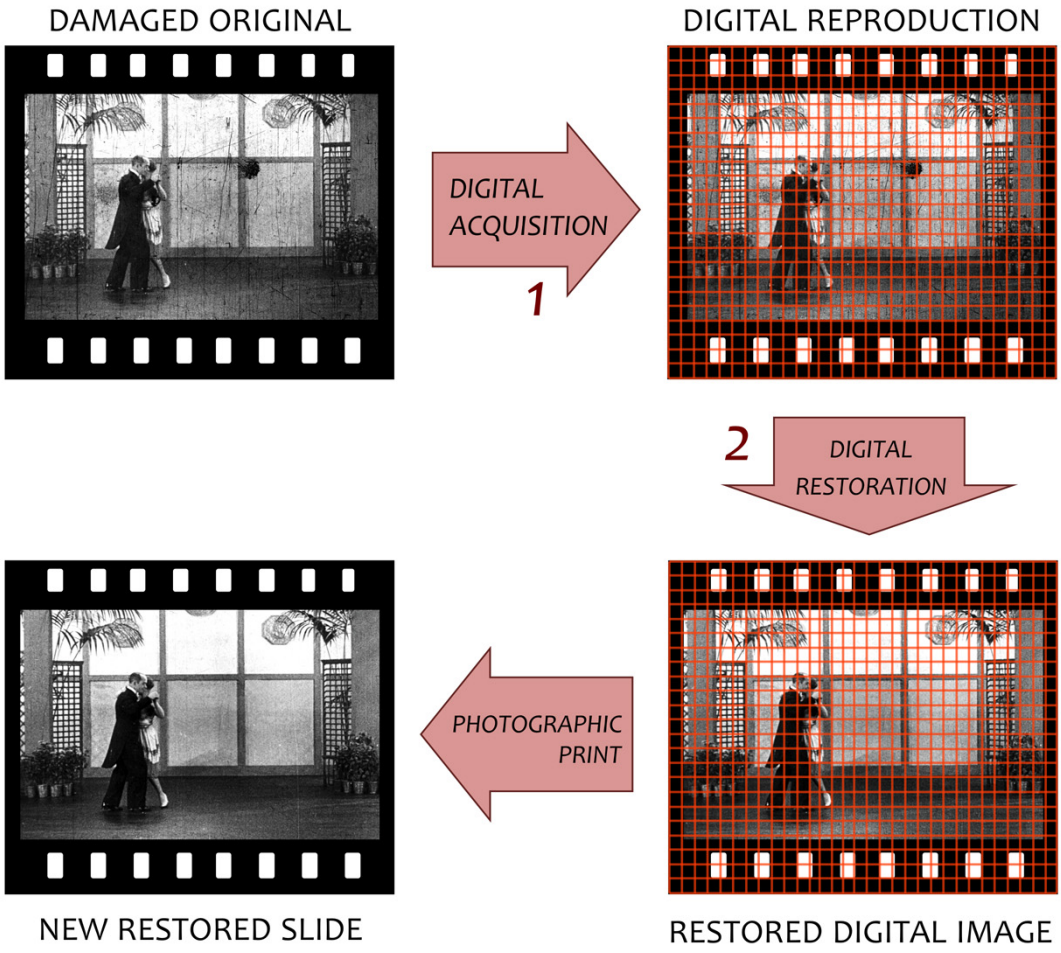

Figure 3.1.1: The two-step process of digital restoration and the subsequent print of the restored copy

the restored image can be newly printed on photographic film to create a restored copy of the original object.

The present work deals with dust, scratches and all other flaws of mechanical origin that appear as small local alterations of image brightness. The advanced solutions for this type of flaws are carried out in two stages: the detection stage, in which the flaws are pinpointed in the digital reproduction, and the reconstruction stage (*Inpainting*), in which the values of the pixels corresponding to the deteriorated parts of the image are changed, thus putting the restoration into effect.

Flaw detection

The detection of flaws can be carried out through an analysis of the digital reproduction (sec. 3.2.3), relying on the characteristics of the appearance of flaws (shape, border characteristics, etc.) or on temporal information. The main advantage of this approach is that it can be applied on previously digitized motion pictures, without the need to re-scan the film.

Alternatively, flaws can be detected by relying on physical evidence of the presence of foreign bodies or irregularities on the film (Chap. 6). This approach, sometimes called "*hardware-assisted*" or "*optical*", generally improves the performance of the restoration but requires a special setup to acquire a particular image. The principal drawback of the hardware-assisted methods arises in the case of flaws impressed in the new film during the process of copying. Copied flaws may be detectable by relying on morphological characteristics of their appearance, but, as they have become part of the photographic image of the emulsion, they are not detectable using an optical method. Copying a film on a new carrier is a preservation solution that has been used extensively for motion pictures, and as a result, copied flaws often occur.

The result of flaw detection can be directly used, or can be stored in the *Alpha channel*; skilled applications for digital restoration of movies carry out the reconstruction selectively, using the information contained in the Alpha channel.

Flaw detection is the core topic of the present work, and it will be addressed in detail in Chapter 6.

Inpainting

The term "*inpainting*" refers to the second operational step of digital restoration. At this point, the corrupted image data are corrected so that the final image appears more pleasing and visually plausible to an average observer; the criteria are based on psychophysics studies of the human visual system and image perception. Inpainting uses the information located

near the boundaries of the degraded regions; this information is used to restore continuous edges by connecting the truncated fragments together [33] and filling the lacunae by extending surrounding patterns [34]. The interventions have to adhere to the ethical principles of restoration, with respect for the content as cultural property [35].

3.2 Merchandised solutions for dust and scratches

In the following text, we report on the most important solutions for the removal of dust and scratches available on the market [36], considering both traditional and digital approaches. Each method has pros and cons, and a limited field of effectiveness. Section 3.2.1 describes the object-oriented interventions, while the rest of the following sections of the chapter describe the content-oriented interventions.

3.2.1 Object-oriented intervention

Dust is additional material on the film surface that can be removed from the photographic film. The utilization of compressed air combined with electrostatic discharge is often effective. Alternatively, *Particle Transfer Rollers* can be used. These cleaners use slightly sticky urethane coated rollers that the dust particles adhere to as the film is wound around them (Fig. 3.2.1).

These methods are not always very effective, especially when dirt is sticking to the surface of the film. In such cases, cleaning solvents can be used to promote the dissolution of dirt, although the halogenated hydrocarbons used (i.e. $3-bromo-1,1,1-trifluoropropane$, $perchlorethylene$, $1,1,1-trichloroethane$, $n-propylbromide$) are hazardous for humans and the environment, thus entailing complications.

The cleaning of the film of dust and dirt, together with the repair of tears, constitutes the preliminary step of any content-oriented restoration.

3.2.2 Wet-Gate

"*Wet-Gate*" is a technique that can be used during film printing, copying, or digital acquisition. Some film printers and film scanners are equipped with a Wet-Gate device (Fig. 3.2.2). The reproduction of the original film is created when it is immersed in perchloroethylene (*Perc*); this liquid fills the scratches and, since it has a refractive index close to that of the film base, light scattering is reduced. As a result, the scratches are less visible in the reproduced image of the film.

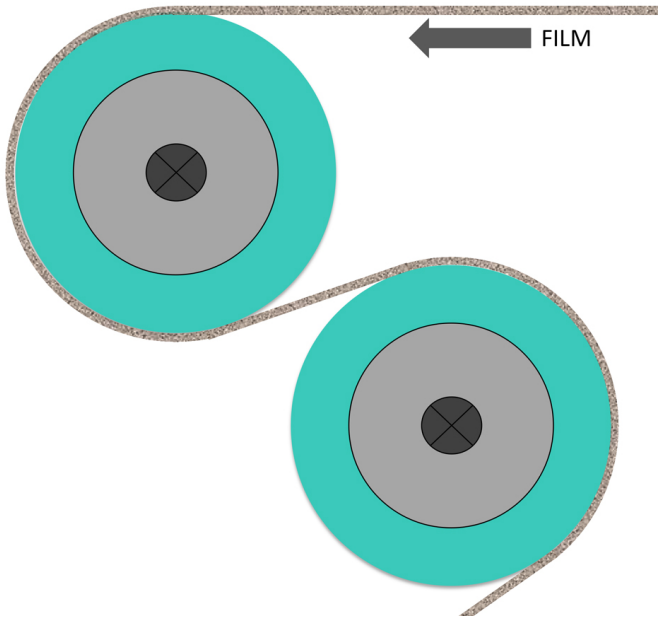

Figure 3.2.1: Particle Transfer Rollers

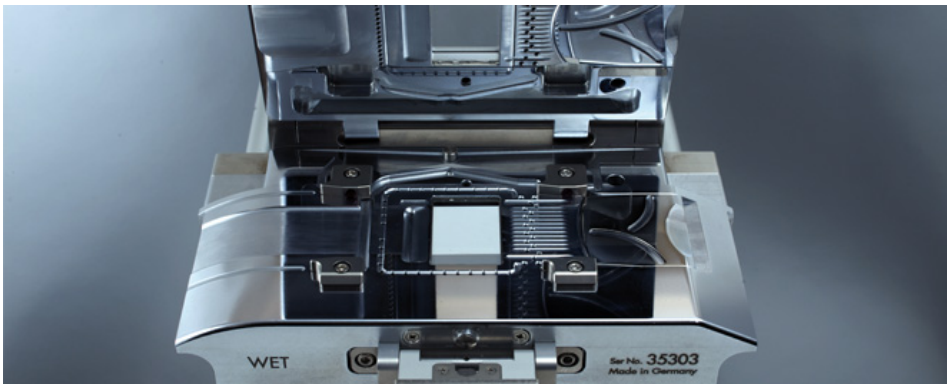

Figure 3.2.2: The Wet-Gate produced by the company ARRI (image from [37])

However, the method is not effective for dust, or for penetrating scratches that have completely removed the emulsion. Moreover, Perc is toxic and this creates complications in the restoration process.

3.2.3 Image analysis

Digital filters

In the removal of local flaws in a photographic film, the simplest way to automatically process a digital reproduction is by applying digital filters. One of the most frequently used digital filters for this purpose is the *median*: each pixel of the image is replaced with the median of neighboring pixels. This has a smoothing effect that removes some kinds of flaws, but it also affects the edges and may obliterate the fine details in the image.

Morphological analysis

A wide selection of sophisticated applications are available for repairing and retouching movie sequences and films in digital form (*Diamant*, *Furnace*, *PFClean*, *DaVinci Revival* etc.). These applications generally offer interactive semi-automatic tools and fully automatic functions. The reconstruction has a diversified action according to the information of the preventive flaw detection, relying on morphological analysis of the appearance of flaws. For example, dust grains are assumed to be small and to have a significant contrast with their background [30], while scratches are often vertical and are assumed to be long and narrow with sharp borders [38].

However, the morphological analysis of a digital reproduction cannot differentiate between flaws and image features with similar morphological characteristics. Hence, elements of the emulsion image can be erroneously obliterated and *digital artifacts* may appear.

Figure 3.2.3 shows an example of flaw removal based on morphological image analysis: the algorithm was successful in removing a fiber and some dust grains, but it also removed a rotor and the landing skids of the helicopter.

Spatio-temporal analysis

In the case of motion pictures, the timeline information provides another criterion for flaw detection based on image analysis [39, 40]. The illusion of movement is given by the slight differences between the contiguous frames of a movie (with the exception of scene cuts). Hence, an algorithm that can take advantage of the high correlation between adjacent frames has the potential to detect and remove dust grains, dirt spots and similar flaws that appear

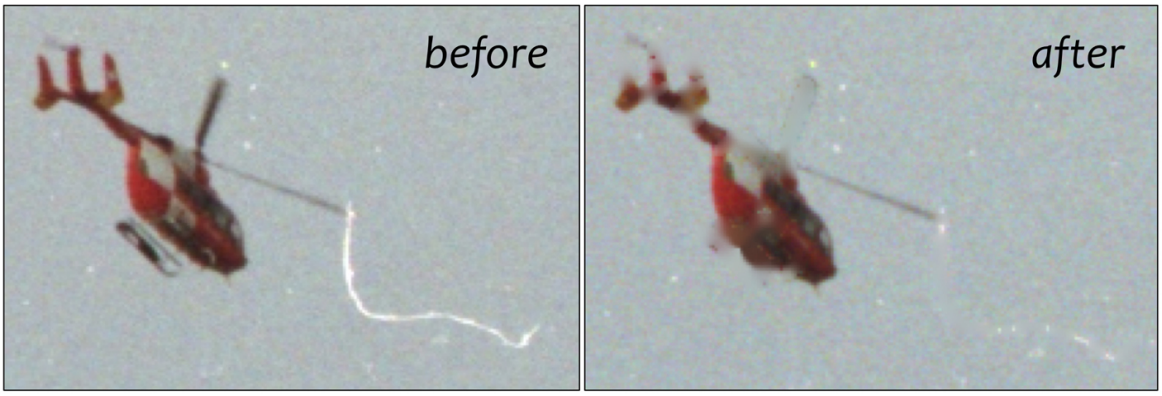

Figure 3.2.3: Digital artifacts resulting from a flaw removal tool based on morphological image analysis

on a single frame [30, 32]. Each movie frame is compared with its contiguous frames (see Fig. 3.2.4); when an element is present only on a frame t, and it is absent from the previous $t-1$ and the subsequent frame $t+1$ (in the same position or in a certain surrounding area), then it is considered as a flaw. In this case, the information of $t-1$ and $t+1$ frames can be used to fill the detected flaw and therefore, this method provides an effective solution for both detection and reconstruction.

Unfortunately, the design of a spatio-temporal restoration algorithm is made difficult by the motion of objects in the recorded scene. For example, an element of the scene can escape detection simply because, due to its fast movement, the positions of the element in the contiguous frames change considerably; therefore, the software does not recognize the element, erroneously considering it as a flaw. Therefore, in order to correct this, the algorithm needs to involve knowledge of the motion in the image sequence [41]. Moreover, spatio-temporal image analysis is not effective for all defects appearing in sequences over more than one frame (e.g. vertical scratches and lens dust).

Color analysis

In specific cases, the color information can be useful to detect dust, dirt and stains [42]. Digital reproduction of a black-and-white photographic film is characterized by being achromatic or having a specific color cast. The latter is particularly pronounced if the film underwent tinting or toning. If foreign bodies accidentally lying on the film surface have a specific color, and this color differs from the color cast of the film, then this difference can be a useful piece of information to detect these bodies.

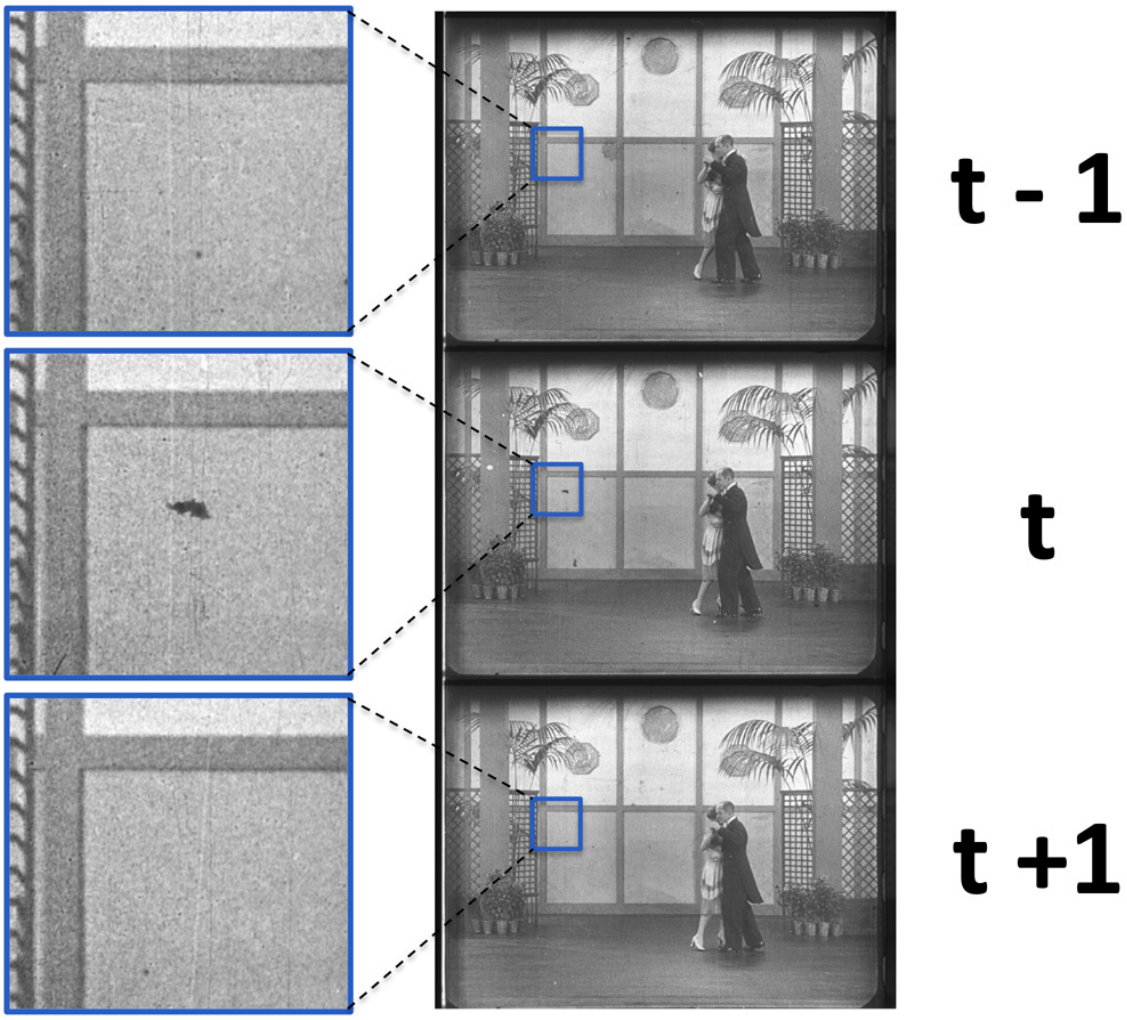

Figure 3.2.4: Flaw detection using a spatio-temporal restoration algorithm

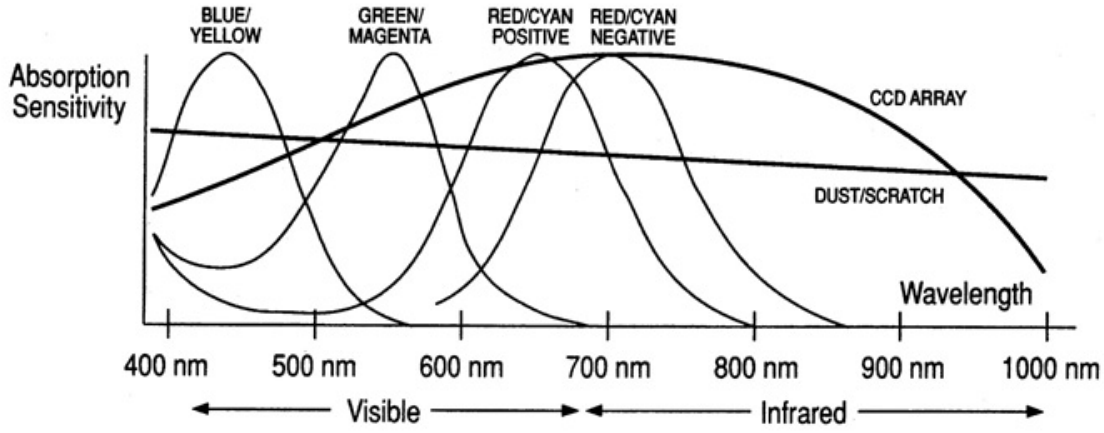

Figure 3.2.5: Absorbance of color dyes, sensitivity of the CCD and absorbance of flaws in the visible and infra-red ranges (image from [43])

3.2.4 Digital ICE

The most effective hardware-assisted method for flaw detection in dye-based film is marketed as "*Digital ICE*". This method [43] acts by acquiring an additional infrared channel together with the visible color channels.

As shown in Figure 3.2.5, dye-based photographic film is mostly transparent to infrared radiation above $850nm$, and this transparency is not dependent on the dye concentration (i.e. the film image is irrelevant). Conversely, dust and scratches are often opaque in the infrared region and are therefore recorded in the IR channel as definite marks on a homogeneous background (see Fig. 3.2.6).

A major limitation of this technique is that it can only be used on dye-based films (color and chromogenic black-and-white), as the image-forming silver particles in black-and-white film stocks are opaque to infrared radiation, thus making this method inapplicable.

The example in Figure 3.2.7 shows the digital retouch of a silver-based film using the IR channel. The dark areas have a high concentration of metallic silver, causing the software to mistakenly mark them as defects and to produce severe digital artifacts.

3.2.5 Dirt & Scratch Correction Option (D/SCO)

The British company *Cintel* developed a hardware-assisted digital method for the removal of dust and scratches on silver-based material [44]. Their scanner is equipped with an

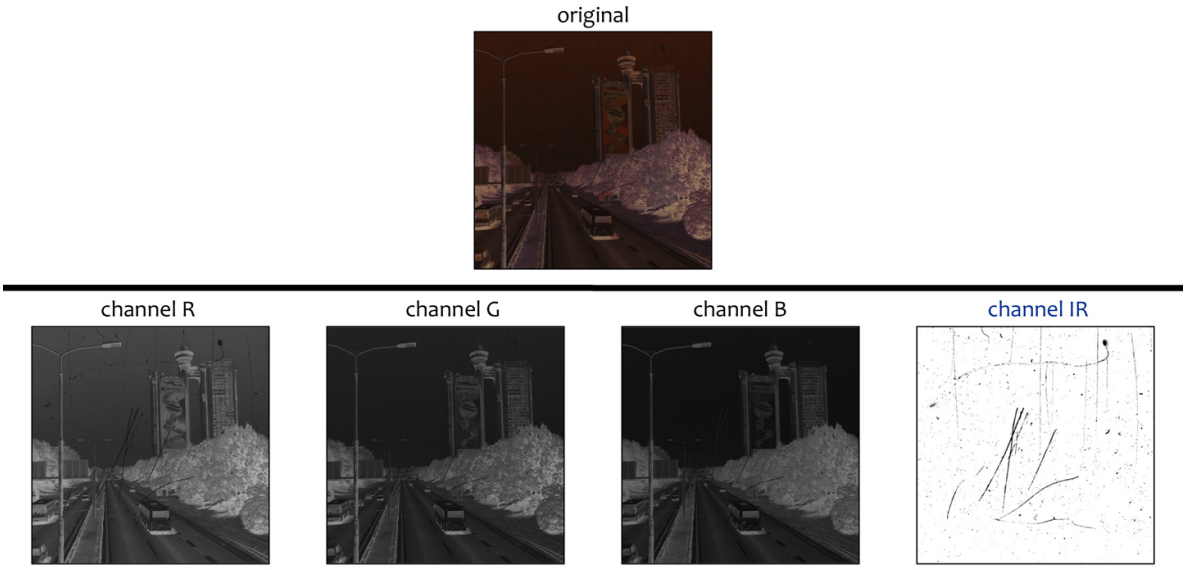

Figure 3.2.6: Digital ICE - acquisition of a fourth infrared channel

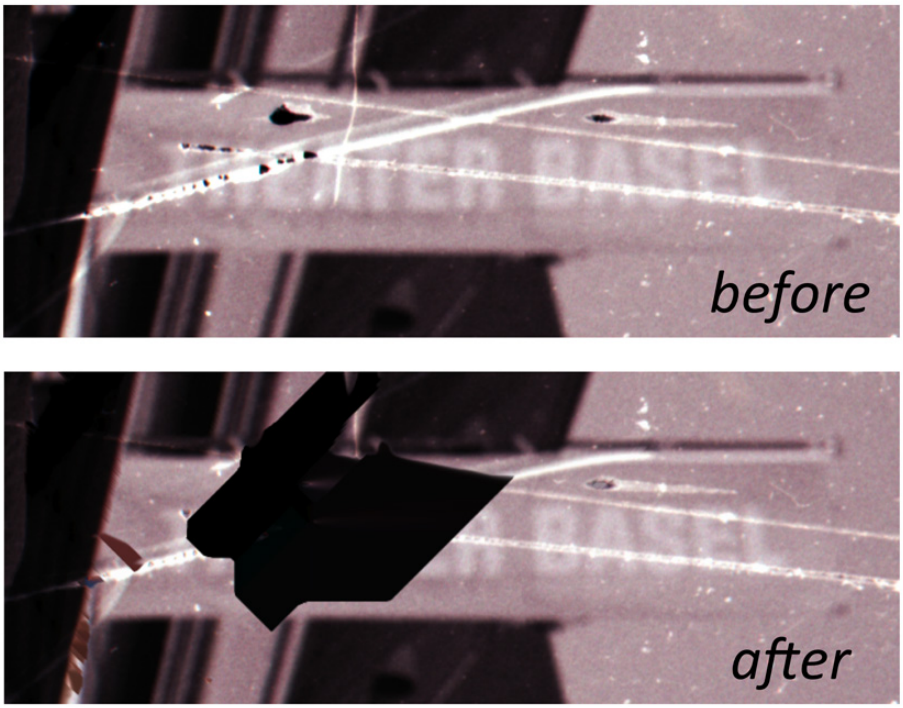

Figure 3.2.7: Severe digital artifacts due to the application of infrared cleaning on a silver-based film

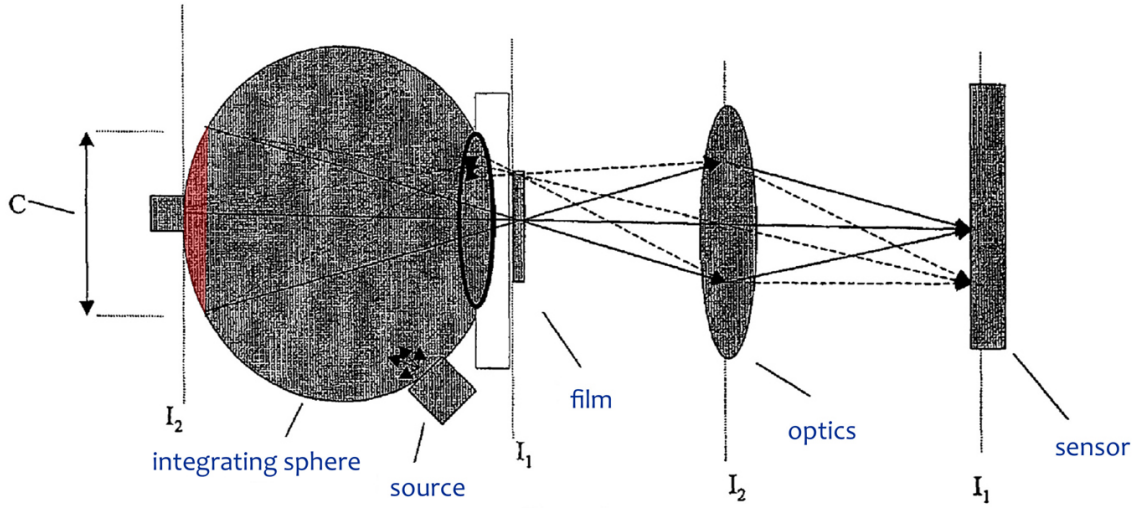

Figure 3.2.8: Sketch of the embodiment as depicted in the patent "Optical scatter correction for film scanners" (image from [44])

integrating sphere that provides the film with a diffused illumination.

A portion of the interior surface of the integrating sphere has a variable reflectivity (part C of the sphere in Fig. 3.2.8); this characteristic allows for the balancing of two different signals corresponding to the scattered and unscattered light (ref. Fig. 5.1.2). The tool "*Dirt & Scratch Correction Option*" (D/SCO) of the scanner software elaborates and compares these two signals and renders the flaws less visible, while simultaneously preserving sharpness and contrast.

Section 5.1.1 discusses the optical principles on which this technology is based, and section 6.2.3 proposes a novel method based on these same principles.

Chapter 4

Film and its interaction with light

With the exception of wave effects (*ray optics*), light interacts with matter being reflected, absorbed, scattered or directly transmitted [1].

In Figure 4.0.1, the case of two media and one interface is considered. There are three possibilities for an incident ray on the interface; it can either follow the laws of reflection, contributing to the specular reflection, or it can be scattered backwards, contributing to the diffuse reflection, or it can penetrate through the second medium, contributing to the refraction. There are also three possibilities for a ray inside a medium; it can be transmitted undeviated, contributing to the direct transmission, or it can be transformed into other forms of energy, contributing to the absorption, or it can be scattered, contributing to the diffuse transmission [45].

4.1 Scattering

Scattering is the deviation of rays from their original direction; the deviation is due to shape irregularities and impurities in the material in which the rays are propagating (scattering centers or particles).

Maxwell's equations constitute the foundation of the electromagnetic theory that explains the propagation of light. Exact computational methods for the description of light scattering descend from the Maxwell's equations; however, the exact analytical solution of the equations requires specific approximations and assumptions. Different formal models have been developed to compute the angular distribution of scattered light for a given system: e.g. the *Rayleigh scattering* for very small particles [46], the *Van de Hulst approximation* for large particles with small refractive index [47], the *Mie solution* for homogeneous spheres of

[1] Other phenomena, such as interference, diffraction and polarization, are not explained by ray optics: depolarization will be treated in sec. 4.3

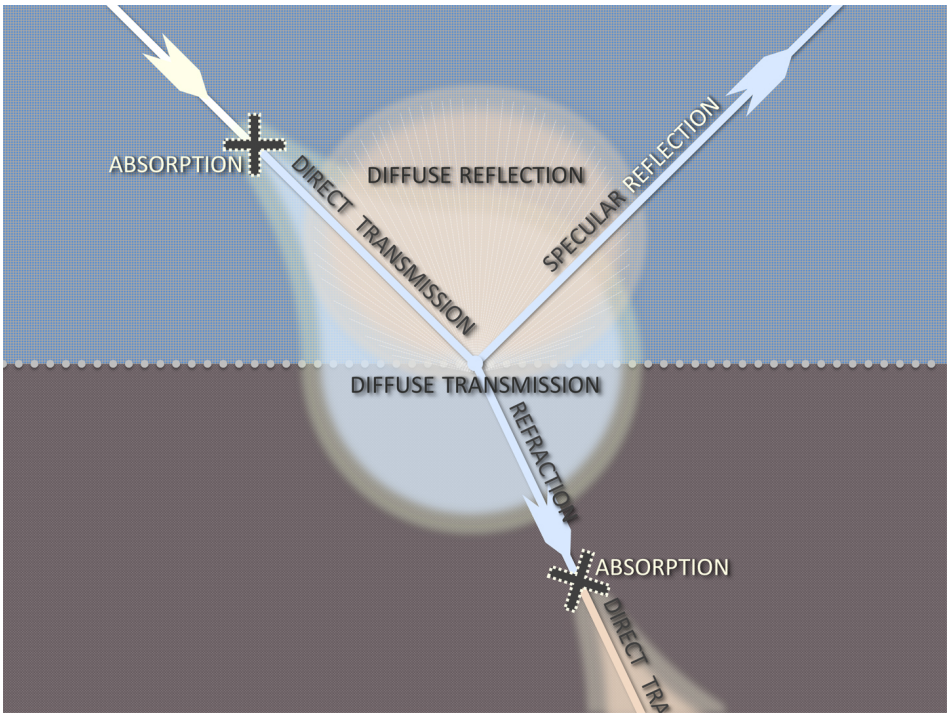

Figure 4.0.1: Interaction between light and matter inside media and at interfaces

arbitrary size [48], and the *discrete dipole approximation* (DDA) for periodic structures [49]. The assumptions made by these models often limit their applicability for the description of real cases [50].

A physical model has been proposed for the numerical prediction of light scattering for unexposed silver halide crystals [51]. Unfortunately, because of the complexity of the clumping medley of randomly oriented filamentary silver particles, the application of a formal model for processed silver-based photographic emulsions is impractical.

Light scattering can be analyzed by considering a system composed by three elements: (I) the incident light, (II) the scattering particles, (III) the medium in which the scattering particles are immersed. The amount of scattered light (*scattering fraction*) is influenced by [52]:

- the concentration of the scattering particles,
- the relation of the particle size to the wavelength of light,
- the optical differences between particles and medium,
- the particle shape.

The most critical factor is the particle size and, as a rule of thumb, the maximum scattering occurs when the particle diameter is about half the wavelength of light [45].

A quite comprehensive parameter, widely used in scattering measurements, is the *size parameter* x, defined as

$$x = \frac{\pi \cdot D \cdot m}{\lambda} \tag{4.1.1}$$

where D is the geometrical particle diameter, m is the real part of the refractive index of the medium and λ is the wavelength of light.

The size of the silver particles in a film can have different size distributions, depending on the film sensibility; a typical processed negative emulsion with an average speed has silver particles spanning from $0.2\mu m$ to $2\mu m$ [22]. Given a system with such a particle size distribution hit by rays of the visible range, and given a refractive index of the gelatin medium of $m = 1.6$ [53], the formula 4.1.1 yields the following size parameters: $x \simeq 1.4$ for the longest wavelength and the smallest particle, and $x \simeq 25$ for the shortest wavelength and the biggest particle.

A broadly applicable descriptive model for scattering has been proposed [45]; Figure 4.1.1 reports the $\lambda - scattering$ plot obtained by applying this model to the case of scattering particles dispersed in gelatin. The interaction between photographic film and the visible range of electro-magnetic radiation is characterized by a high scattering fraction; in fact, the peak at $x \approx 1.9$ is included in the range of the case considered.

4.2 Model for film-light interaction

Photographic film is a system constituted of several layers and interfaces (see Chap. 1); when the film is illuminated, light runs into the phenomena sketched in Figure 4.0.1 at each layer and at every interface. A specific incident light ray, depending on the sequence of phenomena occurring, can have different lots; the optical characteristics of the materials involved and their particular arrangement determine the probability of these lots, making many of them negligible. The following are three examples: (I) as the film base is by nature transparent, the absorption and the diffuse transmission through it are negligible; (II) there is a small difference between the refractive indexes of the base and of the gelatin, hence, the specular reflection at the base-emulsion interface is negligible; (III) photographic film is manufactured to be smooth, hence, the diffuse reflection at the interface between air and base is negligible.

Taking the above arguments into consideration, a model can be depicted for the overall phenomena occurring during the interaction between light and a photographic film. In

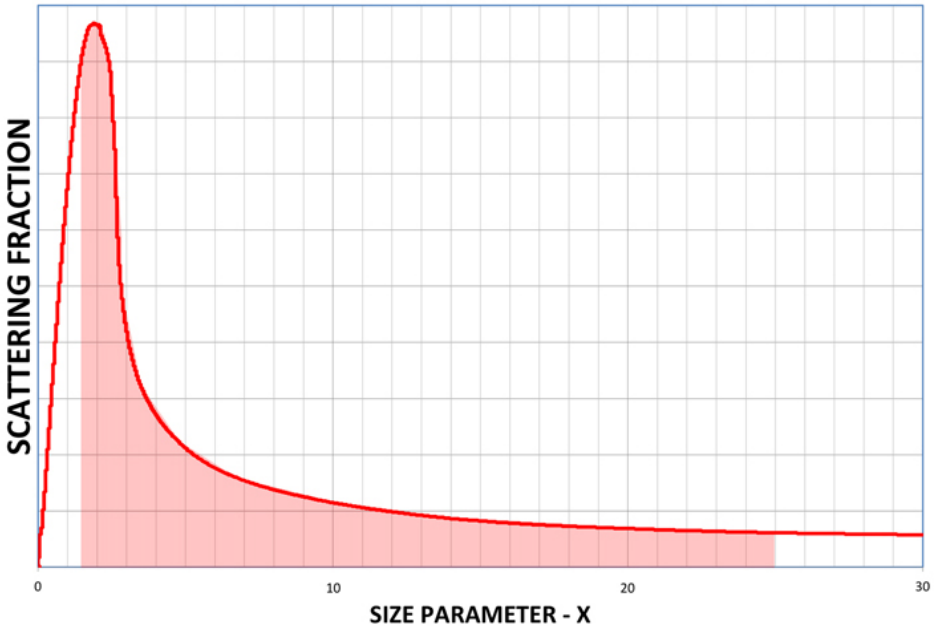

Figure 4.1.1: Relation between size parameter and scattering fraction: in red is highlighted the region relative to a typical silver emulsion irradiated with visible rays

Figure 4.2.1, the model is sketched on the left. Even though the film has many different layers (as described in Chap. 1), it is considered here as a single layer, in which the incident rays can have five behaviors: they can be bounced backward, specularly (I) or diffusely (II), they can be absorbed (III), or they can emerge from the other side, directly (IV) or diffusely (V).

In Figure 4.2.1, the image on the right is a photograph of a silver-based film (the central horizon of the image) hit by a thin pencil of light (the incident beam) provided by a laser. During the long exposure necessary to produce a significant signal, smoke was blown into the air to reveal light. The distribution of light intensity around the film suggests that the model presented on the left properly represents the true behavior of light.

The graphics of Figures 4.0.1 and 4.2.1 depict the backward and forward diffusions of light with a spherical intensity distribution. In reality, in order to have a comprehensive and accurate description of the light scattering property of a surface, the *Bidirectional Scattering Distribution Function* (BSDF) should be determined.

For a fixed point x of the surface, we consider the irradiance dE_i arriving on the surface from an infinitesimal cone $d\sigma$ around a particular direction ω_i ($L_i(\omega_i)\, d\sigma^{\perp}(\omega_i)$) and the consequent radiance dL_0 leaving the surface in another direction ω_0 ($dL_0(\omega_0)$). In Figure 4.2.2, the two directions ω_i and ω_o are indicated in terms of polar and azimuthal angles θ and ϕ. For a given combination of ω_i and ω_o, under normal circumstances, the ratio

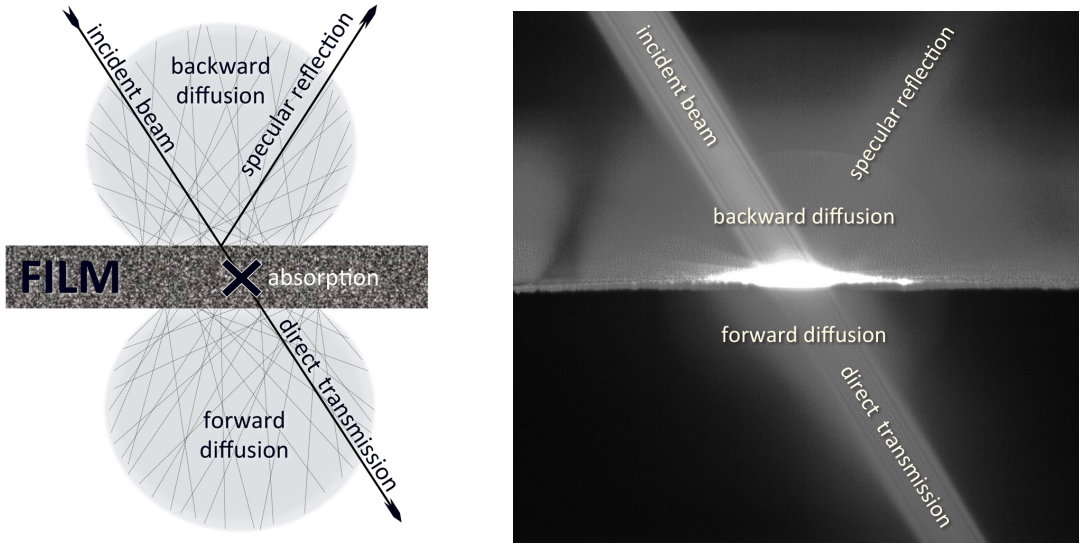

Figure 4.2.1: Interaction between light and photographic film: model (left) and light intensity acquisition (right)

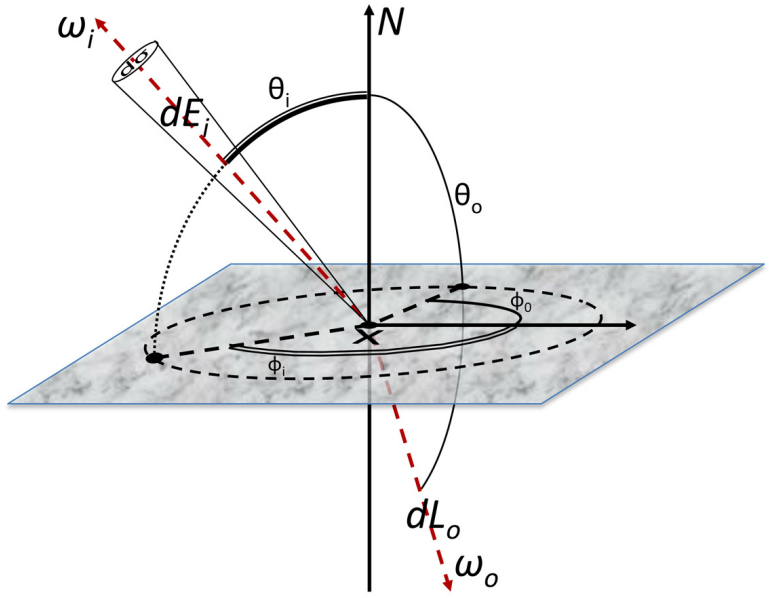

Figure 4.2.2: Bidirectional Scattering Distribution Function for transmitted component ($\theta_0 > 90°$)

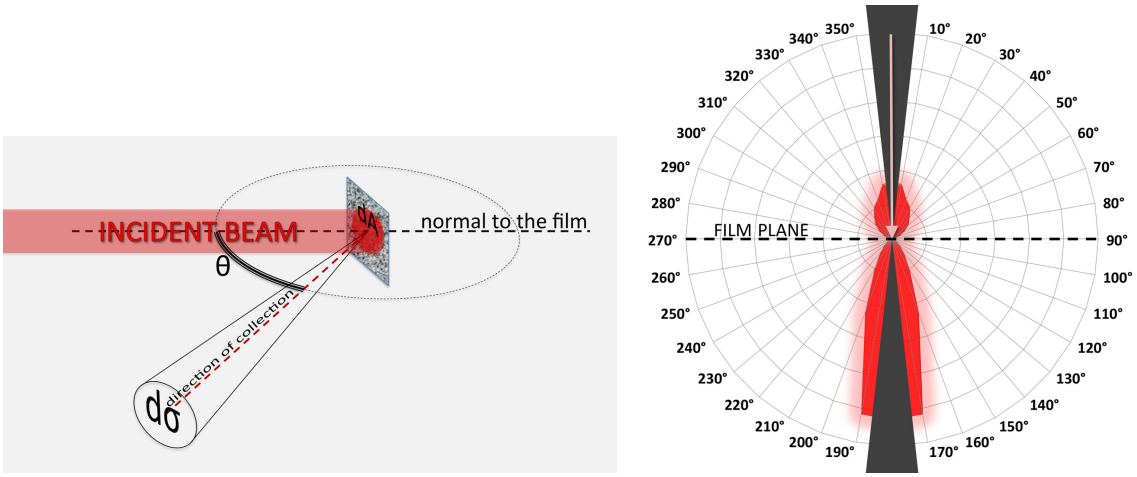

Figure 4.2.3: Angular distribution of scattered light of a photographic emulsion: measurement setup (left) and measured radiant intensity (right)

between the scattered radiance dL_0 and the incident irradiance dE_i is constant: the BSDF is the function that defines the ratio $\frac{dL_0}{dE_i}$ for all the pairs ω_i and ω_o [54, 55].

The present dissertation does not seek to completely define the BSDF; however, it is essential to describe the angular distribution of the light scattered by the photographic film. For a given irradiance normal to the film ($\omega_i \equiv N$), we measure on a plane (for a given ϕ_0) the light scattered by the sample as function of θ_0. We arrange the measurement setup as sketched on the left in Figure 4.2.3 [56]. A small (infinitesimal) area of processed photographic film (dA) with a relatively high optical density is orthogonally hit by a 'pencil beam' provided by a laser; a light sensor measures the light scattered at the angle θ with the normal to the surface; the light sensor collects the light rays within a small (infinitesimal) solid angle ($d\sigma$). A systematic sequence of measurements are carried out, varying the angle θ all around the sample.

The measurement cannot be collected for $\theta = 0°$ and $\theta = 180°$ (no measure sectors). In the first case, the source-sensor covering obstructs the measurement, while in the second case, the detector is 'blinded' by the predominant directly transmitted fraction.

The angular distribution of light scattering is measured in the above described setup. The response of the light sensor is proportional to the luminance; to obtain the luminous intensities (in arbitrary unit), the measured values have to be multiplied by $\cos\theta$. The plot of the scattered light is reported in Figure 4.2.3 on the right (the incident beam comes from above; the gray area indicates the 'no measure sectors'). The plot shows that the forward scattering is higher than the backward scattering and that a higher scattering is exhibited for small angles; the upper lobe in the plot is, in fact, smaller than the lower one, and they both have an elongated shape.

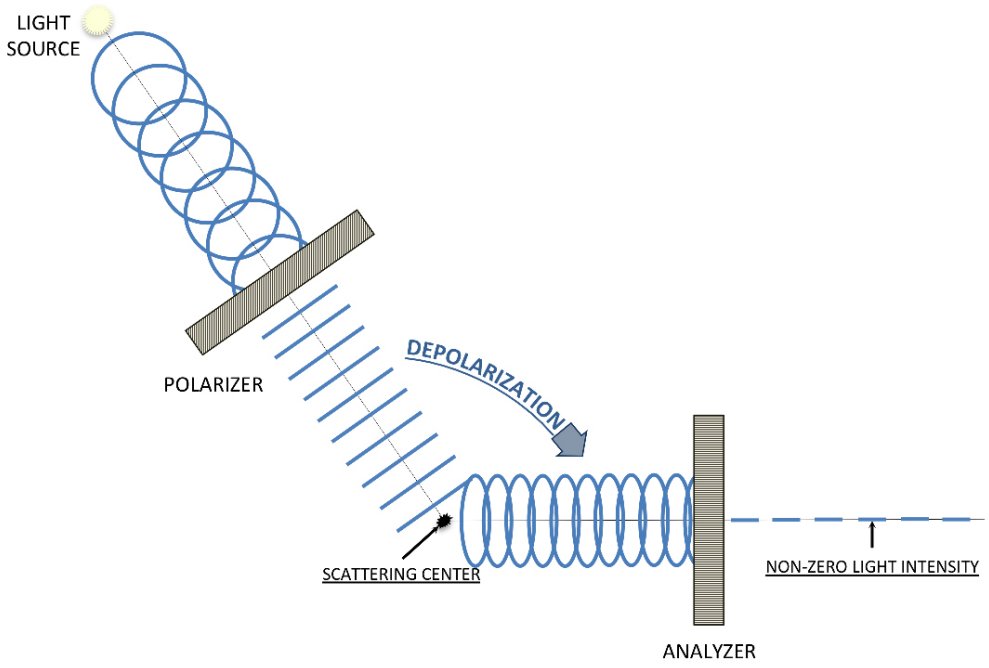

Figure 4.3.1: Depolarization of scattered light

4.3 Depolarization

Electromagnetic scattering by small particles can produce light with polarization characteristics different from those of the incident beam [57]. In particular, when illumination is linearly polarized in full, the scattered light may become partially or totally unpolarized; the phenomenon is called *depolarization* and it can occur even if the scattering particles are not optically active (Fig. 4.3.1) [58].

To analyze the angular distribution of the depolarized scattered light, the same experiment as previously described is repeated with the addition of polarizer and analyzer as sketched in Figure 4.3.2 (left).

The angular distribution of light scattering is measured for the same sample; the plot is reported in Figure 4.3.2 on the right. Contrary to the plot of the unpolarized case, this second plot shows that the backward scattering is higher than the forward scattering and that the angular distribution of scattering is quite uniform; the upper lobe in the plot is, in fact, bigger than the lower one, and they both have a rounded shape.

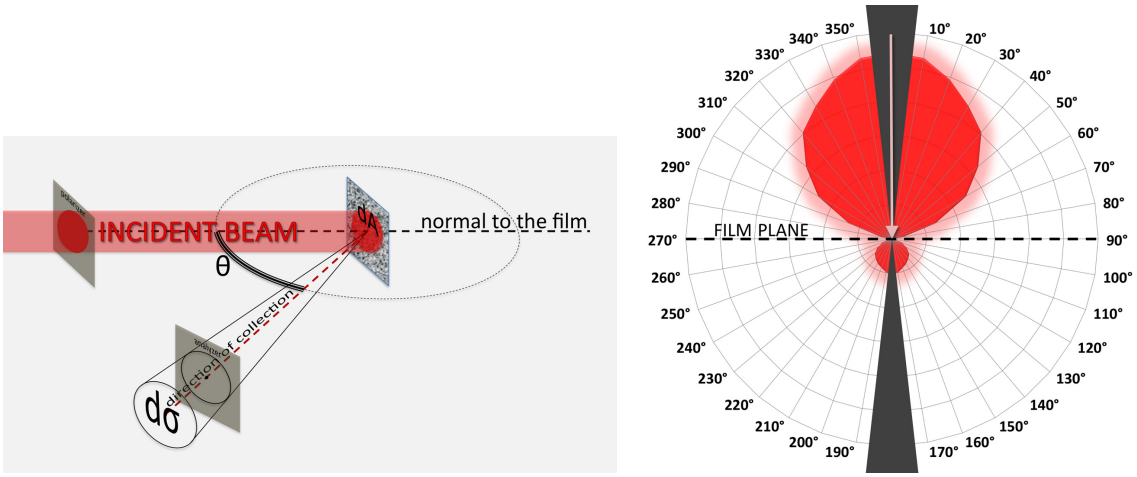

Figure 4.3.2: Angular distribution of scattered light of a photographic emulsion - polarized case: measurement setup (left) and measured radiant intensity (right)

4.4 Light & fundamental image particles

The behavior of light when passing through processed photographic emulsions is very different according to the type of emulsion (Fig. 4.4.1). A silver-based emulsion is a very heterogeneous system; the optical characteristics of silver particles are very different from those of the gelatin in which they are immersed and, therefore, the image particles act as scattering centers. The illuminating beams are absorbed and scattered. On the other hand, dye clouds do not constitute an obstacle for light; their refractive index (at least its real part) is very similar to the refractive index of the medium in which they are immersed. Wavelength-selective absorption is essentially the only phenomenon occurring in dye-based emulsions.

4.5 Light & flaws

As previously discussed at the end of Chapter 2, dust and scratches are two different types of irregularity of film surfaces: dust is additional material on the film surface while, in the case of a scratch, the film material is missing. The additional material that may accidentally lie on the film surface can have any substance and shape; it can be opaque, thus obscuring the underlying emulsion image or, conversely, it can have a certain degree of transparency, thus allowing some light to pass through. In this latter case, the underlying part of the image is visible (Fig. 4.5.1).

Dust lying on the emulsion side of the film is almost in contact with the emulsion. For dust lying on the base side, however, the transparent base keeps a distance between the dust

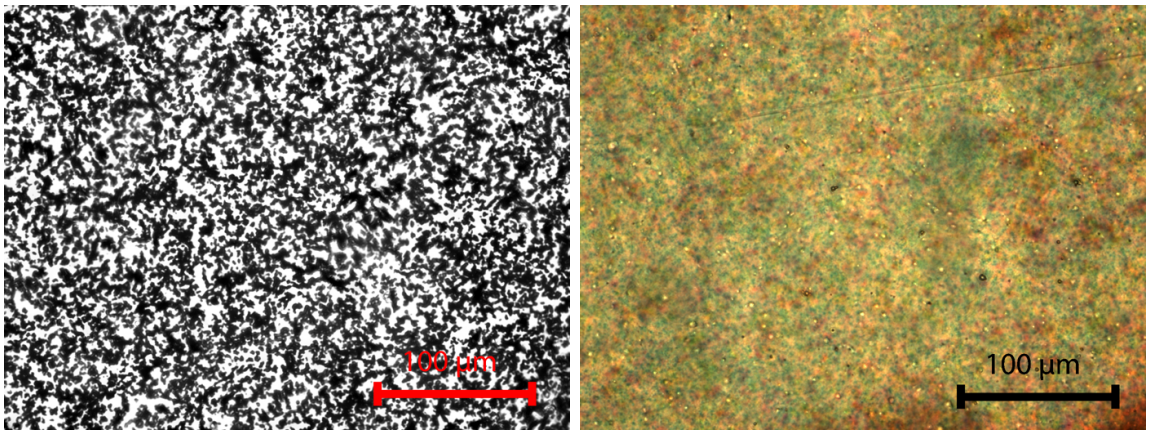

Figure 4.4.1: Images acquired using an optical microscope: silver-based film (left) and dye-based film (right)

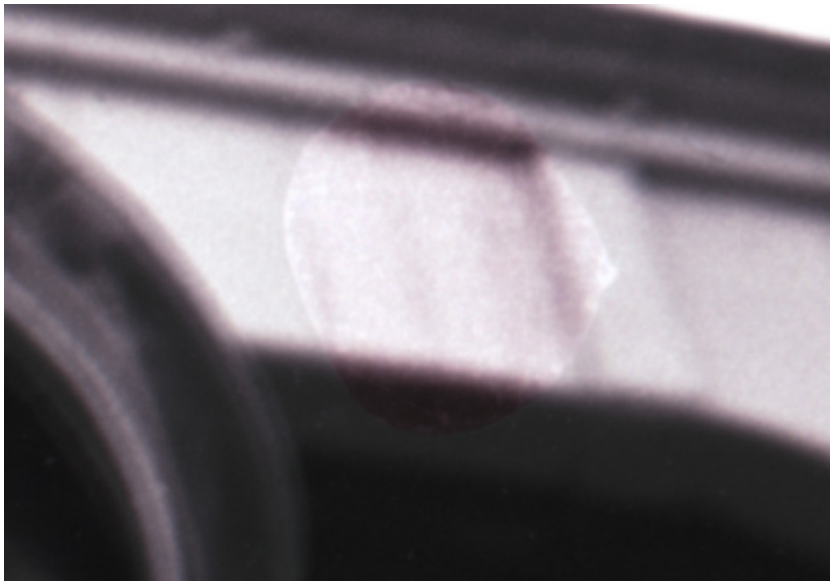

Figure 4.5.1: Transparent stain on black-and-white film

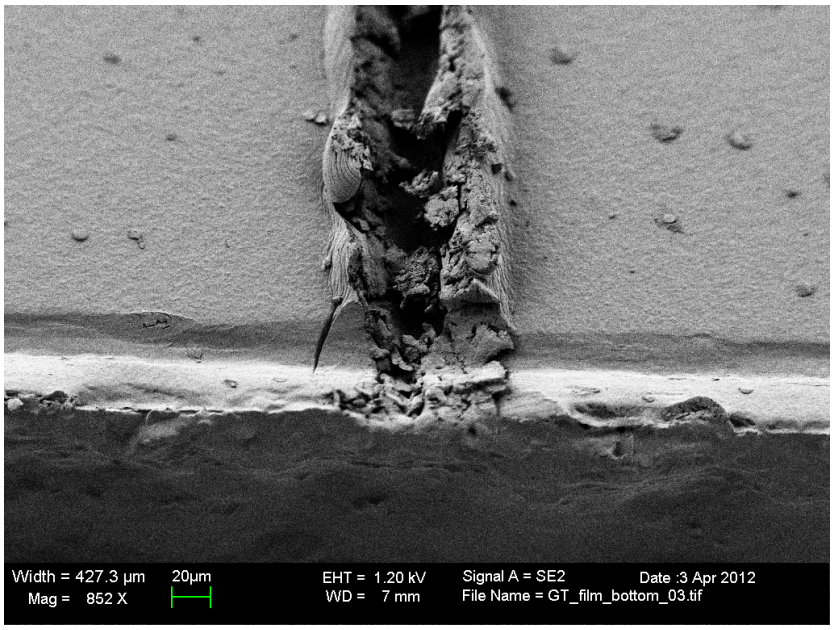

Figure 4.5.2: Image taken with a Scanning Electron Microscope: a scratch appears as a linear valley with two wrinkles beside it (image created by Joakim Reuteler)

grains and the emulsion image; in this second case, the adoption of an oblique illumination may manifest strong shadowing effects (see sec. 6.2.2).

The film surface corresponding to a scratch is generally very irregular (Fig. 4.5.2) and this entails a reduction in transparency due to light diffusion; for this reason, scratches generally appear dark in bright-field illuminations (sec. 5.1.1). However, in the case of penetrating scratches, the emulsion layer may become thinner or may even be completely removed; in this case, the absorption is reduced and the scratches, contrary to the superficial ones, may appear bright when the film is illuminated in a bright-field setup (Fig. 4.5.3).

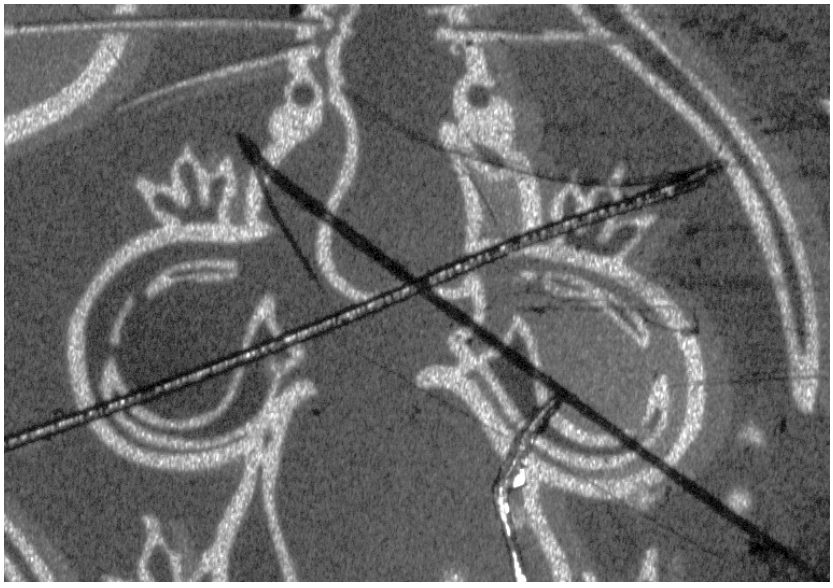

Figure 4.5.3: A photographic film with both penetrating (bright) and superficial scratches (dark)

Chapter 5

Imaging photographic film

A film 'carries' a photographic image as a spatial variation of the fraction of light that passes through it and emerges from the other side [19]. In order to be fully defined, this image has to be 'seen' by an image detector; the latter is a system constituted by an optical system that creates a real image that is collected by an array of independent light sensors. The image detector (whether an eye or an imaging device) is necessary to define the brightness of all the elements of the image, i.e. to define the image itself. After the interaction with the film, the emerging light is collected by the optical system of the image detector and is sent to the sensor. In Figure 5.0.1, the setup of the image formation is sketched.

Transparent photographic material is often projected; in this case, in place of the sensor, there is the reflecting screen, and then visualization takes place in a supplementary stage. However, focusing the film on a surface, also in case of projection, constitutes the first stage of the image formation: the points P of the film and the points Q on the sensor are conjugate for the optical system. *Contact printing* is an exception, as in this case, the optical system is not necessary; the film and the photographic paper (the light sensor) are in contact[1]. Aside from this latter case, in which the whole emerging light participates in the image collection, the image detector collects just a portion of the emerging light (Fig. 5.0.1); the aperture determines the portion of rays that reach the light sensor.

Each point of the photographic film is characterized by an *optical transmission density*; in the present thesis, we prefer to call this physical quantity *attenuance* [59]. Let J_o be the luminous flux measured by a light sensor in the absence of the film and J_1 be the luminous flux measured in the presence of the film. The attenuance D is defined as:

$$D = \log {}^{J_0}/_{J_1} \tag{5.0.1}$$

[1]For the sake of completeness, a *pinhole camera* can be mentioned as another setup for imaging photographic film that does not require an optical system, but actually, such setup is never used for this purpose.

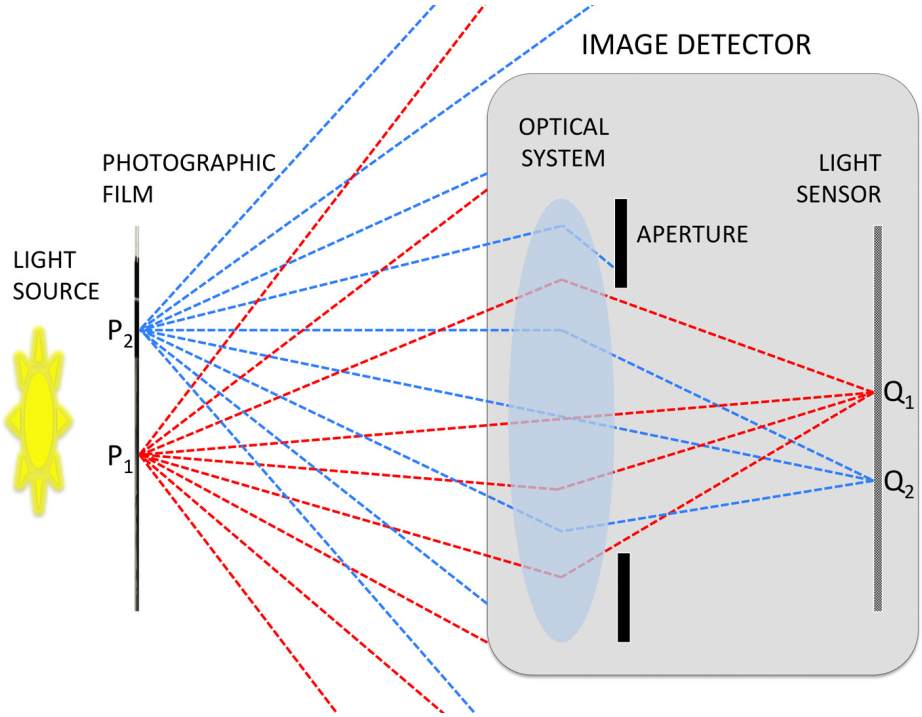

Figure 5.0.1: Setup for the image formation of a photographic film

The measured light is attenuated due to the depletion of the rays into the film (absorption) and due to their deviation in directions uncollectible by the light sensor (scattering) [60]. The spatial distribution of the attenuances defines the photographic image impressed on the film.

The digital reproduction of a photographic film is created in the arrangement depicted in Figure 5.0.1; the light sensor (CCD or CMOS) of the camera/scanner lies or moves parallel to the film plane, in the exact place where the optical system creates the real image of the silver emulsion.

The spatial resolution (i.e. the number of pixels that represent the unit of length) required to capture the full image information content of a photographic film is a thorny issue. In the experiments reported, we adopted a spatial resolution of $3200ppi$ (pixel per inch); in most cases, a higher resolution of the digital reproduction would not yield any additional information about the photographic image [36, 61].

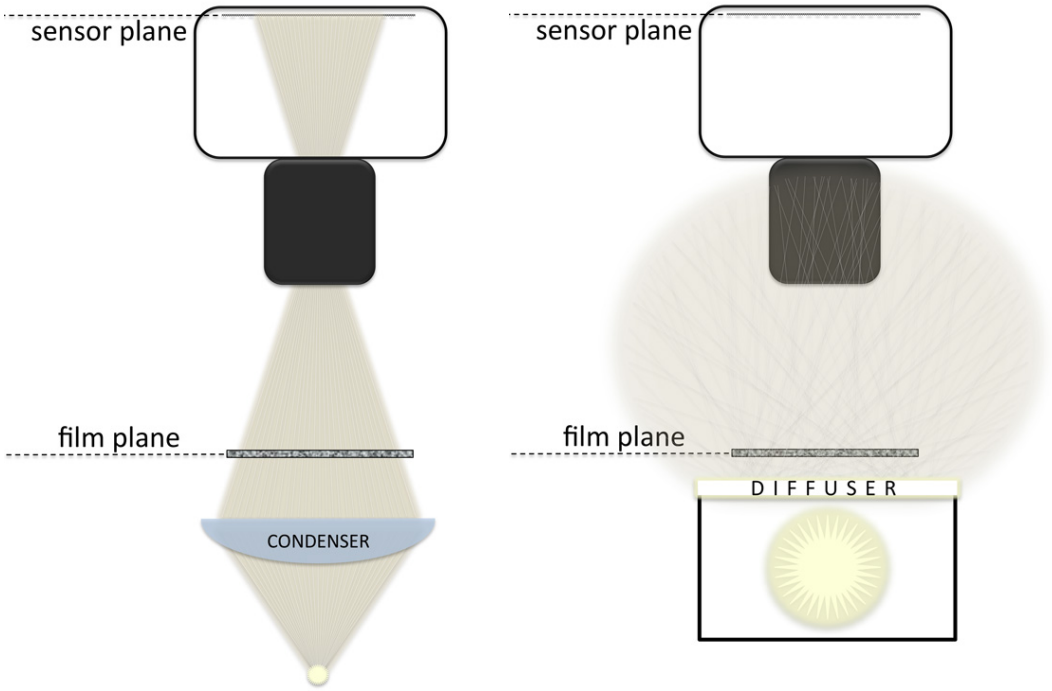

Figure 5.1.1: Directed bright-field setup (left) and diffused bright-field setup (right)

5.1 Illumination methods

When an object is visualized, the directional properties of the illumination define the manner in which the lighting component interacts with the reflection, the transmission and the scattering properties of the object [62]. Many types of illumination can be used, and different features of the film will be emphasized according to the technique adopted, thus yielding varying appearances. In the present section, a list of important illumination setups is reported (the terms utilized often come from optical microscopy).

5.1.1 Bright-field setups

The term "*bright-field*" refers to the most typical transmission setup and represents the operational setup for photographic transparencies. The illumination is *paraxial*, i.e. a substantial part of the rays that illuminate the sample do not diverge very much from the optical axis of the imaging device. By varying the degree of collimation of the rays, it is possible to arrange countless different bright-field setups [63]. Two extreme manners are reported in the following text.

Directed bright-field

The *directed bright-field* has extremely strong directional characteristics by means of an optical system, and it is the most energy-efficient illumination setup; in fact, it is adopted for projection in cinema theaters, where a high illuminance over a large surface is required.

In a directed bright-field setup, a lens (*condenser*) converges the illuminating rays. The optical axis of the condenser coincides with the optical axis of the imaging device; a point light source and the condenser are placed so that the cone of acceptance of the objective encompasses the condensed light (see Fig. 5.1.1 - left). In such an arrangement, all the rays accepted by the lens are used for the image formation. The photographic film is placed between the condenser and the optical system, and it is focused on the sensor; each point of the film receives light from only one direction. This type of illumination is also called "*specular*".

Diffused bright-field

In a *diffused bright-field* setup, the illumination of the film is provided by an extended plane source with uniform luminance and with light emission that does not have a preferred direction. These characteristics are sought using a mechanism in which light exits from an integrating chamber through a translucent slab (*diffuser*); when the diffusion is optimized, the emission obeys the rules of a *Lambert radiator*, in which the luminance indicatrix of the slab forms a half sphere.

When a diffused source is used for the illumination of a photographic film, the translucent slab and the film lay parallel to each other (see Fig. 5.1.1 - right). In this arrangement, each point of the film receives light equally from all the directions. A short distance between the film and the translucent slab guarantees that the slab is not in focus and that any imperfections on its surface are not imaged.

5.1.2 Callier effect

In Figure 5.1.2, the same silver-based film is reproduced in a directed bright-field setup and in a diffused bright-field setup. The images appear quite different: the image on the left is much more 'crisp' and the film grain is emphasized together with dust and scratches, while the image on the right appears to be 'softened' and less sharp. The balance between the brightness of the different parts of the film is also changed: the contrast on the left is much stronger than that on the right. By looking at the targets in the scene, the difference in contrast is evident.

In Figure 5.1.3, the directed bright-field image and the diffused bright-field image are shown for a dye-based film. As in Figure 5.1.2, the image on the left is sharper, and this is

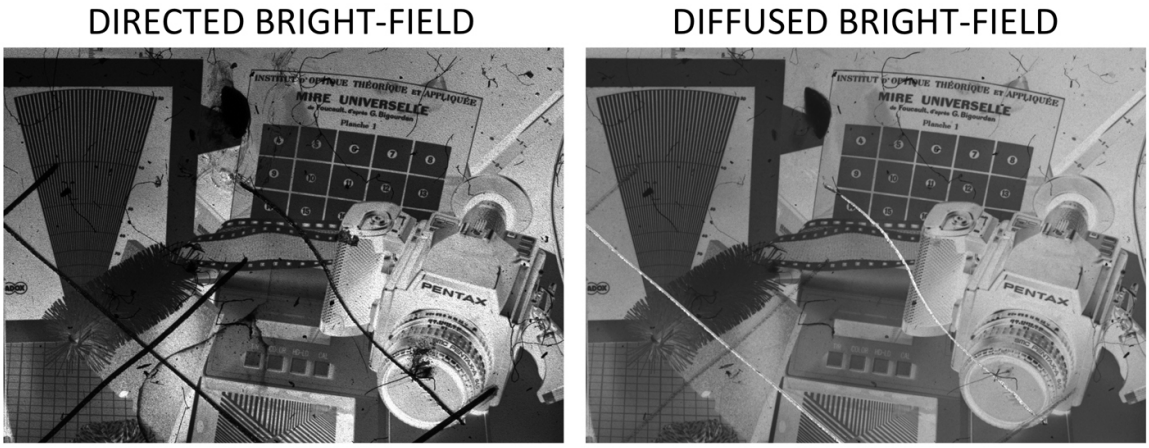

Figure 5.1.2: The same silver-based film acquired in a directed (left) and a diffused (right) bright-field setup

particularly evident with regard to dust. The contrast for the directed setup, however, is the same of the diffused bright-field image.

The attenuances (due to absorption and scattering) of all the points of a film determine the image the film carries. Like every physical quantity, the attenuance can only be defined if its measurement conditions are fully delineated; as explained in previous sections, the manner of illumination plays a fundamental role in the attenuance [64].

Let us consider a specific point of a film. When the image is acquired in a directed bright-field setup, that point is hit by light from a specific direction; if the point scatters light and a portion of the rays are deviated in directions uncollectible by the image detector, than no other directions of incidence will be available to let light reach the sensor. Therefore, the point will be dark. On the other hand, when the image is acquired in a diffused bright-field setup, the same point of the film is hit by light from a multitude of directions. If a ray is scattered away, it is likely that another incident ray will be deviated in a direction collectible by the sensor. Therefore, the point will not be as dark as in the directed setup.

Irrespective of the manner in which the illumination is provided, the rays that are absorbed by a specific point do not reach the sensor, no matter what. As a consequence, in the absence of scattering (as in the case of the dye-based material), the attenuance is independent of the manner of the illumination. A dense point absorbs a lot of light and a less dense point absorbs little: the difference between their attenuances is the same in the images acquired in the directed and in the diffused setups. The contrast remains the same in the two images of dye-based film.

On the other hand, in the case of silver-based material, the contrast changes considerably with the degree of illumination diffusion. A dense point scatters a lot of light and a less

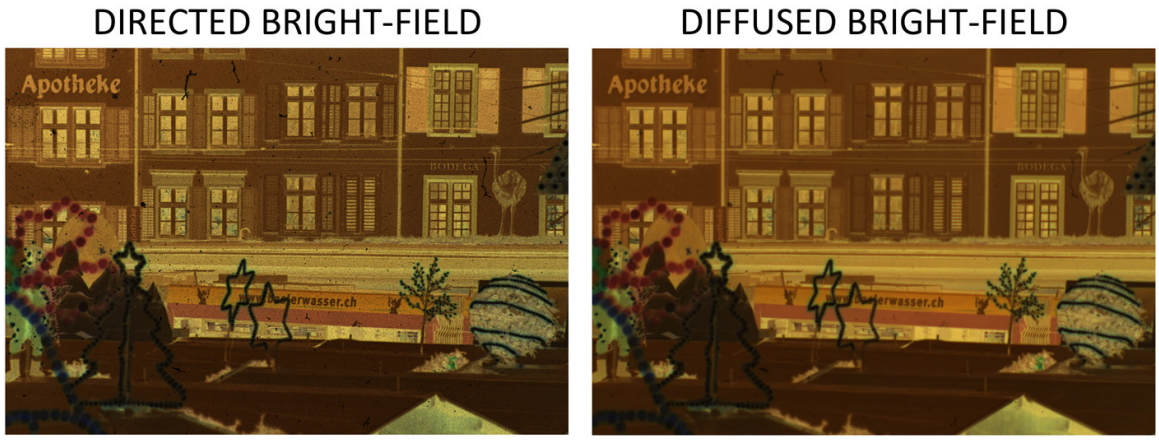

Figure 5.1.3: The same dye-based film acquired in a directed (left) and a diffused (right) bright-field setup

dense point scatters little: for the above reasons, this difference has a greater impact on the image resulting from a directed setup rather than from a diffused setup.

By applying the same concept on a smaller scale ("*micro-contrast*"), the variation of the sharpness between the two images of the silver-based film can also be explained.

The ratio between the attenuances, which were measured illuminating the sample *specularly* (as in a directed bright-field) and *diffusely* (as in a diffused bright-field), is termed the *Callier Q factor* [60]:

$$Q = \frac{D_{\shortparallel}}{D_{\nparallel}} \tag{5.1.1}$$

The Callier Q factor is always equal to or greater than unity; its typical trend versus the diffusely measured density $D_{\nparallel}$ of a given silver-based film is reported in Figure 5.1.4 [65].

The variation in contrast and sharpness of the images produced with different types of illumination (for example with a condenser or a diffuser enlarger) was observed over a long period of time [66] and became known as "*Callier effect*".

The following passages report on an experiment used to clarify this phenomenon. Four samples were selected, they being square fragments of homogeneously processed film:

- a high density silver-based film (***silverHD***)
- a low density silver-based film (***silverLD***)
- a high density dye-based film (***dyeHD***)
- a low density dye-based film (***dyeLD***)

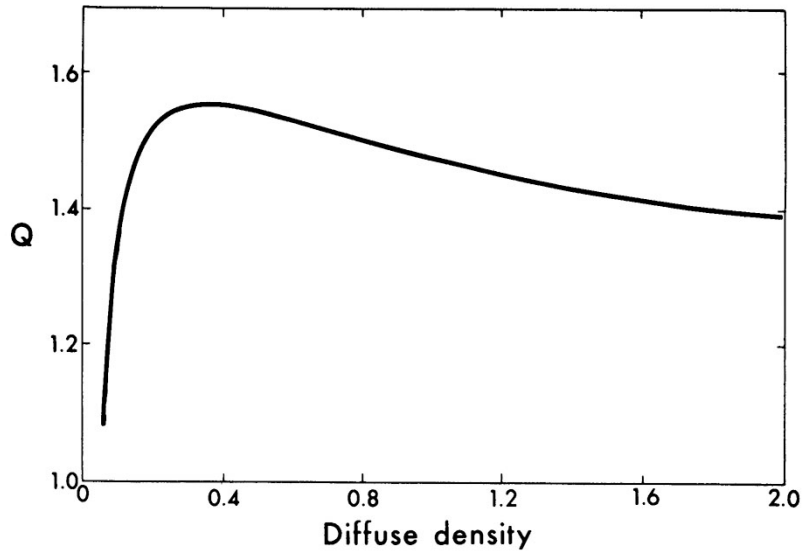

Figure 5.1.4: Callier Q factor versus diffuse density

Two measuring setups were arranged to calculate the attenuance, with both setups having the same conditions of light collection but different conditions of illumination (Fig. 5.1.5):

- a specular setup
- a diffused setup

The luminous fluxes measured by the light sensor are reported in Figure 5.1.6 in arbitrary unit.

By applying the formula 5.0.1 reported at the beginning of the chapter, the attenuances of all the samples were calculated for the two setups. The values follow in the table:

	specular setup - $D_{\shortparallel}$	*diffused setup* - $D_{\nparallel}$
silverHD	1.53	0.87
silverLD	0.29	0.20
dyeHD	1.59	1.55
dyeLD	0.75	0.69

The Callier Q factor was calculated with the formula 5.1.1. The values obtained follow:

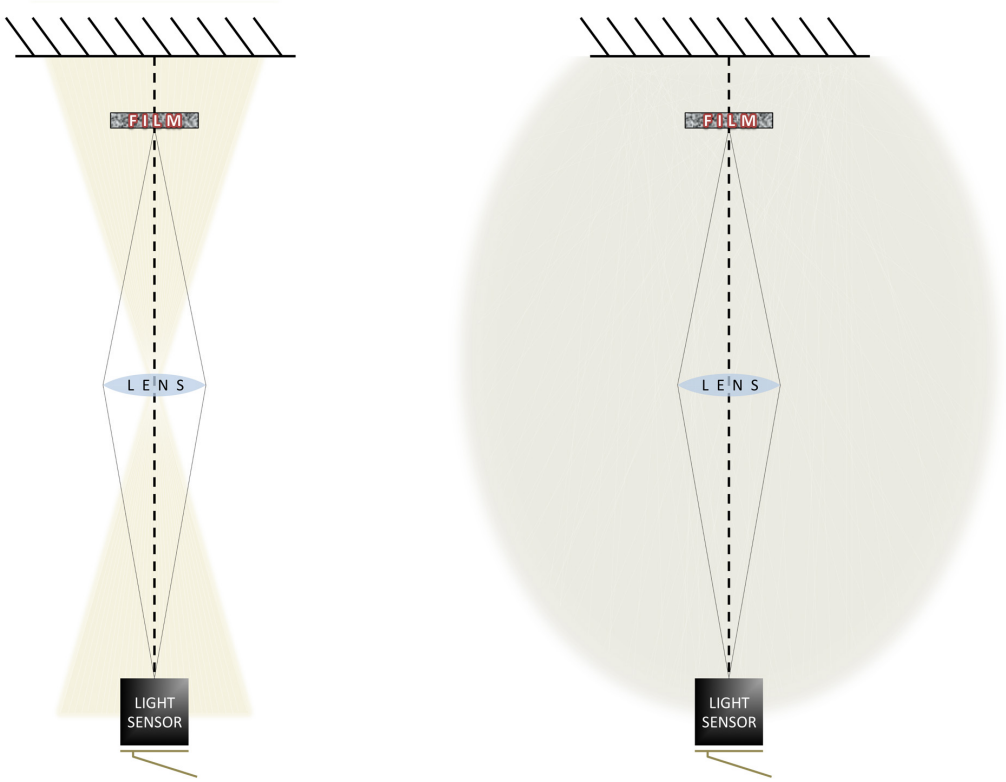

Figure 5.1.5: The specular (left) and the diffused (right) setups for the optical density measurement

Figure 5.1.6: Luminous fluxes measured in arbitrary unit

	Callier Q factor - Q
silverHD	1.76
silverLD	1.40
dyeHD	1.02
dyeLD	1.09

As was expected, Q is higher than 1 for the silver-based samples, for which the scattering fraction is relevant. On the other hand, for the dye-based samples, Q is just barely above 1, since the scattering is weak; the small scattering component, which is also present for these latter samples, is due to the imperfections of the material.

We refer to the *contrast* for human perception K as defined by:

$$K = (L_{max} - L_{min})/(L_{max} + L_{min}) \tag{5.1.2}$$

with L_{max} and L_{min} being the maximal and the minimal luminance of a scene.

Since the conditions of light collection do not change for the different measurements, the formula 5.1.2 can be used with the luminous flux values instead of the luminance values.

The contrast provided by the two different optical densities of the silver-based samples is:

- $K = [(10044 - 568)/(10044 + 568)] = 0.89$ in case of specular illumination
- $K = [(9662 - 2073)/(9662 + 2073)] = 0.65$ in case of diffused illumination

For the dye-based samples, the contrast provided is:

- $K = [(3451 - 503)/(3451 + 503)] = 0.75$ in case of specular illumination
- $K = [(3174 - 435)/(3174 + 435)] = 0.76$ in case of diffused illumination

This simple experiment shows the significance of the Callier effect in the appearance of the photographic film.

5.1.3 Dark-field setup

The term "*dark-field*" indicates a special illumination geometry used in microscopy. In this technique, the sample is illuminated obliquely so that no directly transmitted light is collected by the optical system; light is collected only for elements of the sample that scatter light. Such an arrangement is useful to emphasize structures, shape irregularities and impurities

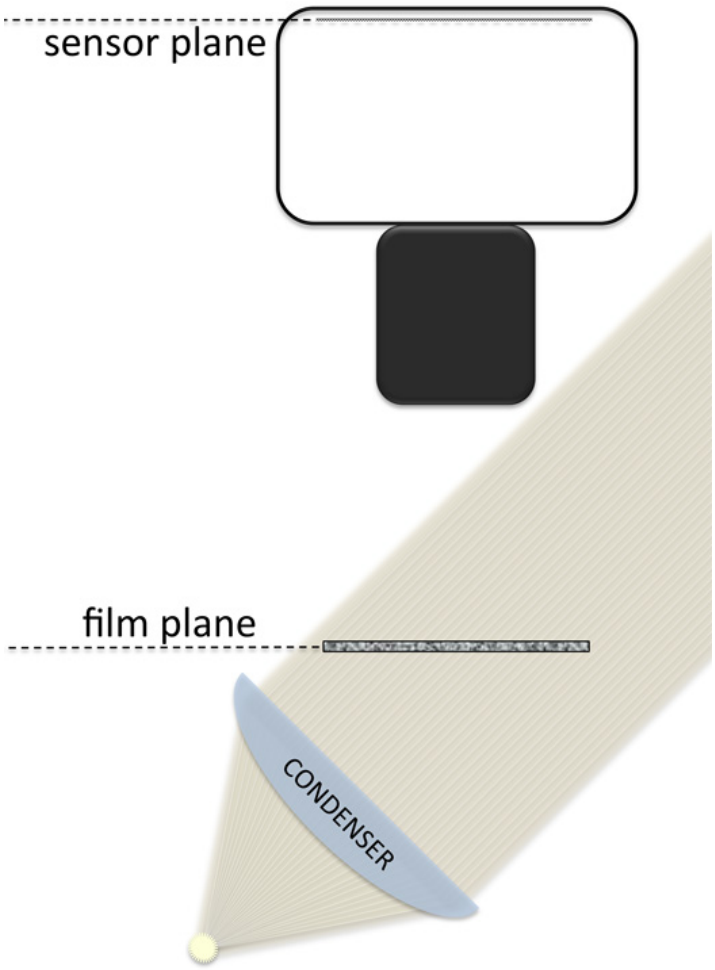

Figure 5.1.7: Dark-field setup for photographic film reproduction

in a sample that is otherwise homogeneous on a wavelength level; in the resulting image, the scattering elements will appear as bright marks on a dark background.

A dark-field setup can be used for the reproduction of photographic film. In Figure 5.1.7, a dark-field consisting of one source is sketched; the condensing lens allows a uniform illuminance on the film to be obtained.

5.1.4 Polarized setups

Originally applied in petrographic and mineralogical research, polarized microscopy has been also used in other fields in recent years.

Linear polarization of light can be used to enhance specific elements of a sample. Generally, there are at least two polarizing filters in polarized setups, with one in front of the illuminating source (*polarizer*) and another in front of the imaging device (*analyzer*); the directions of polarization of the two filters are orientated orthogonally. In this configuration, the sample lies between the two filters and, according to the *Malus' law* [67], light is not transmitted unless elements of the sample change the direction of polarization.

Polarized light can be used in a transmission setup to enhance specific elements of the photographic film.

Polarized bright-field setup

Linear polarization of light can be used in a bright-field setup. Light is not transmitted unless '*optically active*' elements of the sample perturb the direction of polarization. Polarizing filters can be added to the bright-field setups described in the previous section; the case of a directed bright-field is reported in Figure 5.1.8 on the left.

Polarized dark-field setup

A dark-field setup as described in section 5.1.3 can be combined with polarizing filters (Fig. 5.1.8 - right). The dark-field setup is useful to emphasize scatterers (structures, shape irregularities and impurities) in a sample: should these elements depolarize (ref. sec. 4.3) light more than their surroundings do, then the utilization of linearly polarized light in a dark-field setup further emphasizes the scatterers.

5.1.5 Reflection setups

The typical type of illumination setup for a photographic film is in transmission. However, reflection illumination setups, in which the camera and the light sources lie on the same side of the film, can be useful in particular cases.

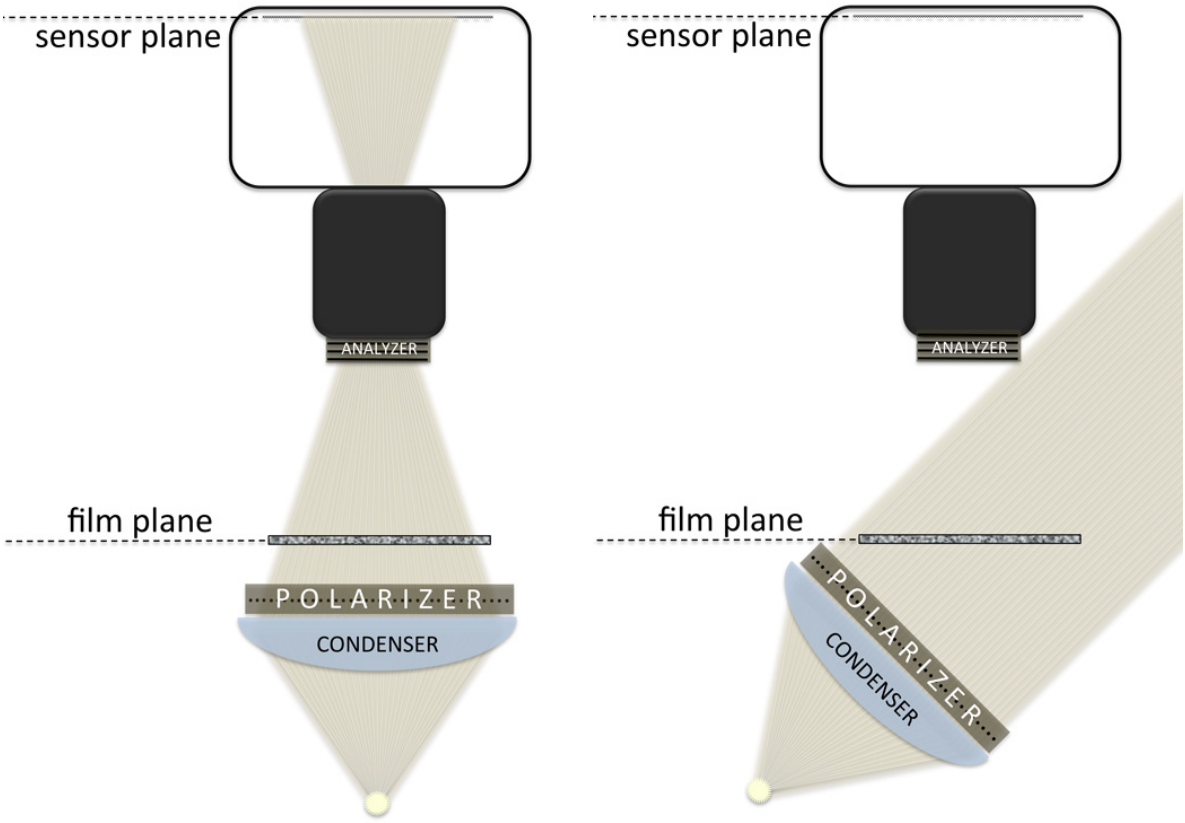

Figure 5.1.8: Directed bright-field setup with polarizing filters (left) and polarized dark-field setup (right)

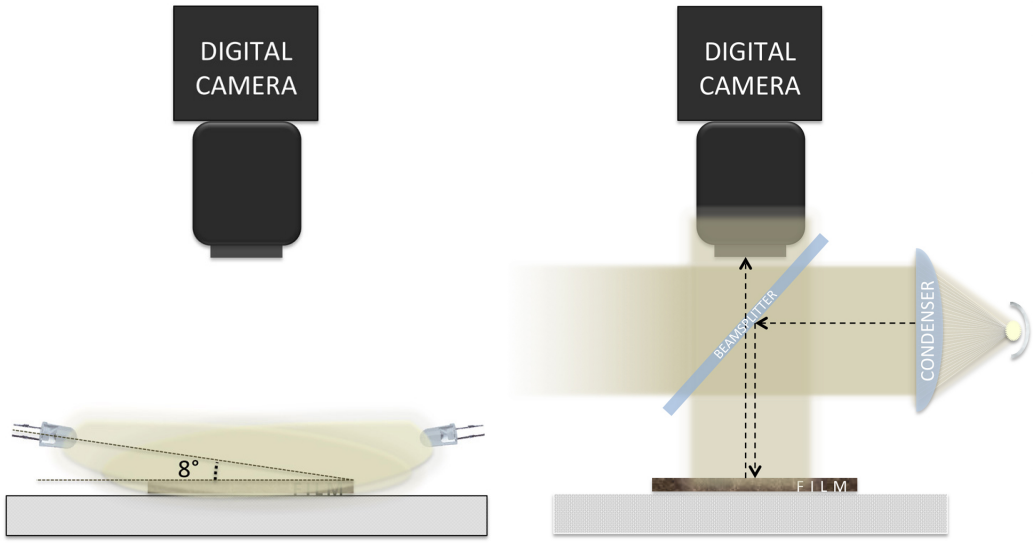

Figure 5.1.9: Reflection setups: raking light setup (left) and axial setup (right)

Raking light

The term "*raking light*" refers to an illumination almost parallel to the sample surface is intended (8° is often employed) (Fig. 5.1.9 - left). A homogeneous raking illumination from all possible directions around a sample can be provided by special light-rings, and the rays form a small angle with the sample surface. The raking light (also called "*grazing light*") allows light reflected by the front surface to be collected, thus emphasizing the visual effects of superficial structures and irregularities of the sample's surface. However, little or no information about the underlying layers is collected. In Figure 5.1.10, the case of a film affected by vinegar syndrome (ref. sec. 2.1) is reported. The part on the left is illuminated in bright-field and the image impressed in the emulsion is well highlighted; the part on the right is illuminated with raking light and the wavy grooves of 'channeling' are emphasized instead of the photographic image of the emulsion, which is barely visible.

Axial light

Gloss (sometimes called *luster*) is the extent of the specular reflection fraction of a surface. This is related to the degree of roughness, as a smooth surface appears glossy, while a rough one appears matte. The structure of a rough surface that influences the specular reflectance has micrometric size, and is invisible unless a high magnification is used. One method of eliciting gloss in a still image consists in acquiring the specularly reflected light. According to the laws of reflection, in order to acquire the specular reflection of a film, the camera and

Figure 5.1.10: A film affected by vinegar syndrome illuminated in bright-field (left) and with raking light (right) (sample source: Image Permanence Institute - digitized by the author)

the light rays have to be placed in such an arrangement so that they form the same angle with the normal to the film, and so that the light rays, the normal and the optical axis lie on the same plane. Due to this requirement, it is impossible to acquire the image using an orthogonal geometry ($0°/0°$), as the source-camera covering obstructs the acquisition.

A *beam-splitter* provides a solution to this problem; half of the incident light is directly transmitted and the other half is specularly reflected. A system composed by a light source, a collimating lens and a beam-splitter (Fig. 5.1.9 - right) provides an illumination composed of rays that are parallel to the optical axis. This method effectively elicits the gloss of a film.

The sample reported in Figure 5.1.11 is affected by ferrotyping in the bottom part (ref. sec. 2.2): this phenomenon is made evident with axial light, while it is not visible in a bright-field setup. The parts of the film characterized by a high specular reflection fraction appear bright, and no information about the underlying layers is collected.

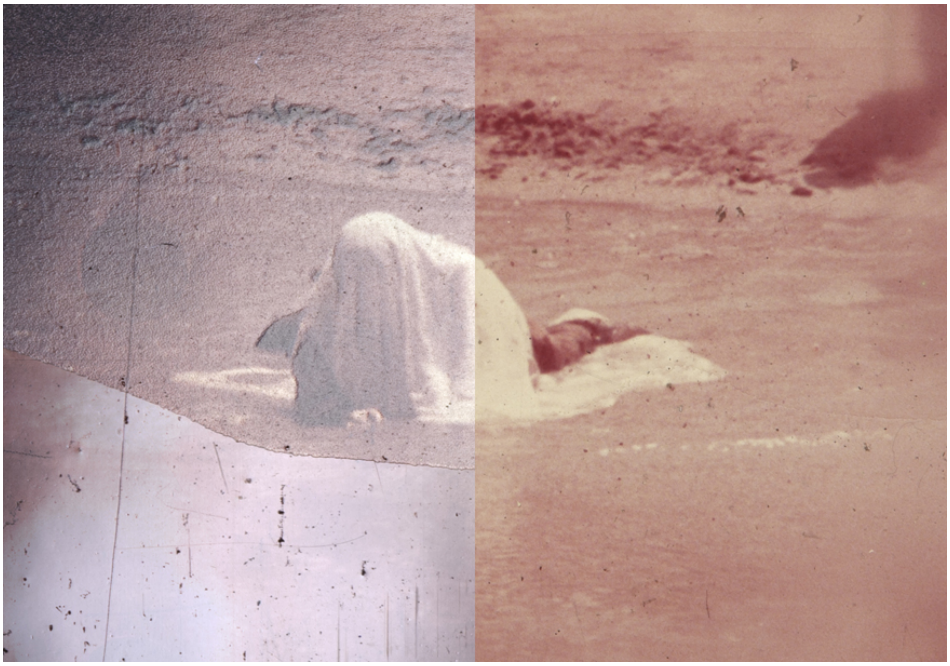

Figure 5.1.11: Ferrotyping highlighted using axial lighting (left part) (sample source: Image Permanence Institute - digitized by the author)

Chapter 6

Optical flaw detection

In the case of local flaws, the advanced solutions for the automatic digital restoration of photographic film are accomplished in two stages (Fig. 6.0.1): the *detection* stage, in which the flaws are pinpointed in the digital reproduction, and the *reconstruction* stage (*inpainting*), in which the values of the pixels corresponding to the deteriorated parts of the image are changed in order to put the restoration into effect. As these operations become more and more automated, restoration is becoming more affordable; this is especially the case for motion picture films, as a frame-by-frame manual restoration would be extremely burdensome for this.

In today's practice of digital restoration, the most effective methods for flaw detection are infrared radiation (e.g. Digital ICE) and spatio-temporal image analysis (sec. 3.2). While infrared radiation has the advantage of being effective both for still images and motion pictures, it should be noted that it only works for dye-based material. Spatio-temporal image analysis is relatively cheap, as no special scanning hardware is required, and it works on all kind of flaws (including copied ones). However, this method is only completely effective on mostly homogeneous areas of the scene, it has limits due to motion in the scene

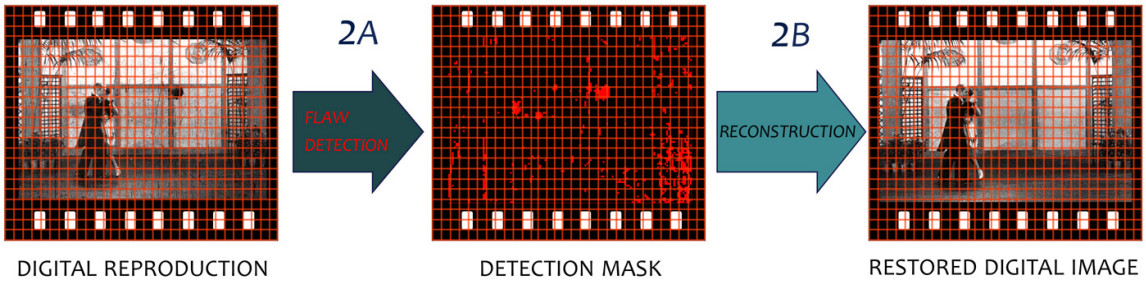

Figure 6.0.1: Flaw detection & reconstruction

and it is not effective for all defects appearing in the sequence over more than one frame (e.g. vertical scratches and lens dust). Moreover, the method is not applicable on still images.

The present chapter presents a range of methods for flaw detection applicable on silver-based as well as on dye-based material and on still images as well as on motion pictures.

We consider the image of a photographic film as being composed by two visual components: the photographic image of the emulsion is the main component and the flaws are a visual component superimposed on top of this.

According to a widely accepted code of ethics, as e.g. the code compiled by the *International Federation of Film Archives* [35], the reconstruction of the corrupted parts must be done with respect for the film as cultural property, thus being consistent with the intentions of its creators. In case major parts of the photographic image are obliterated, especially in the case of valuable assets, the restoration must be conducted under expert human supervision; automatic unsupervised operations by definition lack a comprehensive awareness of the guidelines [68]. In this thesis, the case of such highly damaged films are excluded, and we only consider films in which the flaw component affects a minor part of the frame.

If the flaw is highly detrimental to the image, the underlying emulsion component is completely obliterated; on the contrary, if the flaw component has a certain degree of transparency, the emulsion image, even if altered, is still visible. When using an unsupervised digital restoration, it is often inappropriate to use an inpainting algorithm to treat these transparent flaws, as this can wrongly alter the still visible emulsion component; hence, it is generally opportune to leave those flaws untouched.

The task of the detection stage is to classify all the pixels of the digital reproduction in two categories: "normal" or "flawed". Alternatively, the classification can assign the pixels to several categories that express the probability that the specific pixel is part of a flaw or its level of detriment. In the present work, we perform a binary classification. This categorization assists the reconstruction stage, by indicating exactly where the restoration is necessary and by preventing the obliteration of elements of the photographic image of the emulsion; in this way, the artifacts typical of the methods based on image analysis (sec. 3.2.3) are avoided.

The 'optical' methods seek physical evidence of the presence of foreign bodies or irregularities on the film. Contrary to basic image processing, in which all information used is contained in the conventional digital reproduction, optical methods require a second image acquired with a special machinery/setup that highlights the particular physical evidence investigated.

Effective illumination techniques, adequate image processing and appropriate computational photography procedures are examined in the following. Some of the procedures presented entail the acquisition of a single image with a particular illumination technique (sec. 6.1). Other procedures presented, on the other hand, entail multiple acquisitions followed by

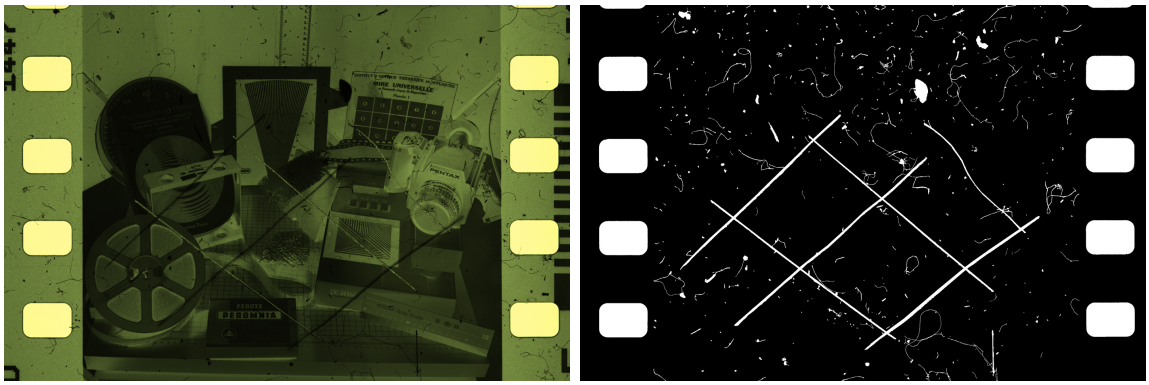

Figure 6.0.2: A digital reproduction of a photographic film and its detection-mask

the combination of the images acquired; the latter type of procedures are classified as '*computational photography*' methods (sec. 6.2).

In the following, we refer to the unprocessed acquired images (single or multiple) with the term "*prime-image*". Regardless of the procedure adopted, the prime-images undergo processing that transforms them into a binary image. This image expresses the classification of the pixels into the two categories 'normal' or 'flawed'; we refer to this image with the term *"detection mask"* (Fig. 6.0.2).

6.1 Single acquisition flaw detection

6.1.1 Illumination methods for flaw emphasis

By reviewing section 5.1, we select the illumination techniques that have the capacity to suppress the image impressed in the photographic emulsion and to emphasize the presence of dust and scratches. The bright-field setups are excluded since they do not suppress the photographic image of the emulsion. The reflection setups are also excluded since they only provide information for features of the front surface, and thus the flaws of the opposite side cannot be detected. It is very often the case that dust and scratches do not entail any optical activity; therefore, the adoption of a polarized bright-field setup for automatic flaw detection would cause many missed detections and, for this reason, we decided to also exclude this illumination technique from the treatise. In spite of this problem, a flaw detecting device with a polarized bright-field setup was patented in 2003 [69].

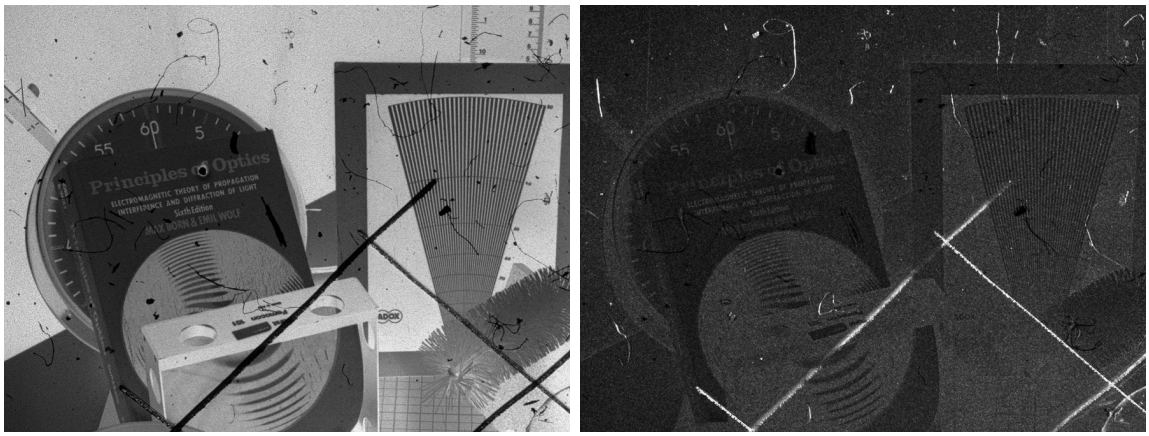

Figure 6.1.1: A sample with dust and scratches illuminated in bright-field (left) and in dark-field (right)

Dark-field setup (sec. 5.1.3)

The irregularities of the surface of a film due to dust and scratches cause the incident light to be deviated in random directions; therefore, in a dark-field setup, a signal for flaws would be produced [70].

In Figure 6.1.1, the images of a sample affected by dust and scratches are reported for bright-field and for dark-field illumination. The photographic image of the emulsion is partly suppressed and the flaws are bright; however, due to the high scattering fraction of the silver emulsion, the brightness differentiation between silver and flaws is not very high.

Polarized dark-field setup (sec. 5.1.4)

The experiment described in section 4.3 indicates that the depolarization of light scattered by silver particles is lower for forward scattering than for backward scattering and, therefore, a polarized dark-field setup may further suppress the image of the emulsion. As a matter of fact, in case the light scattered by dust and scratches is depolarized to a greater extent than the light scattered by silver particles, the adoption of polarizers in a dark-field setup enhances the brightness differentiation between silver and flaws.

Prior to 2010, there is no documentation that reports on the use of this combined illumination technique for dust and scratch detection on photographic film [11].

In Figure 6.1.2, the images of the sample (the same of Figure 6.1.1) are reported for bright-field and for polarized dark-field setups. The comparison of Figures 6.1.1 and 6.1.2 shows that the adoption of polarizing filters further suppresses the photographic image of the emulsion and that a larger number of flaws produce a significant signal.

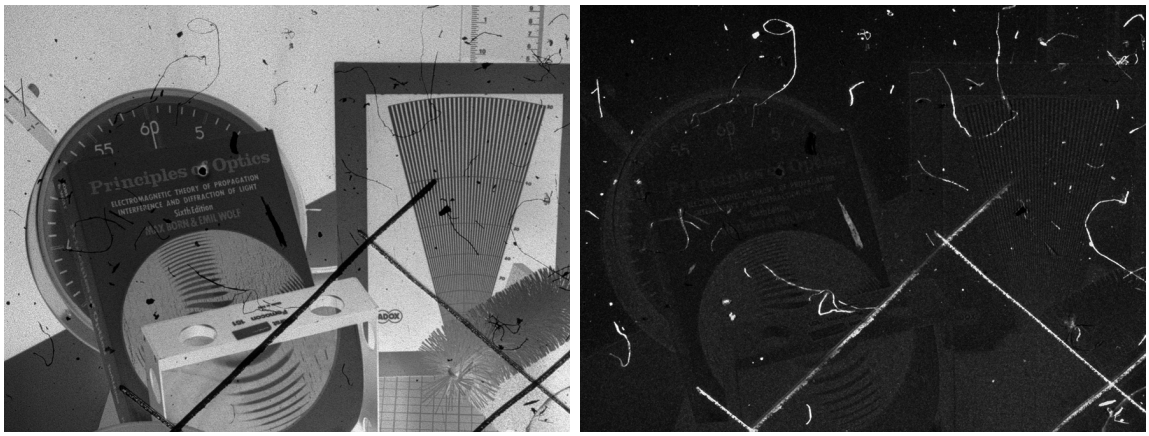

Figure 6.1.2: A sample with dust and scratches illuminated in bright-field (left) and in polarized dark-field (right)

Total internal reflection

It is worth mentioning the attempt to use the phenomenon of *total internal reflection* with the aim of flaw detection, even though it did not give a positive result in the end.

When a propagating wave strikes the boundary between two media and passes from a higher to a lower refractive index, total internal reflection may occur according to the incidence angle, and light can be completely specularly reflected in a mirror-like manner. Bearing this in mind, a photographic film was enclosed between the flat faces of two borosilicate crown prisms; the refractive index of the borosilicate ($\backsimeq 1.4$) is lower than the refractive index of the photographic emulsion ($\backsimeq 1.6$). The presence of a scratch on the film, which is a sort of engraving, creates an air gap between the film and the prism. A simplistic way to model the situation would be to assume direct contact film/borosilicate for the intact film and a double boundary borosilicate/air/film at a scratch (Fig. 6.1.3); if the film were illuminated through the prism with an angle of incidence higher than the critical angle borosilicate-air ($\backsimeq 46°$), it would be theoretically possible to have total internal reflection only at the scratches.

If this model were correct, then the total internal reflection would provide useful information to precisely locate the scratches. In reality, the direct bonding of the flat extended surfaces of two different solids is a complex issue. In addition to both surfaces needing to be exactly conformal, the surfaces must also be extremely clean and free from any small contamination that would prevent or weaken the bond and create an air gap between the borosilicate and the film. This gap would be eliminated only through the use of binder, balsam or glue. Due to these complications, we eliminated 'total internal reflection' as a potential phenomenon for use in flaw detection.

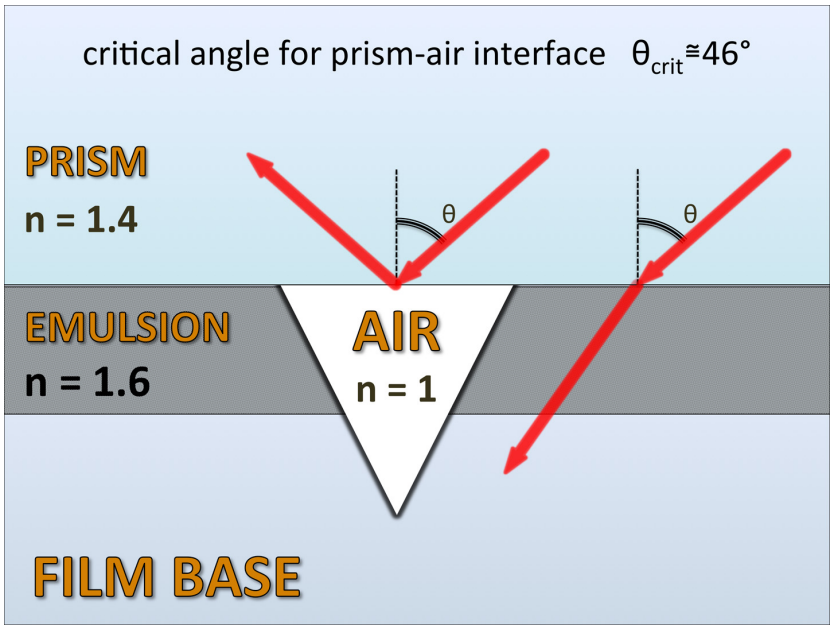

Figure 6.1.3: Simplistic model for film-glass total internal reflection

6.1.2 Binary detection-mask

In order to put the flaw detection into effect, a binary detection-mask has to be created. To fulfill this task, a thresholding operation is carried out on the prime-image acquired with the specific illumination adopted. For the methods described in section 6.1.1 a simple '*threshold-above*' is necessary: the pixels of the image are labeled as a "flaw" if their value is greater than a certain value (*threshold*) and otherwise, they are labeled as "normal". The key parameter in this process is the choice of the threshold; for this reason, the stronger the differentiation between the signal of the emulsion image and the signal of the flaws, the less critical the choice of the threshold value will be.

Assuming that the flaws affect a minor part of the frame (as discussed in the beginning of the chapter), the dark-field prime-images will be mostly dark. A typical example of the histogram of these images is reported in Figure 6.1.4 in logarithmic scale; the peak represents the emulsion image that is not entirely suppressed, while the tail in the higher values represents the irregularities of the film surface (i.e. the flaws). To choose the threshold, the peak position is identified (value 33 in the example of Fig. 6.1.4) along with the relative count (407120): starting from the peak bin, we move toward the higher values until the current bin count becomes lower than a predetermined fraction[1] ($1/100$) of the peak bin count (4071). The first bin that satisfies this condition (79) is the selected values for the "threshold-above" operation, and the detected flaws correspond to the pixels whose

[1] refer to sec. 7.2 to find out how this fraction was determined

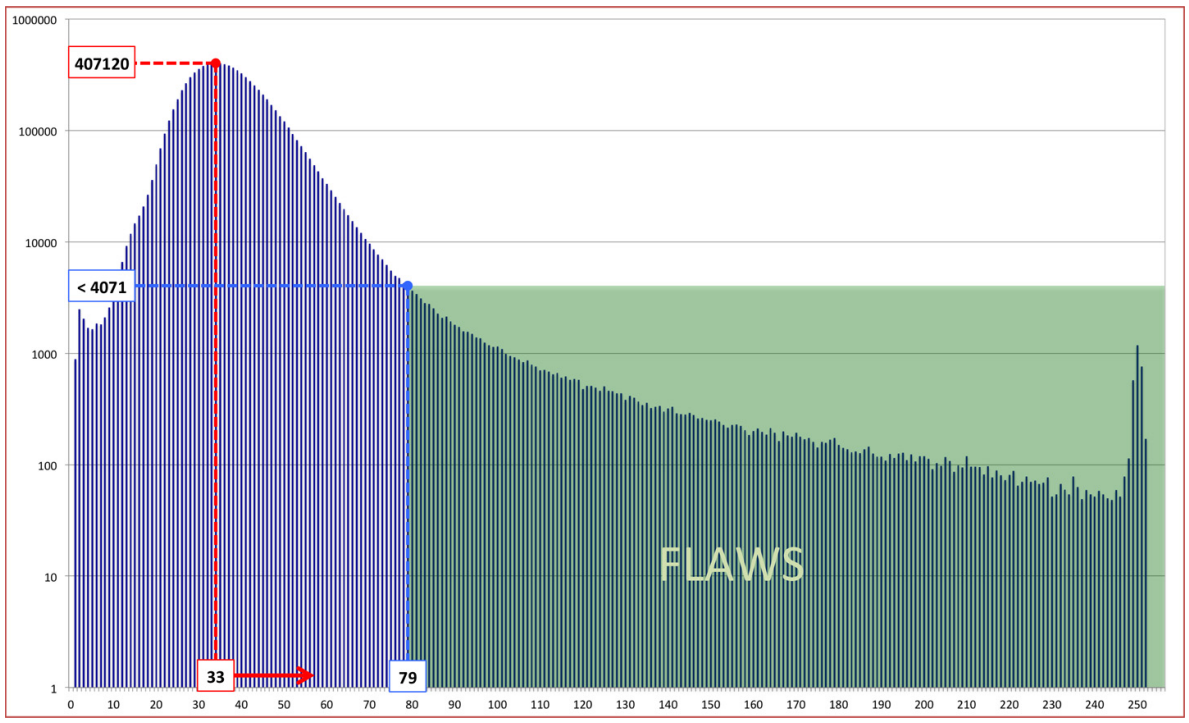

Figure 6.1.4: Typical histogram of the prime-image acquired in a dark-field setup (log scale) - The "threshold-above" operation

value is greater than or equal to that value (≥ 79).

In case the prime-images are characterized by an uneven illumination or in case the differentiation emulsion-flaws provided by the illumination technique adopted is not strong enough, an '*adaptive thresholding*' may improve the flaw detection [71]. This procedure entails splitting the image into several sub-images and applying a different threshold to each sub-image.

The threshold-above operation (adaptive if needed) is carried out and the corresponding pixels are classified as flaws.

6.2 Computational photography flaw detection

6.2.1 Effects of the variation of the illumination direction

The capabilities of dark-field illumination have been described above; by varying the angles θ and ϕ indicated in Figure 6.2.1, countless different dark-field setup can be realized.

Structures and irregularities in the film produce shadows and glows that change position according to the provenance of the light beam [72]; both film grain and flaws entail such an effect.

When imaged, silver particles appear to bank up in a random texture (the '*film grain*') with elements ranging in size from 10 to $30\mu m$; using a sampling density of $3200ppi$, the grain appearance is barely resolvable. By acquiring registered images with different provenances of the illumination, the pattern of the film grain (consisting of its glows and its shadows) shifts by few pixels or none at all. On the other hand, dust and scratches are problematic when the order of magnitude of their size is hundreds of microns or higher; by varying the direction of illumination in an image of $3200ppi$, the position of glows and shadows of such flaws can shift by several pixels.

An example is reported in Figure 6.2.2; a sample with sharp scratches on the base side is acquired twice with the emulsion facing the camera, once with $\theta = 70°$ and $\phi = 0°$ and a second time with $\theta = 70°$ and $\phi = 180°$ (ref. Fig. 6.2.1). The unblemished parts of the film look similar in the two images, while the scratched parts look different.

In this particular case, a shadowing effect is revealed. The sketch in Figure 6.2.3 explains how the scratches cast shadows on the underlying emulsion.

A shadow appears beside a scratch; the shift of the shadow with respect to its scratch depends on the direction of the beam. The scratch blocks the collimated rays and creates a shadow on the emulsion that acts as a screen. Considering a film base with thickness $0.125mm$ and refractive index 1.5, the length of the segment A in Figure 6.2.3 can be predicted using the *Snell's law* and a simple trigonometric calculation.

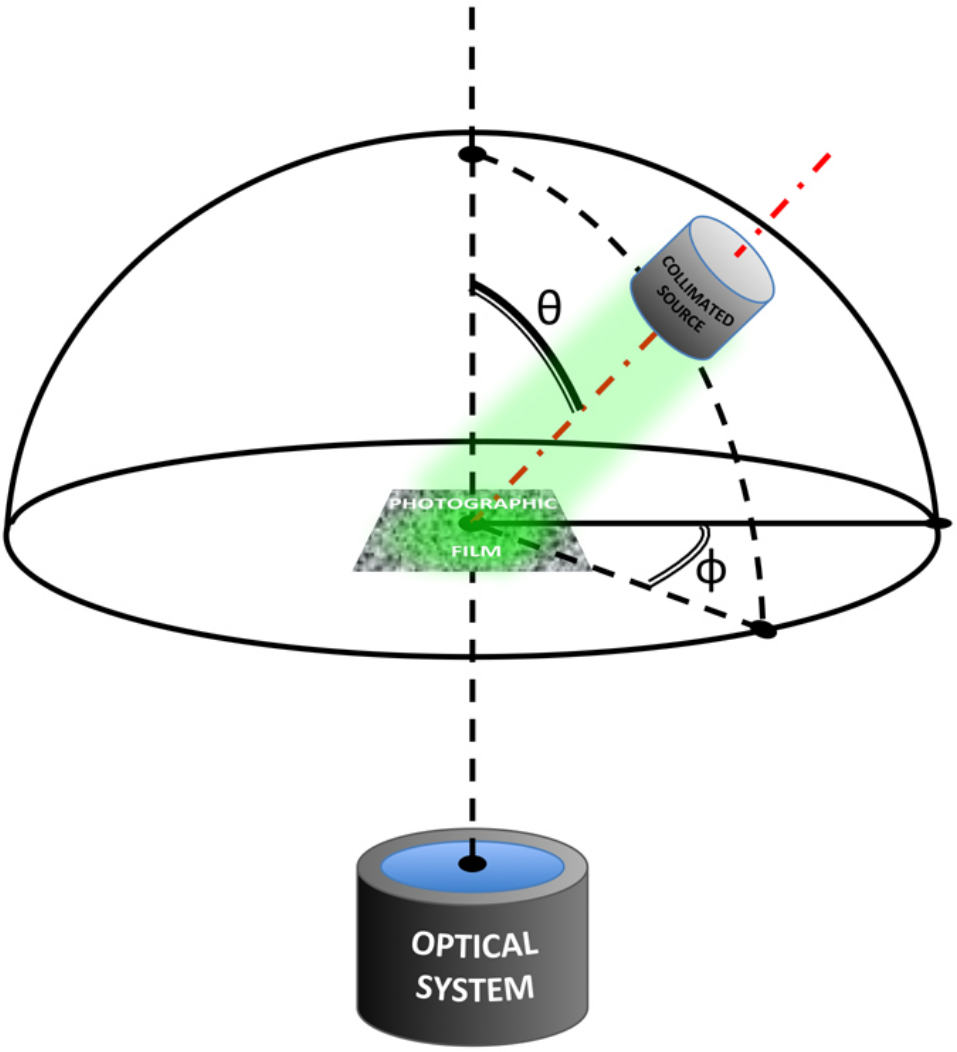

Figure 6.2.1: Dark-field setup with a single collimated source

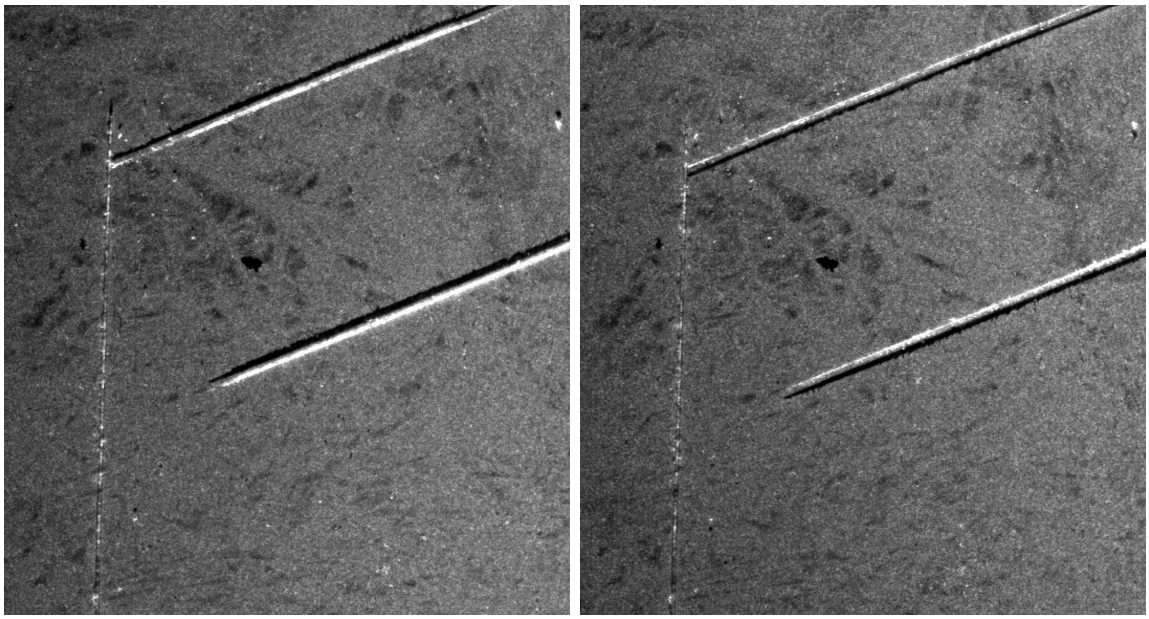

Figure 6.2.2: The same film acquired with two different illumination geometries

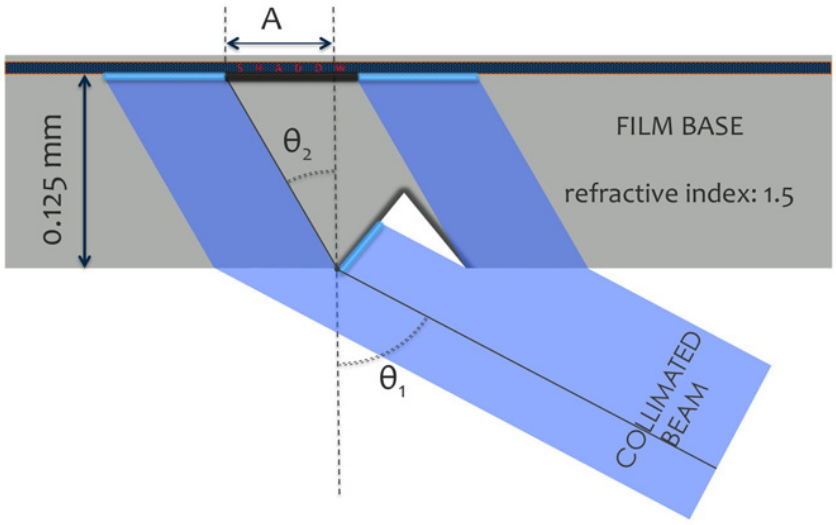

Figure 6.2.3: Model of the shadowing effect

$$\theta_2 = \arcsin(\frac{\sin\theta_1}{1.5})$$

$$A = \tan\theta_2 \times 0.125$$

The result for $\theta_1 = 70°$ is $A = 0.10mm$.

Now we compare this theoretical value with the empirical one. In the images of Figure 6.2.2, the number of pixels that constitute the segment between a scratch and its shadows is around 13; since the image was acquired using $3200ppi$, this amount of pixels correspond to $0.10mm$. The theoretical and empirical data match very well.

6.2.2 Direction-computational photography

In view of the phenomena previously described, we draw our conclusion that an effective method to produce a good detection-mask is the acquisition of multiple images of a photographic film with different geometry of illumination and the extraction of the differences between the images.

In this matter, it is important to consider that, according to their structure and orientation, the flaws are more evident using certain directions of illumination than others. An example is reported in Figure 6.2.4: the vertical scratches present on the sample are effectively detected by extracting the differences between images in which the illumination was orthogonal to the scratches (W and E). On the other hand, the same vertical scratches are not detectable by extracting the differences between images acquired illuminating the film parallel to them (N and S).

Cardinal acquisition

Considering these factors, we developed a novel computational photography method for flaw detection. Four different digital images are acquired in a dark-field setup, illuminating the sample uniformly with a collimated source from four different directions; θ is constant and $\phi = 0°, 90°, 180°, 270°$ (ref. Fig. 6.2.1). The illuminating sources and the corresponding images are indicated with the cardinal points: N, S, W and E (Fig. 6.2.5).

Thanks to the dark-field setup, the photographic image of the emulsion is partly suppressed and the flaws are bright in all the four prime-images. Moreover, the four images are similar in the areas corresponding to the unblemished emulsion, whereas they differ in the positions of the flaws, according to the direction of provenance of light. The extraction of the differences between N and S images draws the horizontal components of the flaws, whereas the vertical components are drawn with the analysis of the differences between W and E.

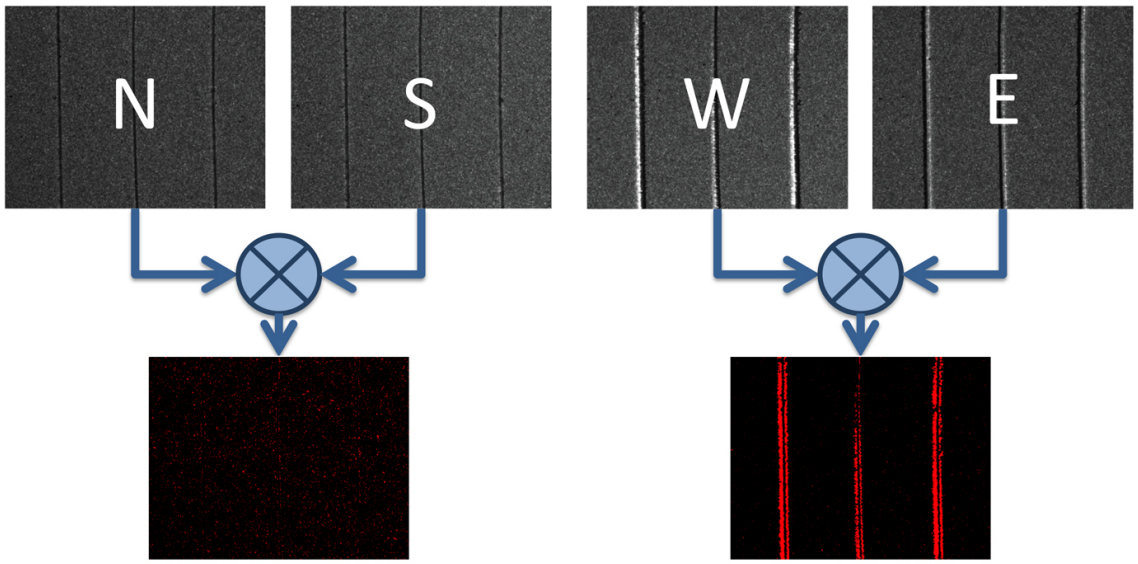

Figure 6.2.4: Cardinal acquisition and difference extraction

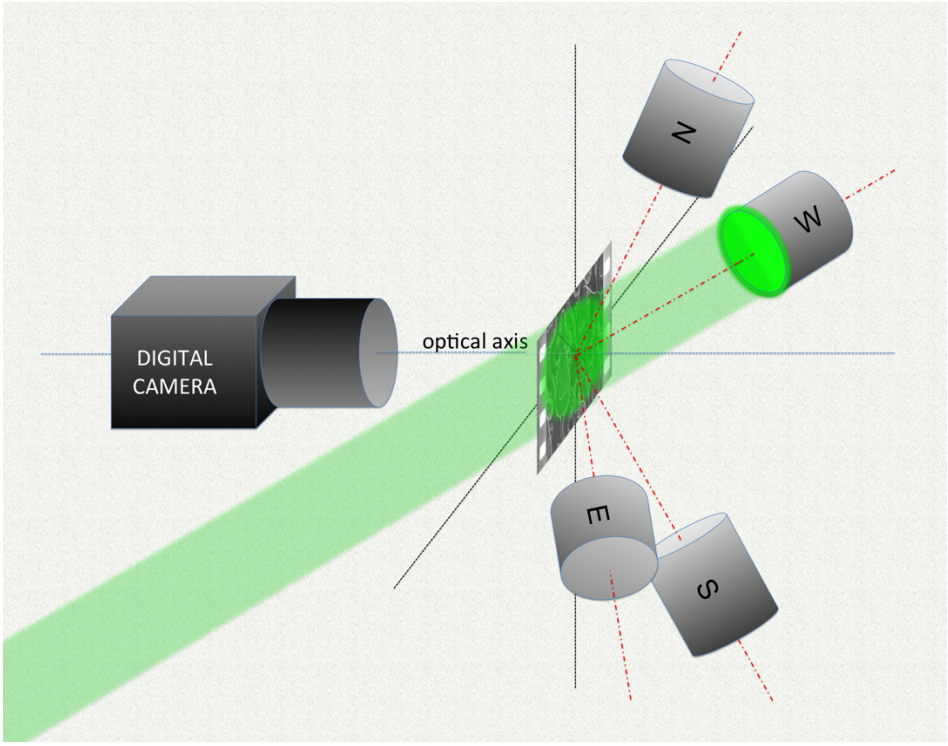

Figure 6.2.5: Cardinal acquisition setup

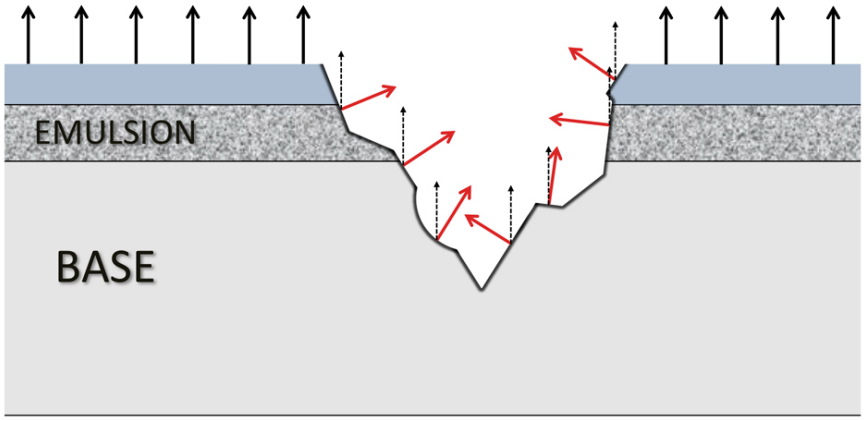

Figure 6.2.6: Section of a scratch and the deviation of the normal (red arrow) of its point from the film normal (black arrow)

An effective tool to analyze and extract the difference between images is provided by *Multivariate Image Analysis*; the process is described in section 6.2.4.

Multi-direction acquisition

The differences between images acquired with different illuminating directions are related to the local deviation of the surface normal from the normal of the intact film surface. An irregularity in the film surface, due to a scratch or a dust grain, can have any shape and, therefore, the deviation from the film normal for different points can also vary widely; the case of a scratch is reported in Figure 6.2.6.

In an image of a photographic film, every point of a flaw will glow depending on the relation between the local surface normal and the direction of illumination. The greater the number of directions that are used by the computational photography method, then the more probable it will be that the flaws will be completely highlighted in all their parts; in fact, by including a larger number of illumination directions, it is likely that the proper direction for each local deviation from the film normal will be achieved. For these reasons, another setup was developed in which several LED sources were homogeneously spread in a semi-sphere, with the film is lying in its center (Fig. 6.2.7).

This was realized by mounting a set of LEDs on a dome characterized by a black matte surface. An image was acquired for each LED and the differences between the images were extracted through *Principal Component Analysis* (sec. 6.2.4).

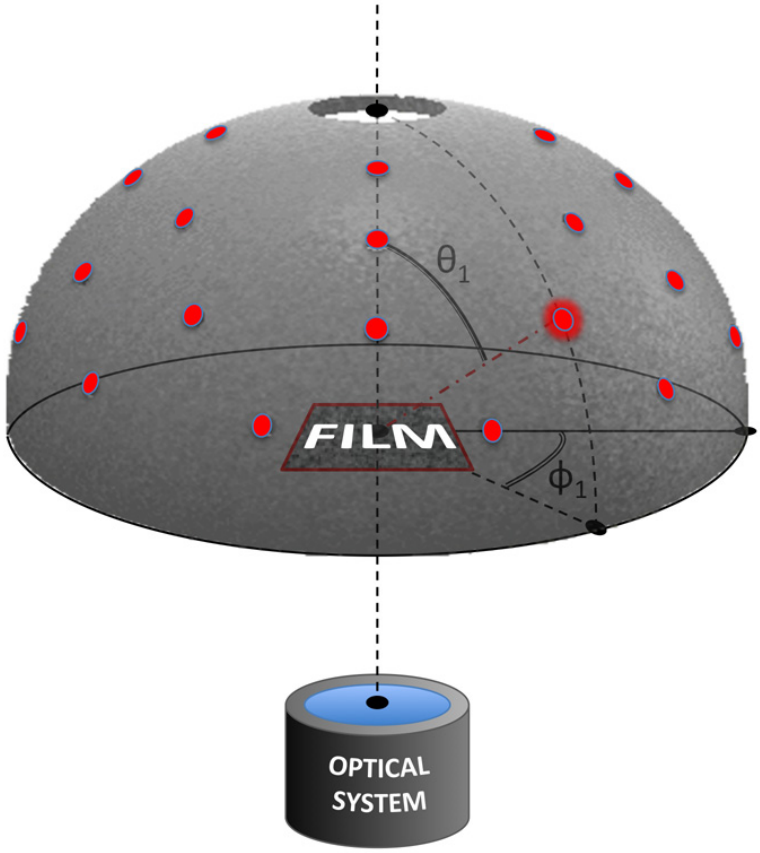

Figure 6.2.7: The multiple-direction setup: the red dots indicate the positions of the sources

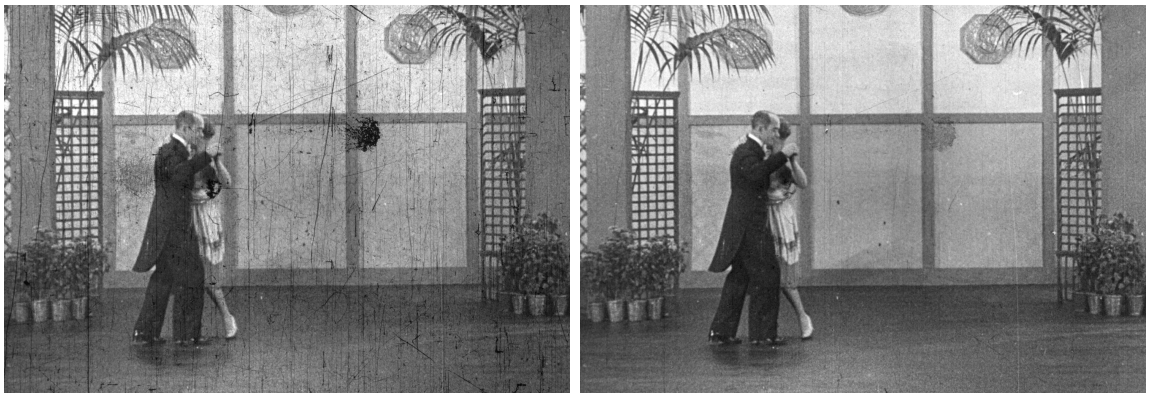

Figure 6.2.8: The same frame acquired in a directed bright-field setup (left) and in a diffused bright-field setup (right) (sample source: David Pfluger - digitized by the author)

6.2.3 Collimation-computational photography

As described in section 5.1.1, a crisp image is obtained when a condensed bright-field illumination setup is used. In this crisp image, the film grain is emphasized together with dust and scratches. On the other hand, when a diffused bright-field is adopted, the image has less sharpness and contrast, although blemishes on the film are much less visible (Fig. 6.2.8).

If we adopt a sampling density of $3200ppi$, the grain appearance in the image is barely resolvable, while dust and scratches are bigger and well visible. As a consequence, the main differences between the two images are the flaws, and the extraction of these differences was found to be effective for flaw detection. This is essentially the same principle as that on which the technique reported in section 3.2.5 (D/SCO) is also based.

As in direction-computational photography, the differences can be extracted through a *Principal Components Analysis*; the process is described in the next section.

6.2.4 Difference extraction through PCA

The steps we adopted to perform Principal Component Analysis (PCA) are described in Appendix A. When the procedure is carried out on a set of N images, the output consists of N new images which are the result of particular linear combinations of the original images (the 1-D matrices $\mathbf{D}$ in Appendix A conveniently rearranged).

In many applications (e.g. image compression), PCA is used to reduce the dimensionality of a data set, that is, selecting the eigenvectors with the highest eigenvalues. In our procedure, PCA is used to extract the differences between images acquired in different illumination conditions (secs. 6.2.2 and 6.2.3) and thus, a completely different approach is adopted. A

similar approach has already been used in agricultural engineering for extracting superficial defects from sets of images -of the same object- acquired with different illumination [73].

According to the dissertation in the beginning of the chapter, we assume that the flaws affect a minor part of the frame. In both computational photography techniques described in sections 6.2.2 and 6.2.3, the major contribution of the emulsion's photographic image causes the acquired prime-images to be quite similar, and thus they have high correlation coefficients. As a consequence, for such a set of images, the eigenvector with the highest eigenvalue is generally found to be in the positive hyper-octant, in which all the components are positive. The image values corresponding to this eigenvector are a weighted mean of the values in the original prime-images, and the photographic image of the emulsion remains visible. PCA's prerequisite of mutual orthogonality causes all the remaining eigenvectors to have a similar amount of positive and negative components; these eigenvectors actually take into account all of the differences between the original images, and these differences correspond to the flaws in the film.

In Figure 6.2.9, the results of the application of PCA are reported for the case of cardinal acquisition, as described in section 6.2.2. The four eigenvectors (eigenimages) and the corresponding eigenvalues are calculated for the four acquired images N, S, W and E (see Appendix A for details).

By looking at the components, we observe the following: the first eigenvector is close to the diagonal of the positive hyper-octant, since all the illumination directions contribute positively to a similar extent; for the second eigenvector, the vertical illuminations (N and S) and the horizontal illuminations (W and E) contribute opposingly to a similar extent. The other two eigenvectors essentially combine only two of the four cardinal images: the third combines W and E opposingly and the fourth combines N and S opposingly (the factors of the other components are small).

The data projected on these vectors are rearranged in digital images (lower images in Fig. 6.2.9). The first image ($EV1$) appears quite similar to the original ones; in the other three images ($EV2$, $EV3$ and $EV4$), the photographic image of the emulsion has disappeared in a relatively homogeneous mid-gray and only the marks of the defects remain as a deviation from the mid-gray. Flaw detection is performed using these last images, and $EV1$ is excluded since it does not suppress the photographic image of the emulsion.

At this stage, it is necessary to establish which of the three remaining images should to be selected. Considering the total number of pixels deviating (over an opportune threshold defined with a procedure described in the following section) from the mid-grays in all the three images, we calculated the cumulative percentage of deviating pixels for the succession $EV2 - EV3 - EV4$. The image $EV2$ alone contributes to 80% of the deviating pixels; the inclusion of $EV3$ adds another 15%; the inclusion of $EV4$ adds the remaining 5%. All of these percentages are significant and hence, all of the three eigenimages are potential contributors to flaw detection. For the above reasons, it is advantageous to use the infor-

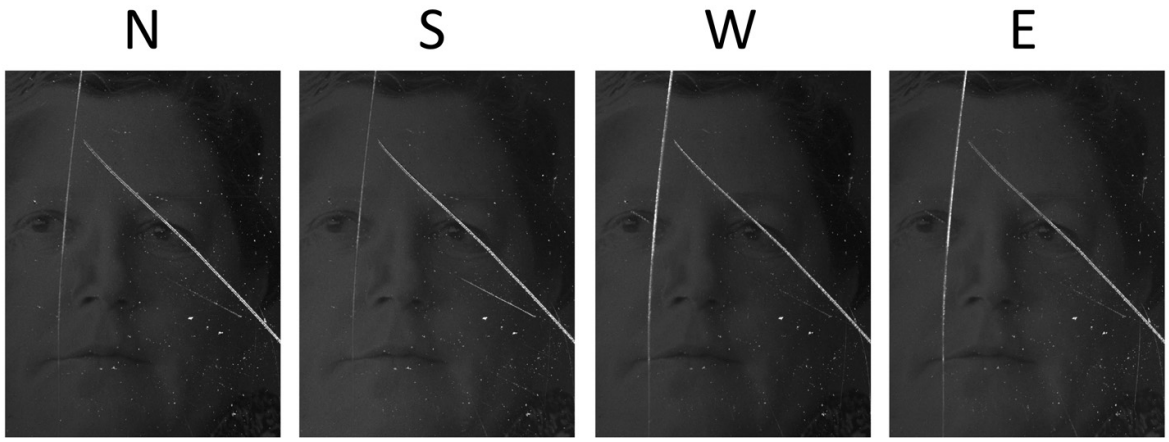

PCA	1st eigenvector	2nd eigenvector	3rd eigenvector	4th eigenvector
N	0.5095	-0.5256	0.0289	-0.6806
S	0.4965	-0.4625	0.0654	0.7316
W	0.5183	0.459	-0.7215	0.0029
E	0.4745	0.5469	0.6887	-0.0379
eigenvalue	**339265.34**	**30675.67**	**27964.76**	**24620.48**

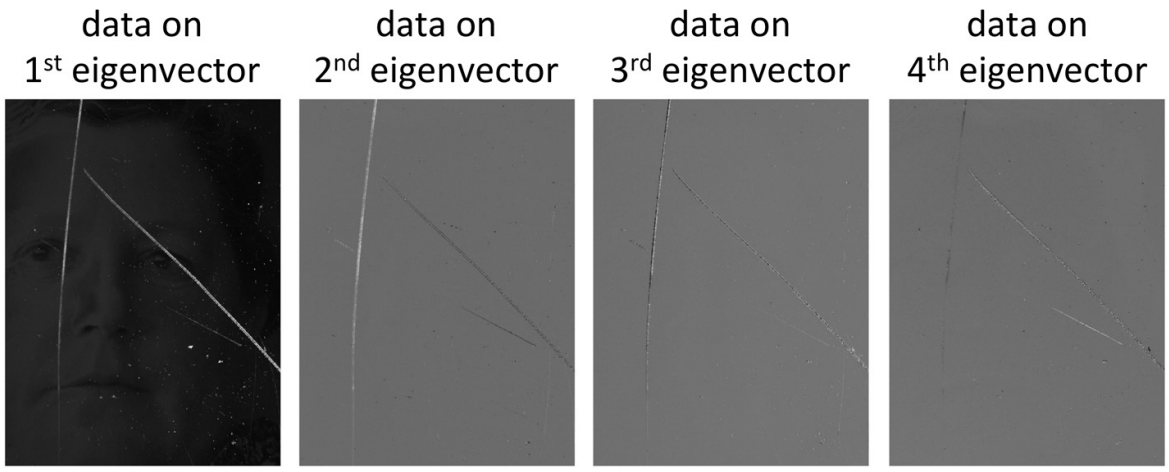

Figure 6.2.9: Example of the results of PCA for the case of cardinal acquisition

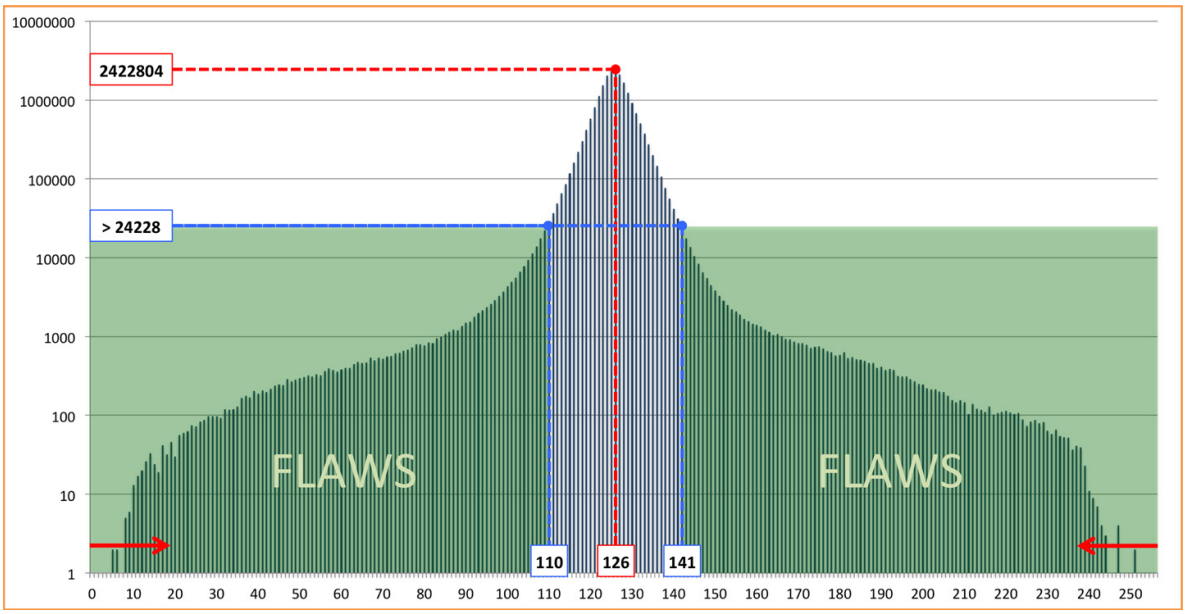

Figure 6.2.10: Threshold-outside

mation from all of the remaining eigenimages for the extraction of the differences between the prime-images.

6.2.5 Binary detection-mask

Contrary to the dark-field images (sec. 6.1.2), the eigenimages require a different thresholding operation to create the binary detection-mask. In this case, a '*threshold-outside*' operation is needed: the pixels of the image are labeled "flaw" if their value is lower than a certain value (*low threshold*) and greater than another value (*high threshold*). Otherwise, the pixels are labeled "normal".

After the histogram of the image is built, the peak of the mid-gray is identified (value 126 in the example of Fig. 6.2.10) along with the relative count (2422804); starting from the outer bins (bin-0 and bin-255 considering $8bits$), we move toward the mid-gray peak bin until the current bin count becomes higher than a predetermined fraction ($1/100$ - ref. sec. 7.2) of the peak bin count (24228). The two bins that satisfy this condition (one for the 0-bin and one for the 255-bin starting point) are the selected values for the threshold-outside operation (values 110 and 141). The corresponding pixels are classified as flaws.

In case the original acquired images are characterized by diversified uneven illuminations, the eigenimages may be affected by an uneven mid-gray; in such cases, an 'adaptive thresholding' (different thresholds for different parts of the image) may improve the flaw detection.

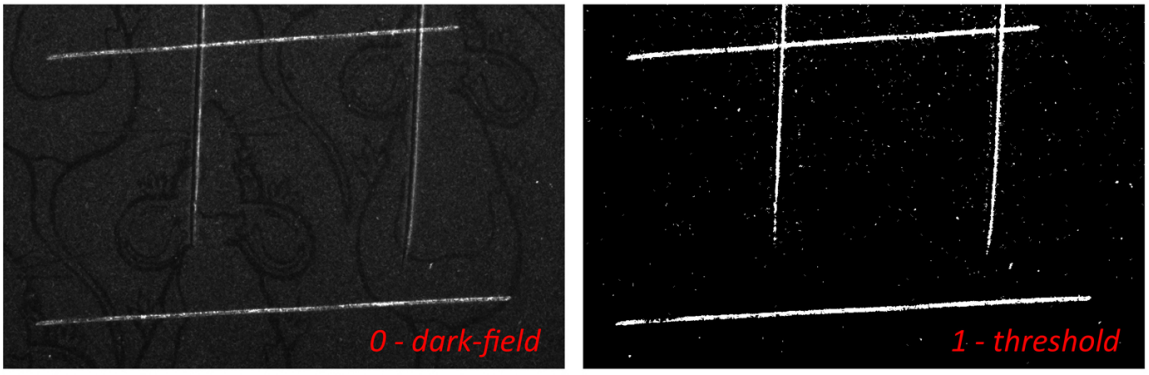

Figure 6.3.1: An image obtained with a dark-field setup before and after thresholding

The threshold-outside operation (adaptive if needed) is carried out on each of the selected eigenimages and the results are added together in inclusive disjunction (OR) into a unique detection mask.

6.3 Flaw-size threshold

The binary images that result from the thresholding operations described in sections 6.1.2 and 6.2.5 indicate the detected flaws of the film.

These images may contain, in addition to the correctly detected flaws, erroneous elements in the form of a spread of randomly distributed little points (Fig. 6.3.1). The presence of these erroneous elements can be caused by the structure of the silver grain that was not completely suppressed or by the electric noise in the prime images. An effective solution to remove these randomly distributed points is to exclude the structures smaller than a certain area. The 4-step procedure to accomplish this task is described with an example in Figure 6.3.2.

A *connected-components-labeling* (CCL) is performed on the rough binary detection-mask (**1 - threshold**), produced with the thresholding operation (secs. 6.1.2 and 6.2.5), and the elements are identified [74],[75]. A size threshold applied on the labeled elements would be sufficient to select the elements larger than a certain number of pixels ("*cleansing*").

However, it is often the case in the detection-mask that not all the parts of a correctly detected flaw are connected together and, therefore, the CCL identifies the flaw with multiple labels; in this case, the size threshold would also cleanse these unconnected parts of flaws that were actually correctly detected. To avoid this, a preliminary *dilation* prior to the size threshold is effective; the elements labeled in the first stage are dilated to fill the fractures in the flaws (**2 - dilated**) and a second CCL is performed. Afterwards, the size threshold

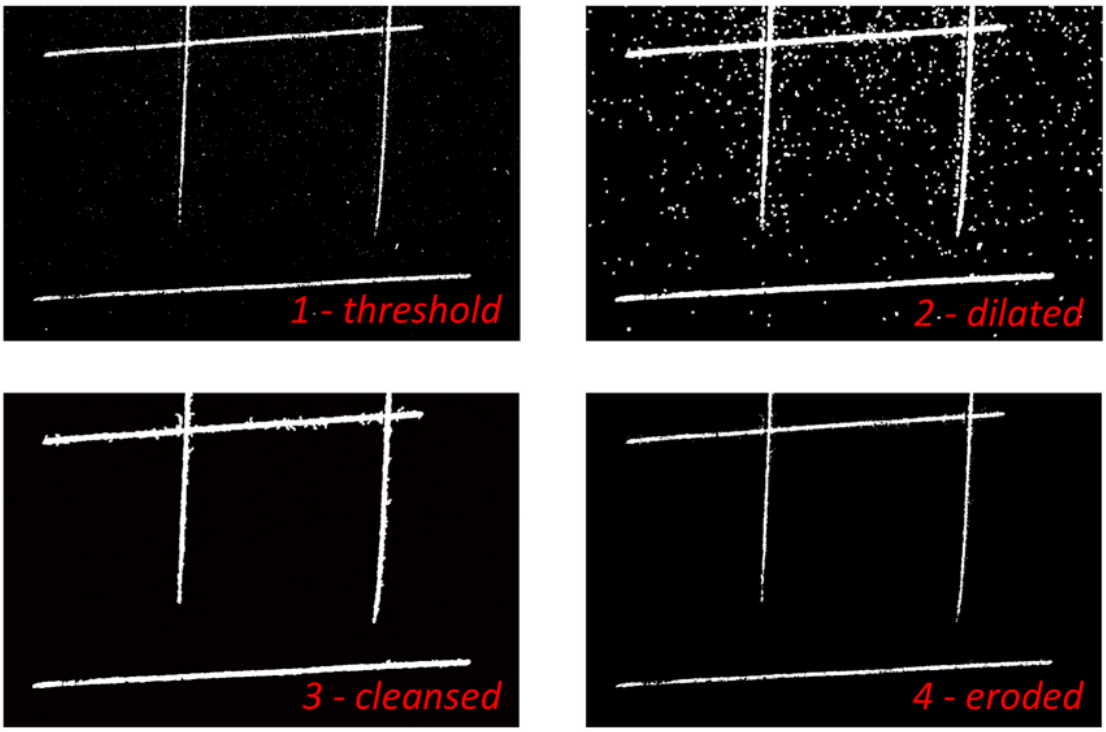

Figure 6.3.2: Operations for the selection of the elements over a size threshold

is applied to the elements (**3 - cleansed**). Eventually, it is necessary to perform an *erosion* to return to the undilated cleansed image (**4 - eroded**).

In addition to excluding the erroneous bright points, the cleansing has additional benefits for flaw detection. When the flaw detection is based on dark-field illumination, parallax effects could slightly shift the detection with respect to the effective position of the flaws in the bright-field digital reproduction, which eventually is the image to be inpainted. The selection of the flaw elements larger than a certain dimension guarantees more clear and consistent results (see the next chapter for details).

Moreover, the cleansing operation is a practical application of the principle of "minimal intervention". According to this principle of ethical restoration [35], the reconstruction should alter the original information only if absolutely necessary; as a matter of fact, when a flaw is very small, it does not truly compromise the proper use of an image and, therefore, it is better to leave the corresponding part untouched, rather than inpainting it with arbitrary information.

Chapter 7

Detection evaluation

The previous chapter described in detail a set of methods for the effective detection of flaws on photographic film. It is necessary to evaluate the detection provided by these methods in order to confirm whether or not they are valid, and in order to define all of their best parameters. For this purpose, comparative tests need to be arranged in which the detection-mask (i.e. the binary image that classifies all of the pixels and labels them "normal" or "flaw") produced by a certain method is compared to the binary image that indicates the 'true' flaws of the film frame under consideration.

In order to evaluate whether or not a flaw is true, an assessment conducted by an operator is required, in which its direct observation of the film and its assessment of the detriment are used. The operator should only label the pixels "flaw" where a significant part of the photographic emulsion image is corrupted; the labeling should avoid transparent flaws, in which the emulsion is still visible, and very small flaws, in which the proper use of the image is not seriously compromised. This meticulous human labeling operation was carried out using a graphics software, starting from an image acquired in a directed bright-field setup, in which the flaws are well distinguishable; the resulting binary image is called "*ground-truth*".

A pixel-to-pixel comparison between the detection-mask and the ground-truth provides a numerical assessment of the performance of the flaw detection. For each pixel of the image, four cases are possible:

Detection-mask	Ground-truth	Result
1	1	Successful detection
1	0	False detection
0	1	Missed detection
0	0	Void

The statistics of these results define the performance of the detection. We consider the number of successful detections (**SD**), false detections (**FD**), missed detections (**MD**) and voids (**V**); we also consider the total number of 1 values in the ground-truth (**f**) and in the detection-mask (**d**). The percentage of flaws correctly detected (**%SD/f**) and the percentage of detections that are false (**%FD/d**) can be considered as two effective indicators. In addition to these two percentages, a unique indicator is also necessary; the *Matthews Correlation Coefficient* (MCC) is a number that spans from -1 to 1 and takes into consideration the number of successful, missed, false detections and voids [76]:

$$MCC = \frac{(SD \times V – FD \times MD)}{\sqrt{(SD + FD) \times (SD + MD) \times (V + FD) \times (V + MD)}}$$

The higher the MCC, the better the detection.

7.1 Image registration

When images of the same subject have different viewpoints and their data have to be compared and/or integrated, *image registration* is necessary to guarantee that equivalent pixels in different images correspond to the same point of the subject (same coordinate system).

In the case of the computational photography techniques described in sections 6.2.2 and 6.2.3, the data of multiple prime-images integrate together to create a detection mask; in any of the techniques, regardless of the method examined, the comparison detection-mask/ground-truth is a necessary step in the experimental pipeline we defined. Should the images not have exactly the same coordinate system, it is necessary to implement image registration in our experimental pipeline.

If the sample or the imaging system are moved between different acquisitions, even if we were to strive to re-create the same framing, it is very difficult to avoid misregistrations (to this end, consider that with $3200ppi$, a $8\mu m$ translation in the object plane results in

a translation of 1 pixel in the digital image). Initially we allowed repositioning during the acquisitions of the images used for a specific frame, and a semi-automatic image registration tool was developed; the tool consists in a computer algorithm that refines the approximate location of a set of control points indicated by a user (ref. to the forthcoming section). The procedure developed is accurate, and provides a good image registration; however, a residual misregistration is often the case, due to the fact that (I) we considered only *Projective transformations* [77] (thus lens distortions and film deformations were not reversible) and (II), by changing the illumination direction, features of the film may shift their position in the images; if these features are used for registration, the consequence of this second fact is that the registration actually seeks to compensate the apparent shift of the features, and the result does not correspond to a real match of the coordinate systems.

As a matter of fact, the direction-computational photography methods rely on the apparent shift of the flaws; therefore, this image registration would jeopardize the methods of section 6.2.2. For these reasons, we eventually decided to avoid repositioning, and we acquired all the images of a single frame without moving the camera or the film (only illumination manner changes); this way, perfectly registered images were acquired. Nevertheless, the challenges that arose in the development of the registration procedure and the strategies to take them on deserve to be reported here. The following passages describe the developed procedure.

Registration by means of film perforation

For the registration of different acquisitions of a photographic film, it is necessary to select a set of *control points*; a control point has to belong to the original object, and it has to be possible to precisely locate it in the digital reproductions. The holes of the perforation constitute an optimal feature to be used in determining the control points, and, to this purpose, we always included the perforation in the acquisitions of the frames (in the *Academy ratio*, four holes on the left and four holes on the right). The procedure that follows provides a precise location of the centers of the holes; the procedure was found to be effective for the two most diffused types of perforation (*Bell & Howell* and *Kodak standard*) [78].

For each control point to be defined, an operator visualizes the digital image on screen and approximately indicates the center of the hole with a mouse click. At first, the algorithm performs the subsequent operations (Fig. 7.1.1):

- Selection of a adjacent rows of A pixels centered in the mouse click position
  - For all the A elements of the rows, computation of the average of the a values
- Selection of b adjacent columns of B pixels centered in the mouse click position

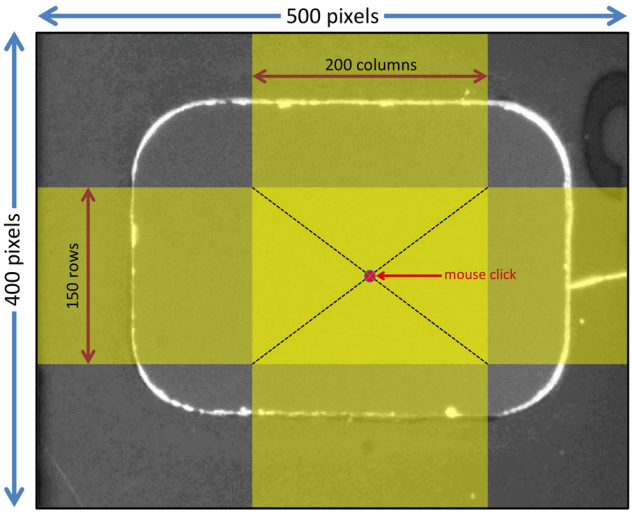

Figure 7.1.1: Procedure for the construction of the horizontal and vertical profiles of a perforation hole

– For all the B elements of the columns, computation of the average of the b values

Figure 7.1.1 describes the criteria that have to be adopted to determine a, A, b and B (these are resolution-dependent). A and B have to be large enough to completely frame the hole, including also a certain margin; a and b have to be large enough to provide sufficient smoothing that leaves out noise and disturbances, and at the same time, they have to be small enough to be included in the hole with a certain margin. The format of the hole in Figure 7.1.1 is *Kodak standard* and the image was acquired with $3200ppi$; proper values in pixels are $a = 150$, $A = 500$, $b = 200$ and $B = 400$.

The A average values of the rows and the B average values of the columns are arranged in two 1-dimensional arrays (*horizontal and vertical profile* respectively). The trend of the profile plots found in this way depends on the type of illumination used during the acquisition and on the characteristics of the film; the different trend plots that are found in different cases can be attributed to few typologies. The diagram in Figure 7.1.2 reports the most typical examples of profiles (the central column). Three elements can be distinguished in the profiles: the borders of the hole (I-borders), the film material around the hole (II-film) and the hole itself (III-hole); the typology of the profile is delineated by the values of these three elements. In the first case of Figure 7.1.2, the values of the hole and of the film are similar, and the borders soar over them as sharp peaks; the second case shows sharp border peaks, but in this case, the hole values are lower than the film values; in the third case, the peaks of the borders point downwards, and the hole has the highest values; also in the last case, the hole has high values, but in this case, the border peaks point upwards.

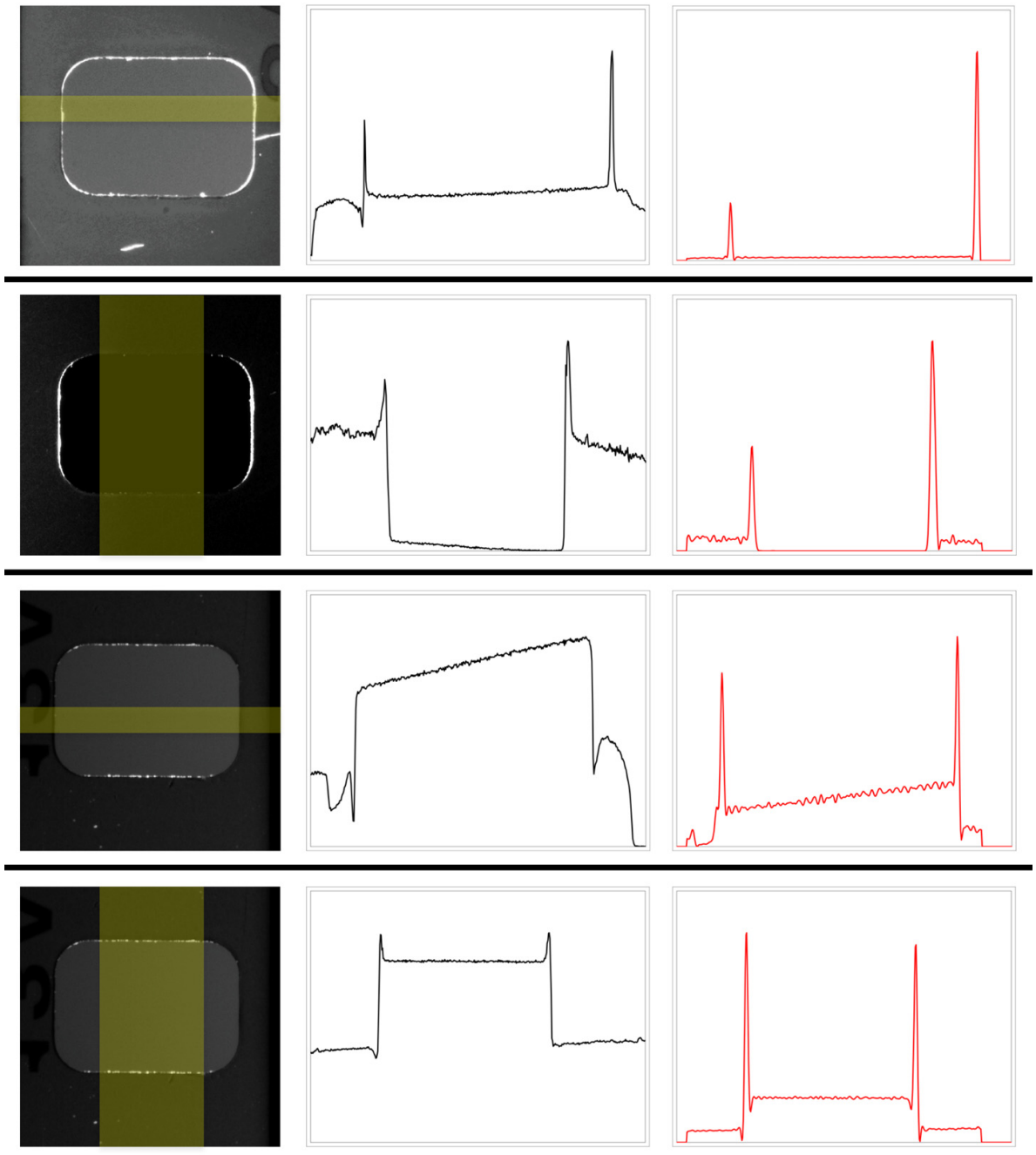

Figure 7.1.2: Different typologies of profiles: the image of the hole (left) with the selected rows/columns highlighted in yellow, the corresponding averaged profile (center) and the result of the application of Gabor filter (right)

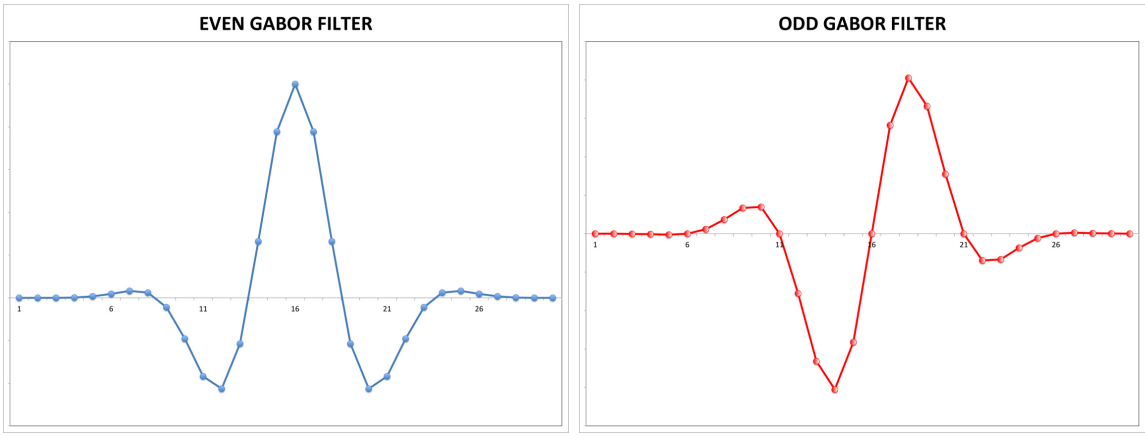

Figure 7.1.3: Impulse responses of even and odd Gabor filters

In order to automatically find the precise location of the borders (and, in turn, of the hole center), it is necessary to find a transformation that renders the different profile typologies into a unique typology: the application of a *Gabor filter* is effective for this purpose[1]. The impulse responses of the even and odd Gabor filters used are reported in Figure 7.1.3 ($wavelength = 10$ - $scale\,factor = 0.5$); the convolution of the profiles is executed with the even (G_{even}) and the odd (G_{odd}) filters and the filtered signals are combined by $G^2_{even}+G^2_{odd}$. The plots on the right of Figure 7.1.2 report the values of the profiles after the application of the Gabor filters; all the filtered profiles have a similar trend, in which the borders soar as sharp peaks over a relatively low base-line.

Generally, the base-line of the filtered profiles is found to be clean and homogeneous between the peaks and, on the other hand, disturbing elements may be found outside the peaks (Fig. 7.1.4). Actually, the flaws that can be present on the portion of film material around the hole are generally the cause of these disturbances; ordinarily, such flaws are never present in the empty inside of the hole; for this reason, it is convenient to carry out the identification of the peak locations by scanning the plot from the central point outwards, thus avoiding erroneous identifications due to flaws.

The procedure for the identification of the peak locations is described in Figure 7.1.4 for a profile composed by 500 values. Starting from the 250^{th} position of the filtered profile, the abscissa is scanned until the value of the current position becomes higher than a threshold: the threshold is defined as the mean value of the profile plus its variance ($\bar{x} + \sigma^2$). By proceeding outwards, another crossing with the threshold is found; the two crossings correspond to the two flanks of the most central peak, which is considered to be the border of the hole. The central point between the two crossings (which are found with sub-pixel accuracy) is selected as the exact position of the hole border. This procedure is executed leftwards

[1] As a matter of fact, the Gabor filter is particularly appropriate to describe the way in which the human visual system detects object edges [79]

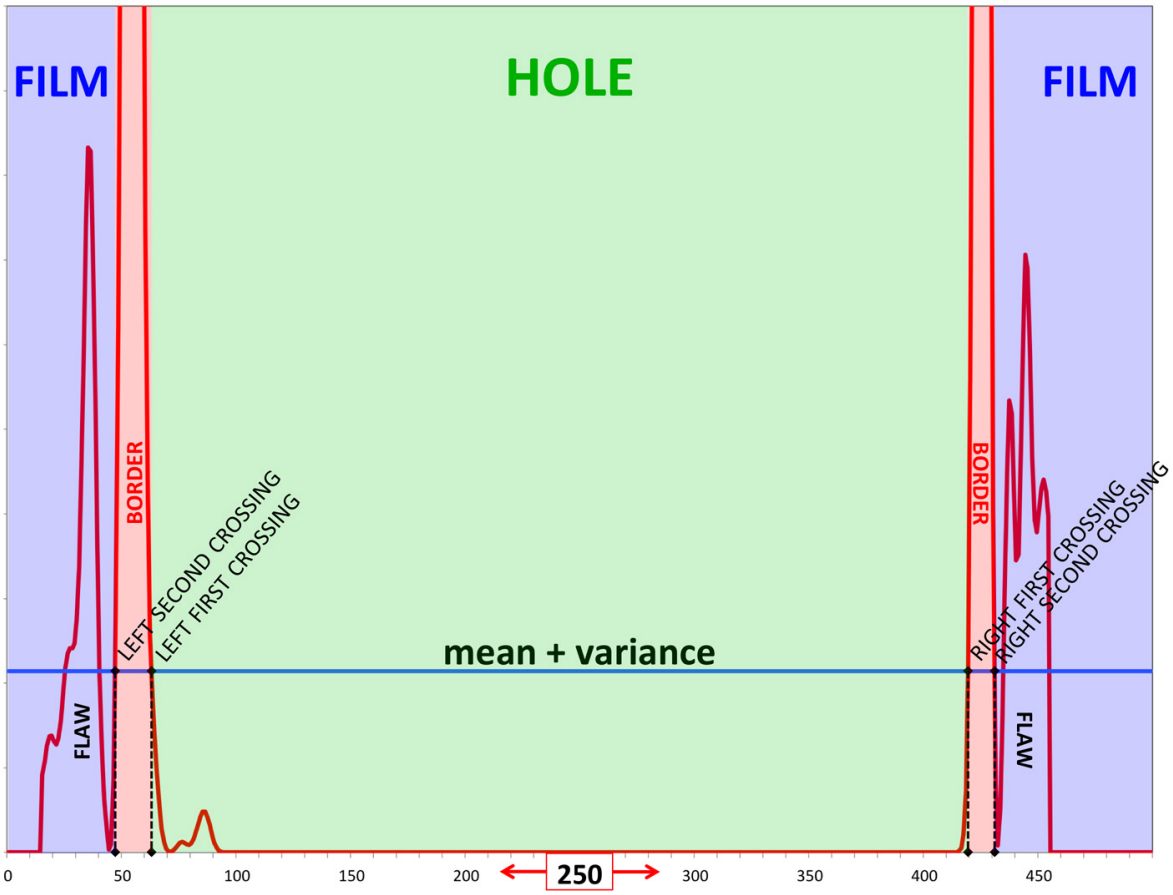

Figure 7.1.4: Procedure for the location of the borders of the hole

and rightwards on the vertical and on the horizontal filtered profiles, thus determining the positions of the top, bottom, left and right borders of the hole. The coordinates of the hole center are given, vertically and horizontally, by the central position between the borders.

The final transformation found is more accurate if the control points are far apart, and therefore, the above described computer-aided procedure that determines the control points is executed on the four holes at the corners of the image to be registered. The ground-truth's coordinate system was designated as the target system; the position of the control points of the misregistered image and the position of the ground-truth's control points (which were previously determined 'manually') provide the information necessary to calculate the suitable transformation, which matches the coordinate system of the misregistered images to the ground-truth's coordinate system.

Considering imaging systems with rectilinear objectives and free from any distortion, and considering that the film remains flat, a Projective transformation can correct all the misregistrations due to perspective irregularities that arise with the repositioning of the object or of the imaging system.

7.2 Software framework

A specific application (*Scratch And Flaws detectoR and ANalyzer*) has been created for this project to automate the creation of the detection-mask (following the precepts defined in Chapter 6) and to compute the evaluation of the detection. The software creates the detection-mask and a new image (the "*detection-result*"), which is indexed to have four possible values indicating the results of the comparison detection-mask/ground-truth. The detection-result, thanks to its clear and simple palette (Fig. 7.2.1), is a powerful tool to gain information on the strengths and the weaknesses of a certain detection method.

Two version of the software were realized: SAFRAN-v2 for the evaluation of flaw detection with a single image (sec. 6.1) and SAFRAN-v3 for the evaluation of the computational photography methods (sec. 6.2).

SAFRAN-v2 (Fig. 7.2.2) takes the prime-image and the corresponding ground-truth as inputs and then an iterative procedure allows for identifying the threshold value that optimizes the flaw detection (i.e. maximizes the MCC). Once this threshold value is identified, the software creates the detection-result image and computes all of the indicators, which are:

- n° of flaws - **f**
- n° of detections - **d**
- n° of successful detections - **SD**

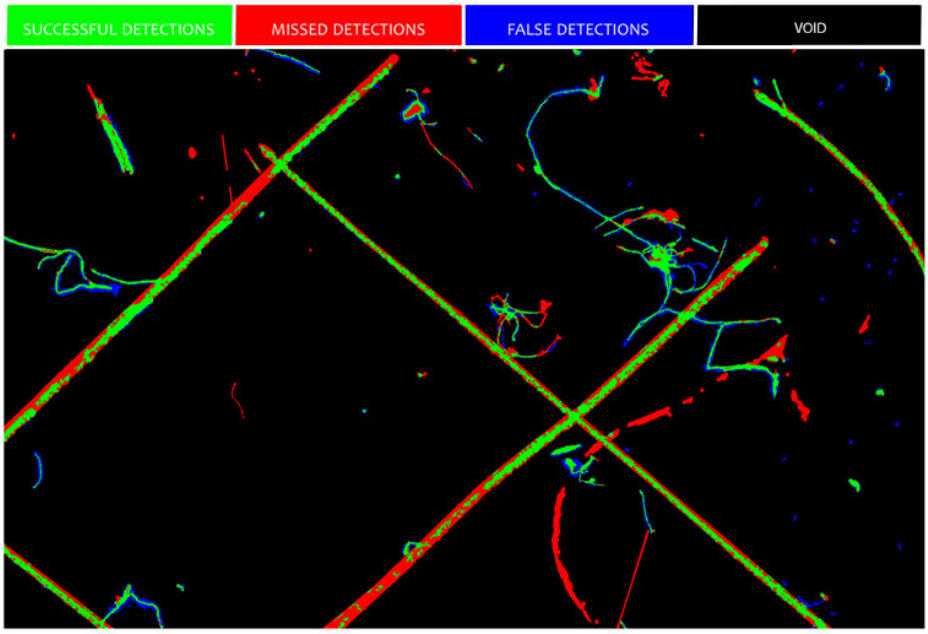

Figure 7.2.1: The result displayed by the SAFRAN software

- n° of missed detections - **MD**
- n° of false detections - **FD**
- % of defects correctly detected - **%SD/f**
- % of detections that are false - **%FD/d**
- Matthews Correlation Coefficient - **MCC**

After performing the Principal Components Analysis on the prime-images, SAFRAN-v3 (Fig. 7.2.3) takes the selected eigenimages ($EV2, ..., EVn$) and the corresponding ground-truth as inputs. The threshold-outside operation and the combination of the $n-1$ images produce a single binary image; this image undergoes the flaw-size thresholding operation, and this yields the detection-mask as a result.

As for SAFRAN-v2, the software creates the detection-result image and computes the numerical indicators.

Peak fraction for thresholding

By relying on the ground-truth, the iterative operation carried out by SAFRAN-v2 allows for finding the optimal threshold value for the specific prime-image used. In the operative

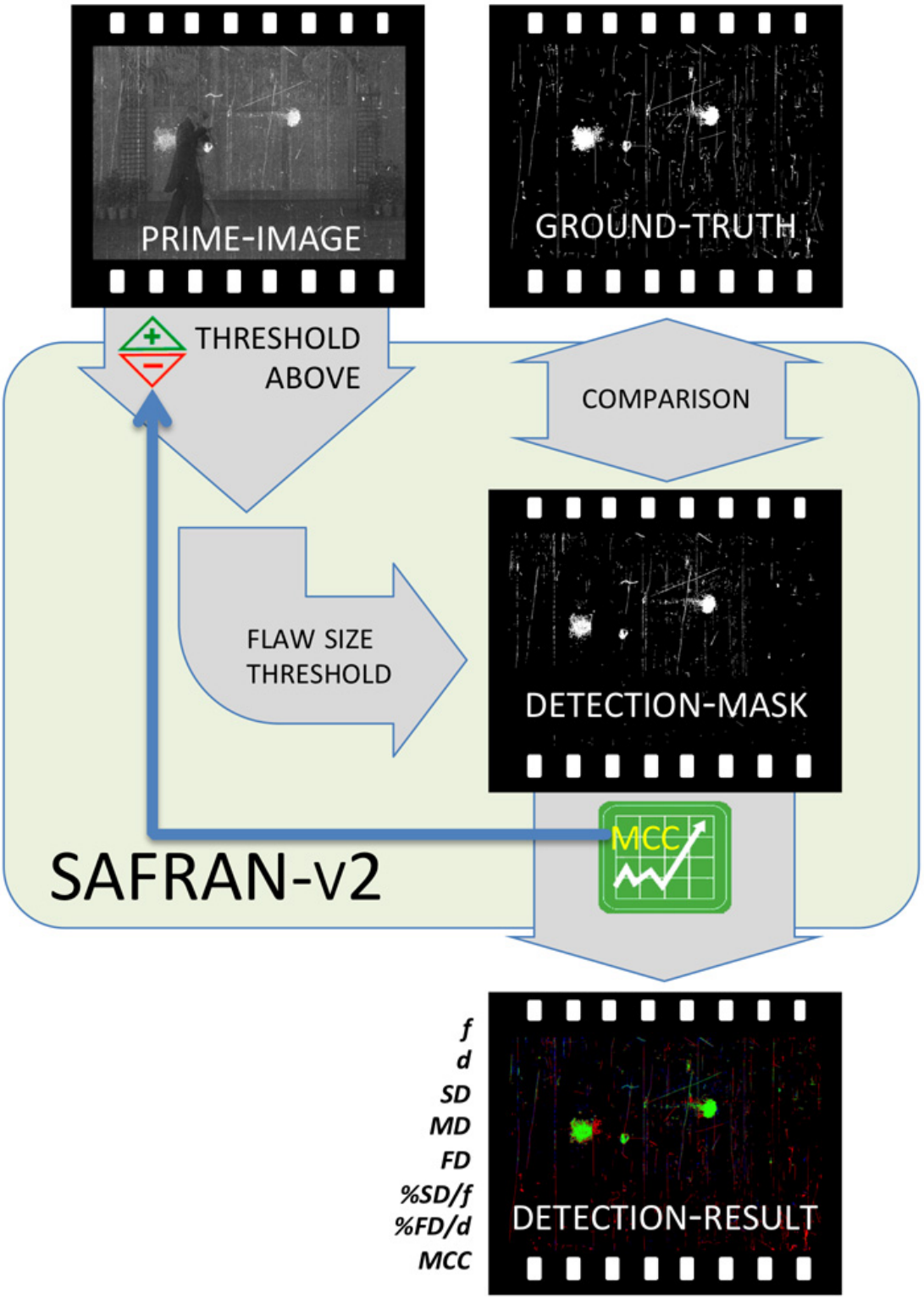

Figure 7.2.2: Flaw-chart of SAFRAN-v2

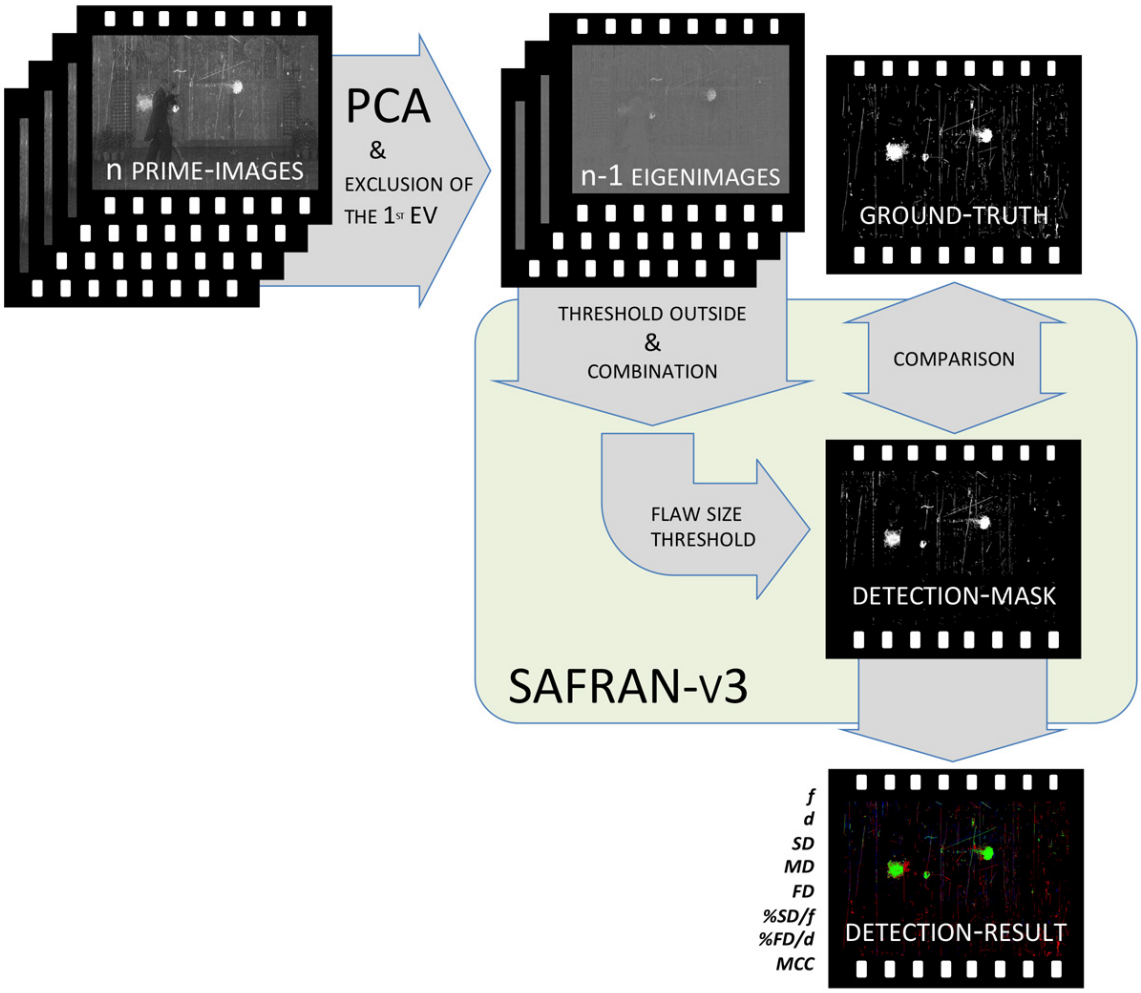

Figure 7.2.3: Flaw-chart of SAFRAN-v3

scenario of flaw detection, the ground-truth is obviously not available, and thus a suitable threshold value has to be identified by relying on the prime-image. To this end, the relation between the optimal threshold value found by SAFRAN-v2 and the histogram of the prime-image has been analyzed for a set of samples. The operations described in sections 6.1.2 and 6.2.5 rely on a predetermined fraction of the bin count of the peak in the histogram; the analysis drew the conclusion that $1/100$ is the proper fraction to have an optimal thresholding in the majority of cases.

Chapter 8

Identification of the best parameters

The present chapter reports the results of the experiments conducted to identify the best parameters to be adopted for every method proposed.

With the aim of having a broad variety of materials, a group of about one hundred photographic films of several different brands and with diverse film-speeds were collected for the experiments; all the samples chosen had mechanical local flaws present, such as dirt, dust and scratches. Some of the film were archival historical material of different provenances; the other part was constituted by films created on purpose, and these films were exposed with sinusoidal patterns, natural scenes or other test scenes and, after processing, artificially scratched and spread with dust on their wet surface (ensuring that the dust grains stick to the surface). For dye-based material, an effective method for flaw detection already exists (the use of infrared radiation); for this reason, the experiments were principally conducted on silver-based samples.

In accordance with the aim of the experiment, four different types of LEDs were used in the experiments as illuminating sources; their specifications are reported in Table 8.1. The polarization of light was obtained by using polyvinyl alcohol-iodine linear polarizers (*Polaroid HN38*).

The digital images were acquired with a DSLR camera equipped with a $12\,Mpixel$ CMOS full-frame sensor (*Nikon D3*). The reproduction ratio adopted was higher than $1:1$ and the

color	wavelength (nm)	FWHM (nm)	power (W)
white	broad spectrum	//	1
red	625	17	0.77
green	530	31	0.40
blue	470	29	0.95

Table 8.1: LEDs used in the experiments

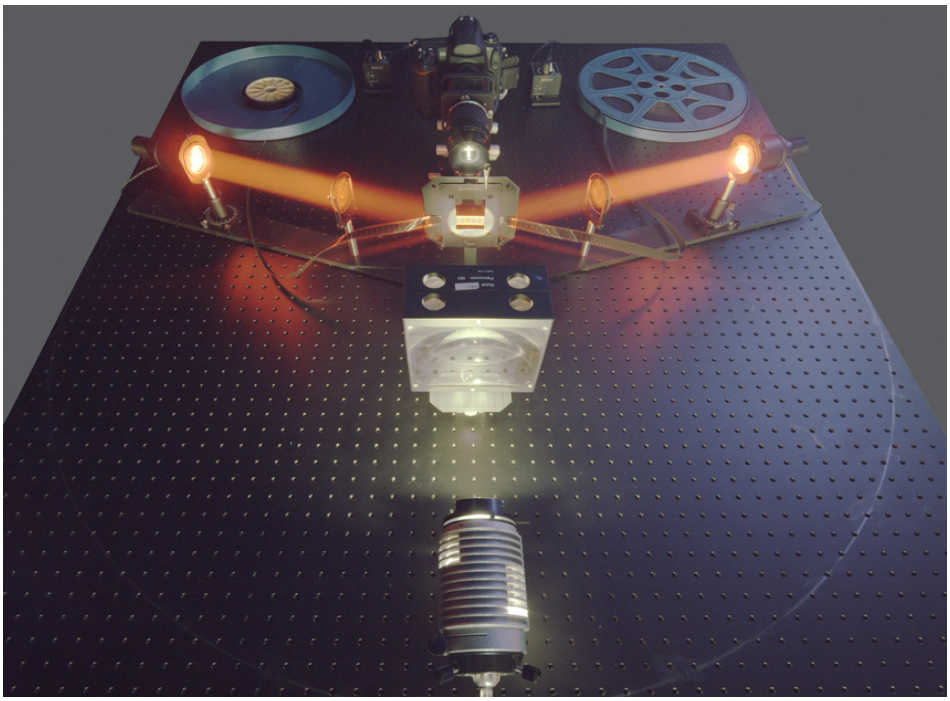

Figure 8.0.1: The main part of the laboratory

spatial sampling density was $3200ppi$; the image focusing was provided by a $105mm\ f/4.5$ objective mounted on a bellow. According to the light level, the exposure was adjusted in order to use the whole dynamic range of the sensor, while still avoiding saturation; moderate apertures, low ISO values and short exposures were preferred in order to prioritize better image quality. The images were saved by the camera in the proprietary RAW format using $14\,bits$; they were then externally converted in *TIFF/16bit* format using the *dcraw* software [80], choosing the parameters in order to linearly translate the raw data registered by the sensor.

Based on the LED used, the corresponding channel was selected accordingly: the R channel for the red LED, the G channel for the green LED, the B channel for the blue LED, and all the three channels for the white LED; in this last case, the three channels of the RGB image are merged into a monochromatic image.

The final images obtained in this way were the prime-images taken by the SAFRAN software as input for their elaboration and for the evaluation of the detection.

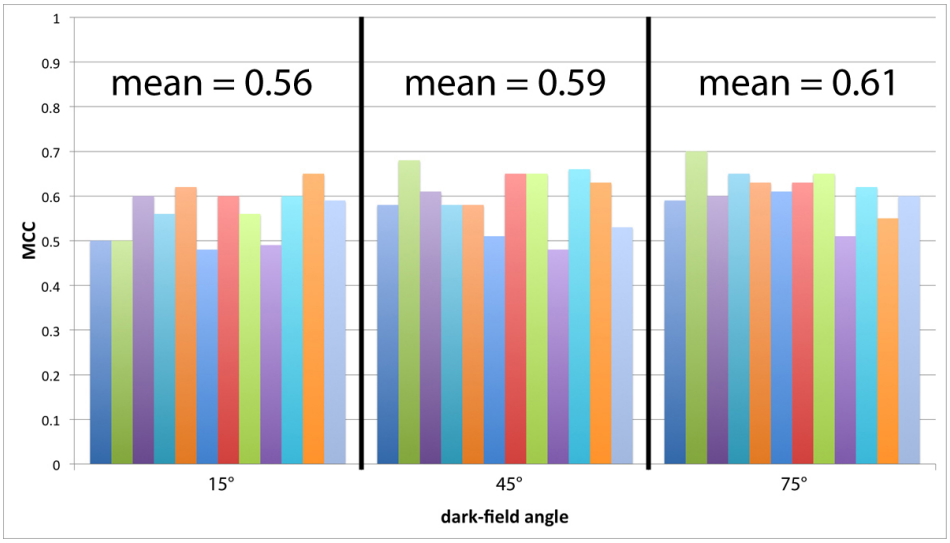

Figure 8.1.1: Polarized dark-field - mean MCC values of 12 samples for three different angles

8.1 Polarized dark-field - best parameters

In light of the treatise made in section 6.1.1, the polarized dark-field setup is the best optical setup to detect flaws by using a single image. The main parameters involved in the arrangement of a polarized dark-field setup are the following: the spectral emission of the sources, the angle between the beam of light and the optical axis, and the orientation of polarization (*S-polarized*, *P-polarized*). The influence of the parameters on the effectiveness of the flaw detection was studied; the results of this study are reported in the following sections.

8.1.1 Angle of light beam

An experiment was carried out to analyze how the angle between the light beam and the optical axis in a polarized dark-field setup influences the flaw detection performances.

A set of 12 processed silver-based photographic films affected by dust and scratches were selected; to provide more variety, the selected samples were chosen from diverse brands and with diverse sensibilities. Each of these was acquired three times in a polarized dark-field setup (as described in sec. 5.1.4) with a white LED, using different angles between the collimated light beam and the optical axis, namely $15°$, $45°$ and $75°$.

The images were analyzed with the SAFRAN software in order to provide the evaluation of the flaw detection. Figure 8.1.1 shows the histogram of the MCC values for the 12 samples and for the three different angles.

dark-field								
angle	10°	20°	30°	40°	50°	60°	70°	80°
MCC	0.18	0.09	0.05	0.04	0.04	0.05	0.06	0.19
polarized dark-field								
angle	10°	20°	30°	40°	50°	60°	70°	80°
MCC	0.48	0.48	0.50	0.49	0.50	0.51	0.56	0.61

Table 8.2: Angle experiment with dark-field and polarized dark-field setups

The smallest angle of 15° is large enough to prevent the directly transmitted light from entering the cone of acceptance of the optical system (i.e. proper dark-field), and thus a good flaw detection is obtained for all the images. By considering the mean MCC value of the 12 samples for each of the three different angles considered, we observe that this value decreases slightly when the angle decreases in size.

However, it has to be taken into consideration that as the angle increases in size, the light intensity collected by the camera decreases and, hence, the exposure time increases; when this method is applied to motion pictures, which have multitudinous frames that have to be processed, the time necessary to accomplish the entire procedure could increase excessively. Moreover, longer exposures entail a higher noise in the images.

8.1.2 Polarization

The experiment described here was carried out to demonstrate the following: the use of polarizers in a dark-field setup (as described in sec. 5.1.4) improves the result of the detection with respect to the simple dark-field setup (as described in sec. 5.1.3), and this is true regardless of the angle between the light beam and the optical axis.

A processed 35mm silver-based film with a speed of $100ASA$ was selected; the film was affected by linear scratches and large dust grains. A dark-field setup was arranged with a white LED and two acquisitions -with and without polarizers- were performed every 10° between 10° and 80° of the angle between the collimated light beam and the optical axis.

The images were analyzed with the SAFRAN software to evaluate the flaw detection; Table 8.2 reports the MCC values for the 8 different images in the two different setups.

With simple dark-field, the signal related to the emulsion remained high and the performances of flaw detection were relatively poor for all the angles. The polarized dark-field provided a stronger suppression of the emulsion signal for all angles, and the flaws were effectively detected (Fig. 8.1.2).

To provide more variety, the experiment was repeated for a specific angle for three other samples of diverse brands and film speed. The MCC values are reported in Table 8.3.

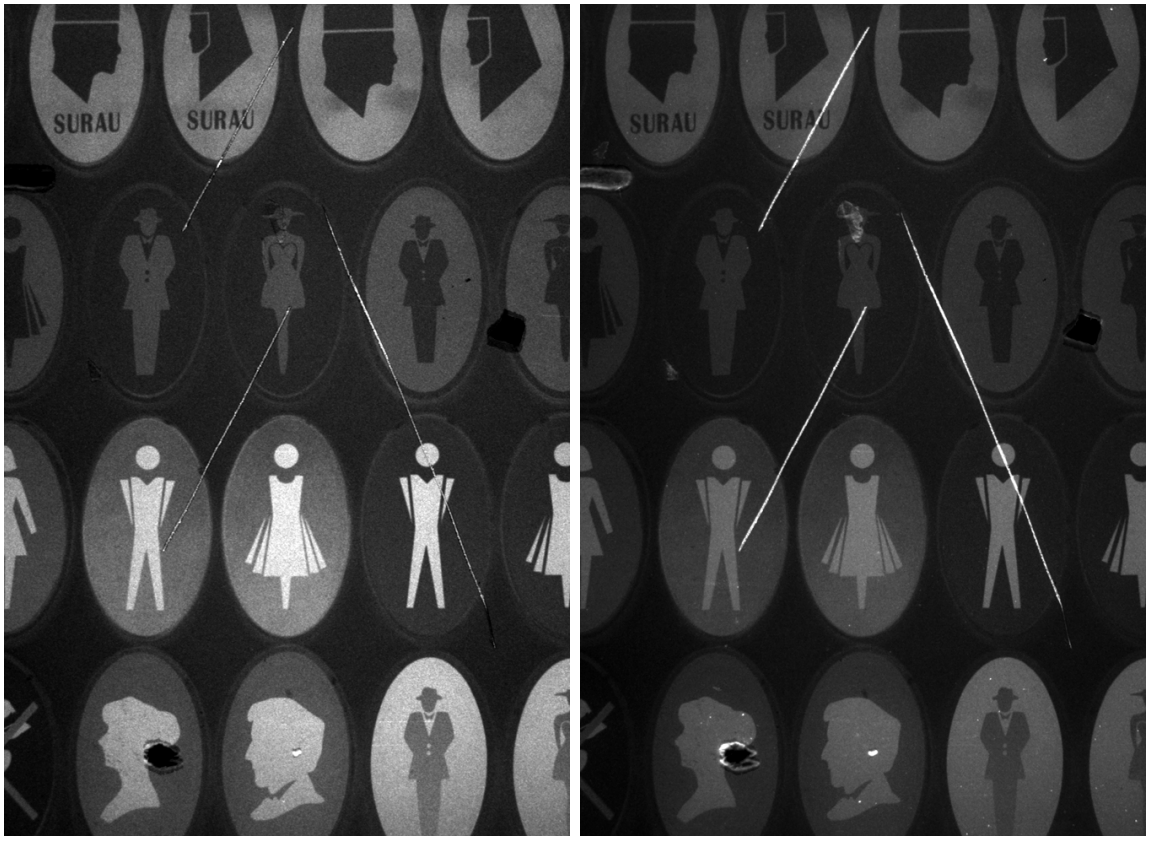

Figure 8.1.2: Images acquired with 50° angle in simple dark-field setup (left) and in polarized dark-field setup (right)

	sample 1	sample 2	sample 3
dark-field	0.3	0.55	0.38
polarized dark-field	0.44	0.57	0.53

Table 8.3: Additional samples for polarization experiment - MCC values

	red LED		green LED		blue LED	
	P-polar.	S-polar.	P-polar.	S-polar.	P-polar.	S-polar.
15°	0.60	0.55	0.57	0.55	0.60	0.60
45°	0.48	0.52	0.64	0.61	0.64	0.67
75°	0.51	0.51	0.56	0.62	0.66	0.63

Table 8.4: Polarized dark-field - MCC values for the polarization orientation experiment

In all the three cases, the polarized dark-field provides a better detection.

During the transit of linearly polarized light through the interface between two different media, the orientation of the polarization with respect to the interface plane may play an important role. In view of this, another parameter to be studied in defining an optical setup for flaw detection is the polarization orientation with respect to the film plane; specifically, we refer to P-polarization when at the point of incidence, the electric field oscillates parallel to the film plane, and we refer to S-polarization when the electric field oscillates perpendicularly.

A processed 35mm silver-based film with a speed of $3200ASA$ was selected; the sample was acquired in a P-polarized and a S-polarized dark-field setup using three different angles between the collimated light beam and the optical axis, namely $15°$, $45°$ and $75°$, and using three different types of sources, namely a red, a green and a blue LED. The images were analyzed with the SAFRAN software to provide the evaluation of the flaw detection; Table 8.4 reports the MCC values for the 18 different images.

The analysis of the values indicates that the orientation of the polarization with respect to the film plane does not have any significant influence on the performance of the flaw detection: there is no preferable orientation between P-polarization and S-polarization.

8.1.3 Spectral range

The experiment described here was carried out to analyze how the spectral distribution of the source in a polarized dark-field setup influences the performances of flaw detection.

Five different samples of diverse brands and film speeds were selected; these were all processed films affected by scratches and dust. A polarized dark-field setup was arranged and, for each sample, four different images were acquired with red, green, blue and white LEDs.

The values in Table 8.5 indicate that, on average, the best results are obtained with the green and the white LEDs.

Different reasons can be proposed to explain the poor results from the blue and the red LEDs. Figure 8.1.3 reports the transmittance of two polarizing filters that are used in a crossed position [81]; the optical density starts to fall off for shorter wavelengths, and at

	blue LED	green LED	red LED	white LED
sample 1	0.79	0.92	0.87	0.94
sample 2	0.61	0.62	0.45	0.61
sample 3	0.50	0.55	0.57	0.56
sample 4	0.65	0.67	0.63	0.67
sample 5	0.68	0.68	0.64	0.68
average	0.65	0.69	0.63	0.69

Table 8.5: Polarized dark-field - MCC values for the spectral range experiment

$450nm$, the transmittance is over 1%. For this reason, the experiments with the blue LED provide poorer results due to the weaker suppression of the emulsion image.

The green LED may be favored over the blue and the red LEDs because the corresponding selected channel (i.e. G-channel) has the double resolution of the other two; in fact, the CMOS sensor has a color filter arrangement which is 50% green, 25% red and 25% blue (*Bayer array*).

Moreover, according to the Airy theoretical treatment [82], the resolution depends on the wavelength of light; in fact, due to the diffraction at the aperture of an optical system, a point source is imaged on the sensor as a disc with a minimum radius given by

$$r_0 = 1.22 \cdot \lambda \cdot f\_number$$

For example, by considering a f_number of 8, the radius of the disc is $\backsimeq 4\mu$ for the shortest visible wavelengths (0.4μ) and $\backsimeq 7\mu$ for the longest visible wavelengths (0.7μ); in this second case, since one pixel of the sensor extends on a square of 8μ side, the disc is larger than one pixel, and the diffraction of light limits the resolution of the digital image. Hence, the resolution is lower with the red LED, and this may have a negative effect on flaw detection.

8.2 Direction-computational detection - best parameters

Flaw detection can be performed with a computational photography method based on a multiple image acquisition with n different directions of illumination (sec. 6.2.2). We studied the influence of the parameters involved in the efficacy of the direction-computational detection; namely, we focused on the influence of the polarization of light and the influence of the number of different directions adopted. The results of this study are reported in the following sections.

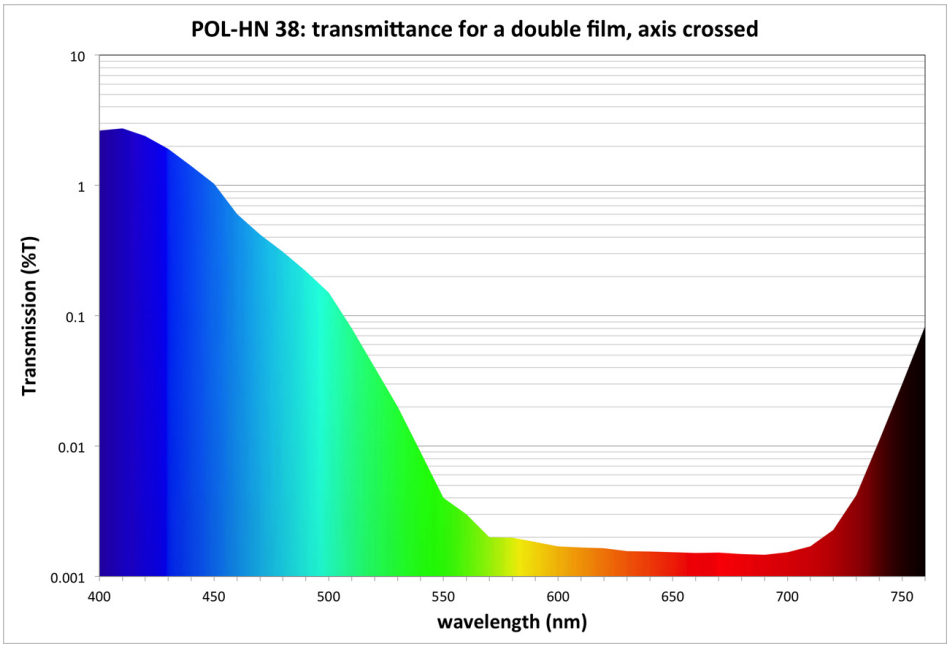

Figure 8.1.3: Transmittance of two polarizing filters placed in crossed position (log scale)

	dark-field (MCC)	polarized dark-field (MCC)
sample-1	0.57	0.60
sample-2	0.51	0.47
sample-3	0.67	0.69

Table 8.6: 4-DCP - polarization experiment

8.2.1 Polarization

First of all, it is fundamental to determine whether a simple dark-field is preferable or, on the contrary, if using polarizers in the dark-field acquisitions is convenient.

Three archival photographic films were selected; they were acquired four times with four different illumination directions (cardinal acquisition - sec. 6.2.2) provided by a white LED, and the entire procedure was carried out twice: once with polarizers and once without them. The detection-masks were then created with SAFRAN. The numerical evaluation of flaw detection is reported in Table 8.6.

The MCC values indicate that the use of polarizers does not provide a clearly better detection. It is certain that the polarized dark-field suppresses the emulsion image in the prime-images more than the simple dark-field; however, the subsequent computation provides a consistent suppression of the emulsion image in both cases, and the performances

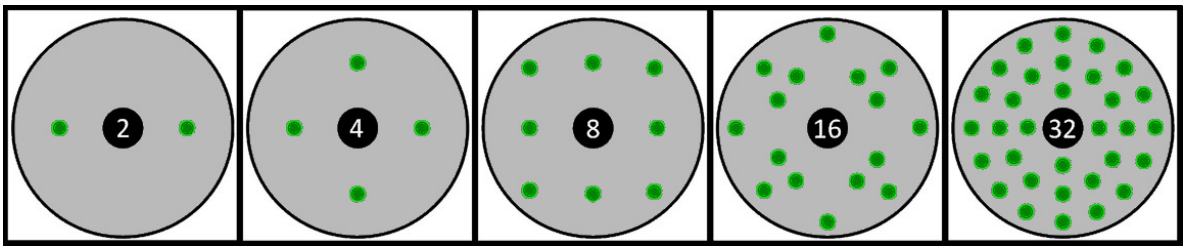

Figure 8.2.1: The six sub-sets of different positions of the source in plan view

of the flaw detection level off.

Moreover, it has to be taken into consideration that, in case polarizers are used, the light intensity collected by the camera decreases and, hence, the exposure time increases; when this method is applied to motion pictures, the time necessary to accomplish the entire procedure could increase excessively.

8.2.2 Number of directions of illumination

A specific experiment was carried out to determine which and how many different directions of illumination are needed for an effective flaw detection with the direction-computational method.

An archival photographic film was selected: a processed 35mm silver-based film on which dust, stains and scratches were present on both sides. Thirty-two different images were acquired using a white LED in dark-field setup, varying the θ and ϕ angles indicated in Figure 6.2.1. The thirty-two positions of the source were homogeneously distributed on the surface of a hemisphere opposite to the imaging device. The film and the camera were not moved between the acquisitions and, therefore, perfectly registered images were created.

Once the digital images were acquired, five sub-sets of the thirty-two images were chosen; these included 2, 4, 8, 16 and 32 different positions of the source. Figure 8.2.1 indicates the positions of the source in plan view for the five different subsets. The subsets were elaborated with the direction-computational method, namely, by extracting the differences between the images through PCA and by segmenting through a 'threshold outside'.

The numerical evaluation of flaw detection was provided by the SAFRAN software as described in Chapter 7. The results of the evaluation are reported in Table 8.7.

As indicated by the MCC values, the performances of detection are improved by increasing the number of images. This result confirms the model described in section 6.2.2 (Multi-direction acquisition).

Together with the increase in true positives (%SD/f), the number of false positives (%FD/d) also increases. However, after a careful examination of the color-coded images that express

	2 images	4 images	8 images	16 images	32 images
%FD/d	1.9%	3.8%	4.6%	6.7%	7.3%
%SD/f	44.9%	64.5%	70.8%	80.3%	88.3%
MCC	0.66	0.78	0.82	0.86	0.90

Table 8.7: Experiment for the determination of the number of directions

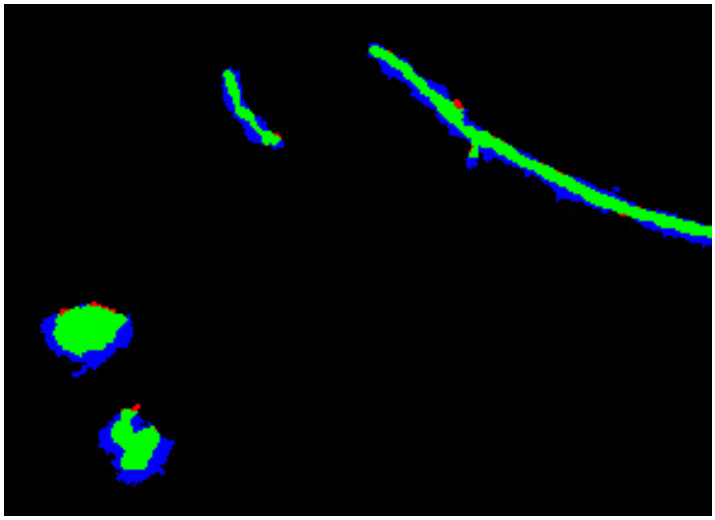

Figure 8.2.2: The result of flaw detection (color code: true positives - green, false negatives - red, false positives - blue)

the result of flaw detection, an important observation can be made. In many cases, the false positives are not separated from the real flaws (see Fig. 8.2.2); the shadowing effect due to the multiple oblique illuminations causes certain flaw elements to be detected as being larger than they really are [83]. For all of these flaws, an erosion of the detected elements would further improve the performance of the detection through post-processing.

The multi-directional illumination has proven to be effective; however, it is necessary to bear in mind that using a higher number of images entails greater complexity in the acquisition stage and also more onerous processing. Therefore, it is advisable to limit the number of images to a reasonable amount, according to an appropriate cost-benefit analysis.

Chapter 9

Method comparison

The present thesis defined in detail a group of innovative methods for optical flaw detection that are applicable on any type of photographic film (silver-based as well as dye-based material, still images as well as moving images). The present chapter reports the numerical evaluation of flaw detection provided by these methods and compares their performances. One of these methods was then selected for the subsequent comparison with the most effective traditional methods.

All the experiments were conducted on single photographs, while the comparison with the spatio-temporal image analysis had to be conducted on a frame sequence of a motion picture film.

9.1 Optical method comparison

In view of the experiments reported in Chapter 8, three optical methods for flaw detection are identified for silver-based material. The parameters of these methods were defined in Chapter 8; in the present chapter, their performaces are compared within each others.

A 35mm silver-based negative was exposed in front of a test scene. The scene was set so to obtain a processed film characterized by a variety of different features: high and low spatial frequencies, patterns and homogeneous areas, sharp and soft transitions, etc. Once the film has benn processed by means of its standard procedure, the selected frame was damaged with scratches and dust on both the emulsion and the support sides.

The flaws in the sample were detected with the following methods (all the images were acquired using a green LED):

- Polarized Dark-Field **(PDF)** - angle light beam / optical axis = 45°

PDF			CCD			4-DCD		
%FP/d	%TP/f	MCC	%FP/d	%TP/f	MCC	%FP/d	%TP/f	MCC
23.9%	60.1%	0.66	11.7%	64.4%	0.74	29.2%	77.5%	0.73

Table 9.1: Comparison of different methods

- Collimation-Computational Detection **(CCD)**
- Direction-Computational Detection **(4-DCD)** - cardinal fourfold acquisition in dark-field setup - angle light beam / optical axis = 45°

The flaw detection was quite successful for all of the three methods; considering the MCC values in Table 9.1, the collimation-computational method slightly exceeds the direction-computational method, and both computational methods are more effective than the single-image method. 4-DCD successfully detects a larger number of flaws but, at the same time, it erroneously marks a large number of sane pixels as "flawed"; as it was already explained in the end of the previous chapter, these false detections often correspond to real flaws that, due to shadowing effects, are detected as being larger than they really are (Fig. 8.2.2).

9.2 Traditional methods vs. direction-computational detection (8-DCD)

In view of the experiments conducted and in view of our reflections on the state-of-the-art of digital restoration, we consider the direction-computational detection the most innovative and promising technique between those presented in the previous section. For this reason, we considered important to carry out a numerical comparison between the performances of the direction-computational detection and the most effective and diffused traditional methods: Digital ICE and spatio-temporal image analysis (sec. 3.2). For the experiments that follow an eightfold acquisition is adopted for the direction-computational detection (Fig. 9.2.1).

9.2.1 Digital ICE vs. 8-DCD

The comparison between Digital ICE and direction-computational photography (8-DCD) was conducted on three processed dye-based negatives affected by dust and scratches; to provide more variety, the selected samples were chosen from diverse brands and with diverse sensibilities.

Images of the samples were acquired with $3200ppi$ using a flatbed scanner (Epson Perfection V700), equipped with the Digital ICE technology.

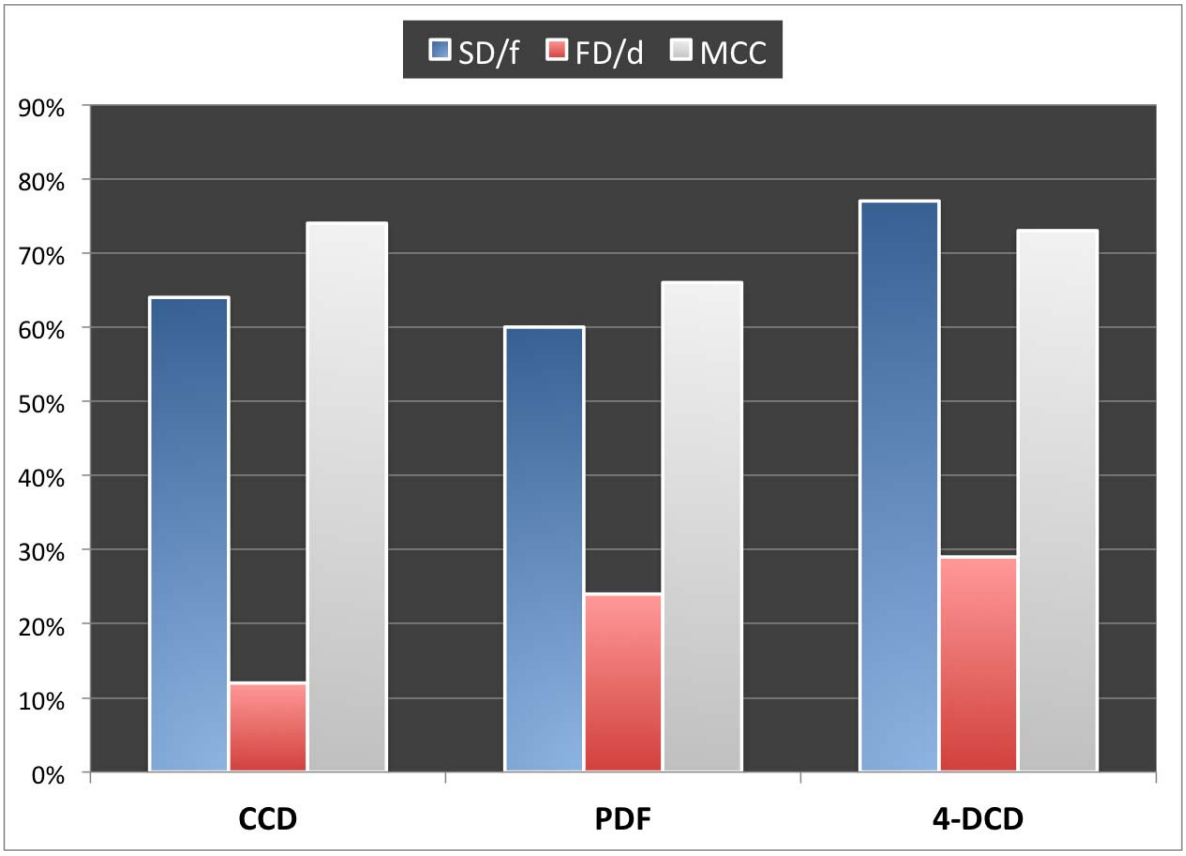

Figure 9.1.1: Comparison of different methods - histogram

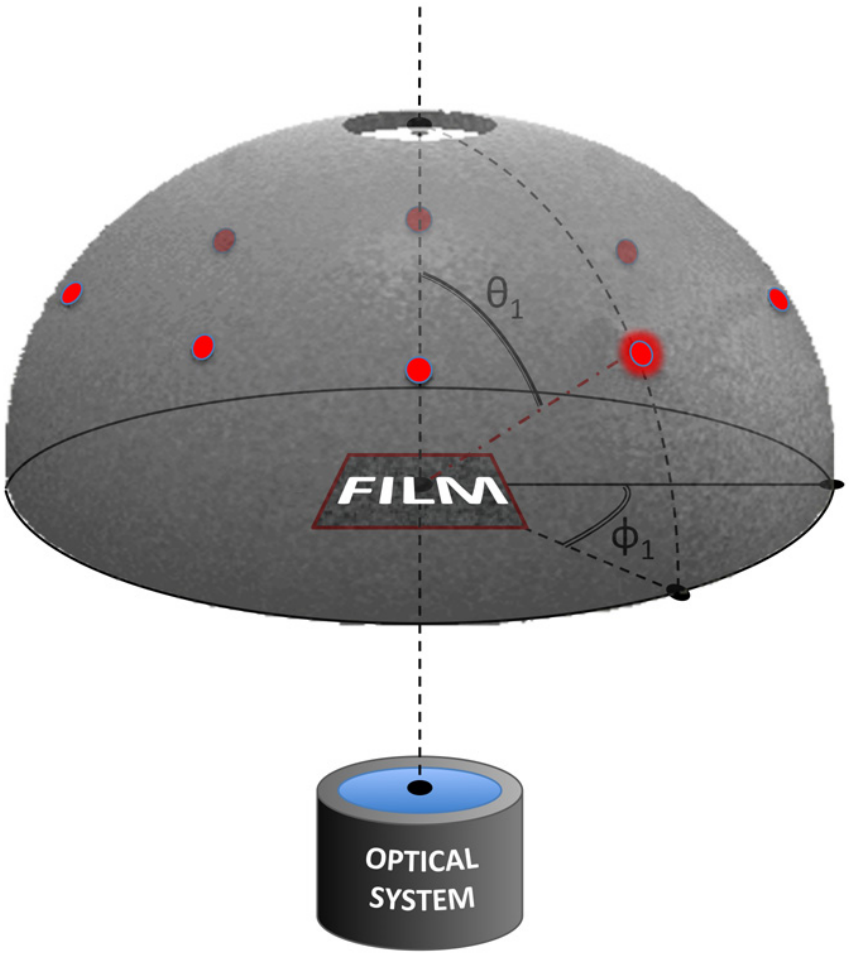

Figure 9.2.1: The eightfold acquisition setup: the red dots indicate the positions of the sources

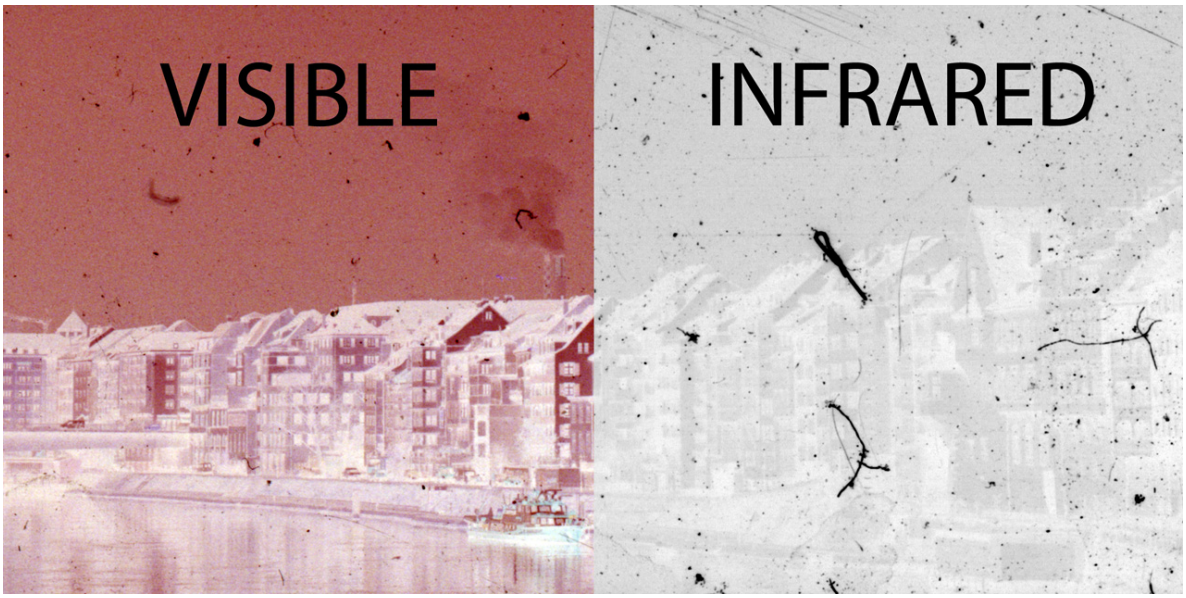

Figure 9.2.2: The image of a dye-based film acquired by the scanner: the left part displays in color the visible channels and the right part reports the infrared channel

In the infrared images, the emulsion is considerably suppressed and the flaws appear as definite dark marks (Fig. 9.2.2); however, in the spectral range of the infrared channel the dyes are not completely transparent and the photographic image is still visible.

In Figure 9.2.3 the results of flaw detection are reported for Digital ICE and for 8-DCD. The points in which Digital ICE indicates a flaw are marked in green, while the points in which 8-DCD indicates a flaw are marked in red; in the points marked in blue both the methods indicated a flaw.

As a general rule, the Digital ICE produces good results, exploiting the best performances in case of dust grains. On the other hand, in correspondance to scratches, the attenuance of infrared radiation is only due to scattering (scratches generally do not entail strong absorption), and thus the traces of scratches are often not very definite; in such cases, missed detections may occur.

In case the scratch is very deep, missed detection are even more likely; Figure 9.2.4 reports one of these examples. The emulsion has been removed and the absorption of both visible and infrared radiations is strongly reduced; as a consequence, in the image acquired in a bright-field setup (left) the penetrating scratch glows, while the Digital ICE technique (center) does not perceive the scratch as a definite mark. On the other hand, the direction-computational method (right) correctly detects the deep scratches.

However, it is also important to notice that, in case of very superficial scratches, under which the emulsion is still visible and the proper fruition of the image is not compromised,

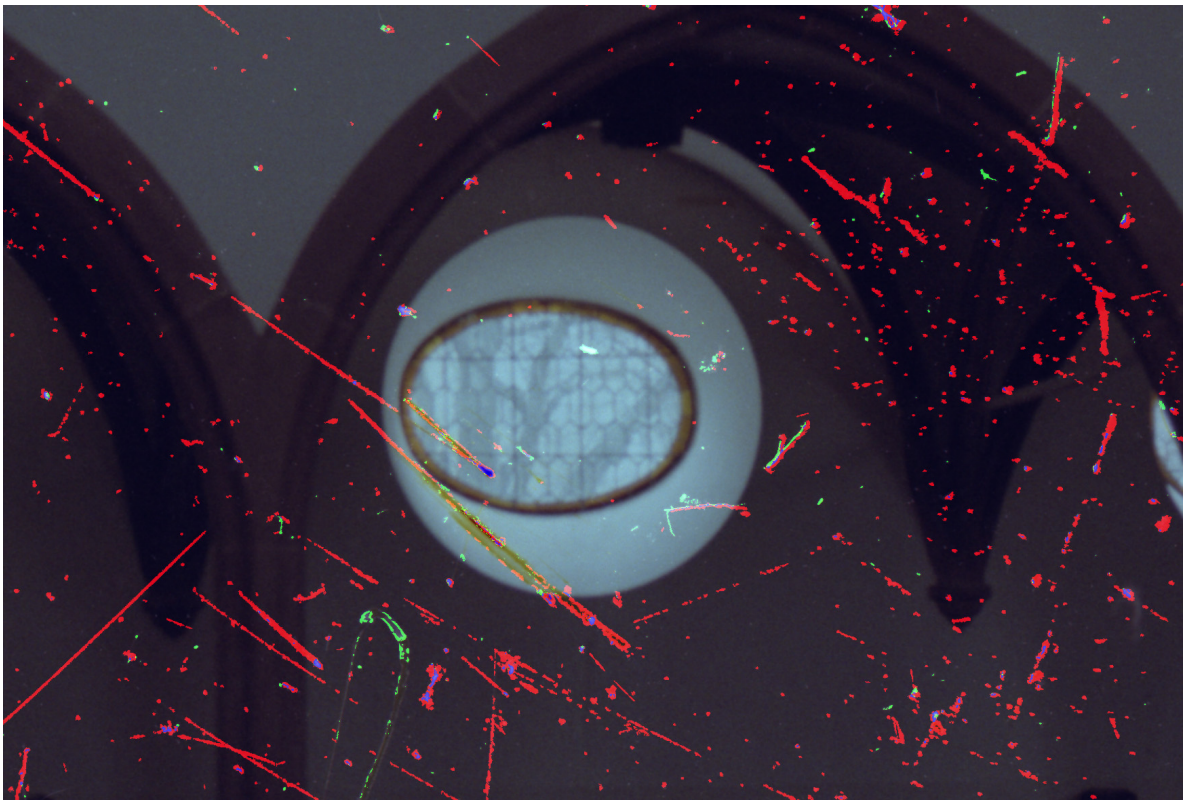

Figure 9.2.3: Flaw detection with Digital ICE (highlighted in green) and with 8-DCD (highlighted in red); the points where both the methods detected flaws are marked in blue

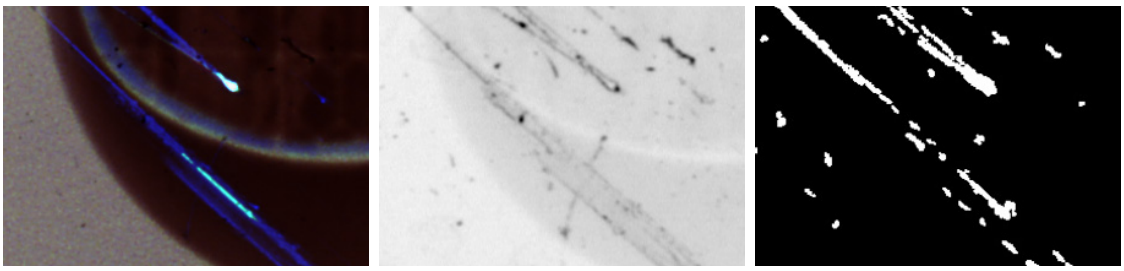

Figure 9.2.4: A penetrating scratch in bright-field (left) in the IR channel (center) and as detected with the multi-directional method (right)

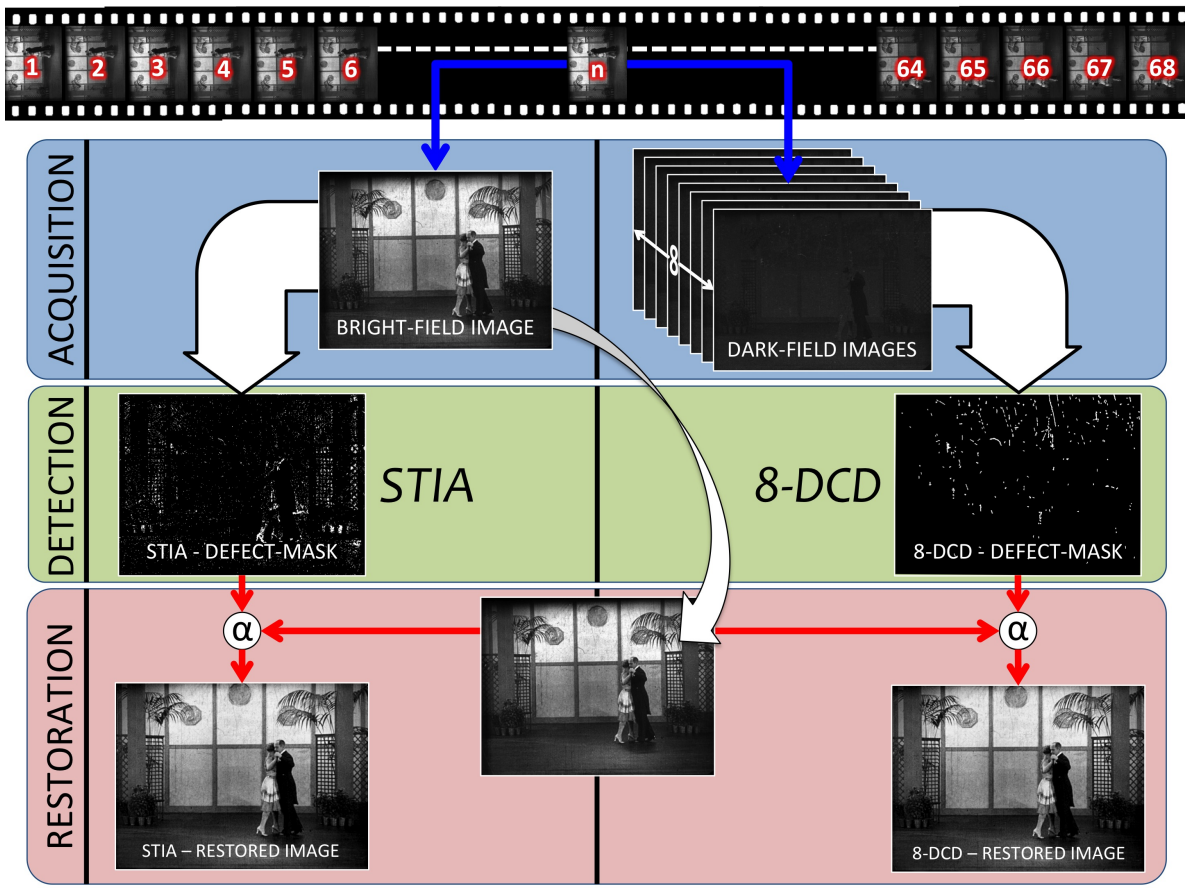

Figure 9.2.5: Comparison between spatio-temporal image analysis (STIA) and direction-computational detection (8-DCD)

the direction-computational method is sometimes too sensitive and it over-detects.

9.2.2 Spatio-temporal image analysis (STIA) vs. 8-DCD

The comparison between direction-computational detection (8-DCD) and spatio-temporal image analysis (STIA) was conducted on a motion picture print film (Fig. 9.2.5); the sample selected is a 35mm silver-based film produced by the German company '*Lignose*' (mainly operative during the 20s) [84], which was operated at 24 frames-per-second. Sixty-eight consecutive frames ($\backsimeq 2.8$ seconds) of a static shot were considered in the experiment; the scene framed was an interior in which two characters perform a dance movement. The frames were severely affected by dust and scratches.

The dark-field setup for the direction-computational detection is depicted in Figure 9.2.1: an eightfold acquisition was performed with polar angle $\theta = 45°$ at azimuths $\phi = 0°, 45°,$

$90°$, $135°$, $180°$, $225°$, $270°$, $315°$. The flow-chart in Figure 9.2.5 describes the process. Nine images were acquired for each of the sixty-eight frames: eight dark-field images and a reproduction in diffused bright-field. The flaws were detected with the spatio-temporal image analysis (sec. 3.2) using the bright-field images, and with the direction-computational method (sec. 6.2.2) using the dark-field images. The two detection masks produced with the different methods were included in the alpha channel of the bright-field image; this information provided a 'guidance' for the subsequent inpainting stage.

Image stability is fundamental for an effective spatio-temporal image analysis [40]; therefore, prior to detection and reconstruction, the motion created by the images of the sixty-eight frames was stabilized referring to the static interior present in the scene. The bright-field sequence was used for the stabilization; the transformation found for each frame was applied equally to the eight dark-field images, and finally, all the nine images of each frame were registered and the image sequence was stable. *Flicker*, as well as image vibration, may also jeopardize the spatio-temporal image analysis; hence, a de-flicker was also applied to the sequence.

Image stabilization, de-flicker, spatio-temporal image analysis and inpainting were performed using the software *NUKE* and its plugin *FURNACE*, distributed by the company *The Foundry Visionmongers Ltd*. Its tool *F_DirtRemoval* automatically detects and removes specs of dust and dirt from a frame, looking for objects that appear for only one frame (STIA). The tool can take as input a previously created detection-mask; if this input is supplied (as a separate file or in the alpha channel), the restoration takes place only in the regions specified in the mask; we used this feature to perform the inpainting that relies on the 8-DCD. The parameters of the spatio-temporal detection can be adjusted according to presets; for archive footage, the FURNACE's user guide suggests the '*Very Aggressive*' preset and, in accordance with this suggestion, we chose this preset for the restoration through STIA.

In light of an accurate examination of the detection accomplished by the two methods, and by carefully analyzing the corresponding restored versions of the short sequence, some important observations that can be made. In the following figures, significant details of specific frames are reported, displaying the original and the restored versions, and highlighting in red the pixels considered as flaws by the two methods.

By watching the restored movies, one of the first impression is that the STIA version is cleaner then the 8-DCD version. As a matter of fact, STIA is favored whenever the flaws have been copied (Fig. 9.2.6); in these cases, on the other hand, every optical method is deceived.

By looking the film with a microscope, allowed verifying that many of the black spots on the film, rather than being real dust grains, were just traces of dust grains that were accidentally lying on the film during previous copying operations (Fig. 9.2.7).

Motion of objects in the scene is a problem for STIA. If an element of the scene is moving fast, its position changes considerably between adjacent frames and, in these cases, the

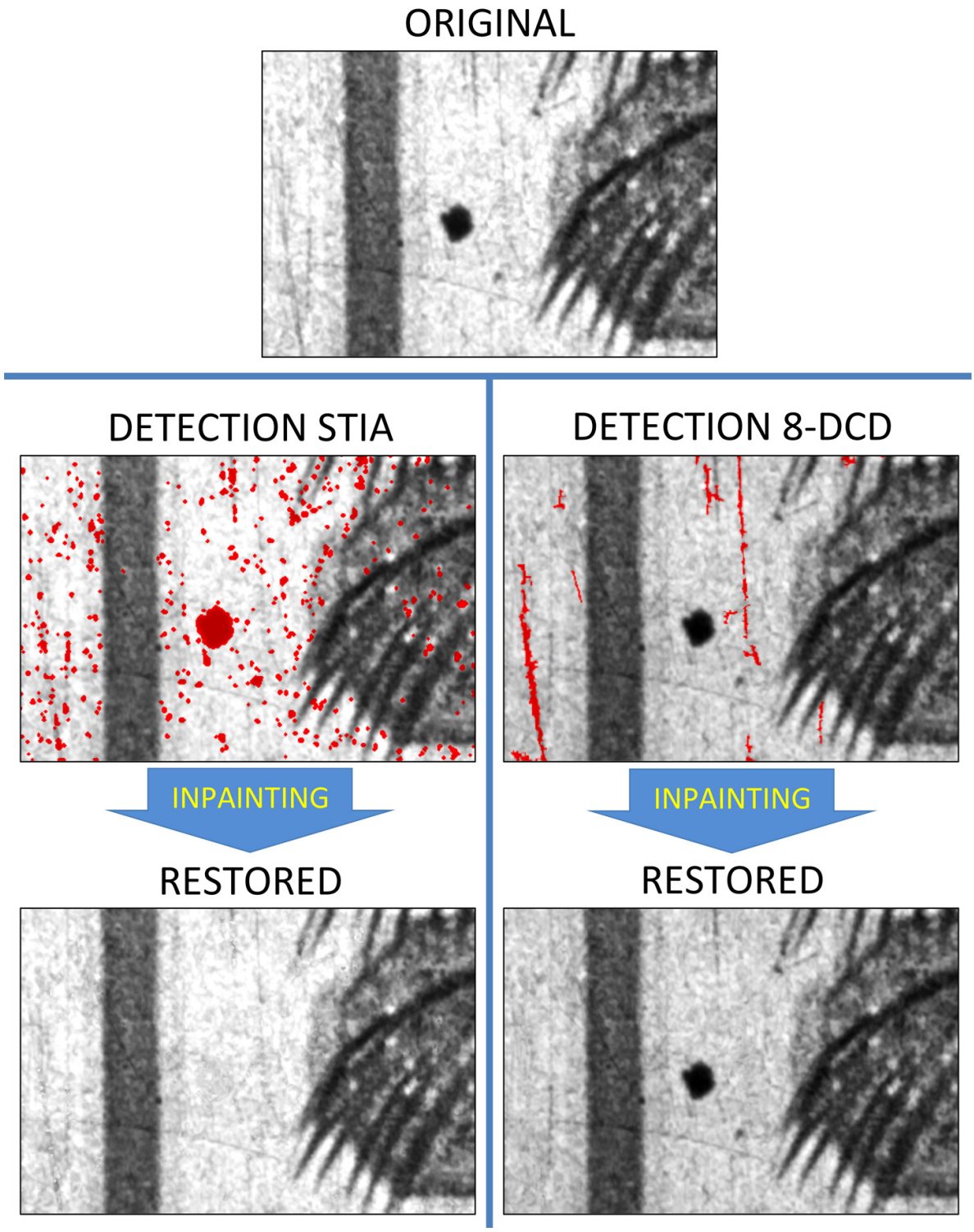

Figure 9.2.6: Comparison between STIA and 8-DCD - the case of copied flaws

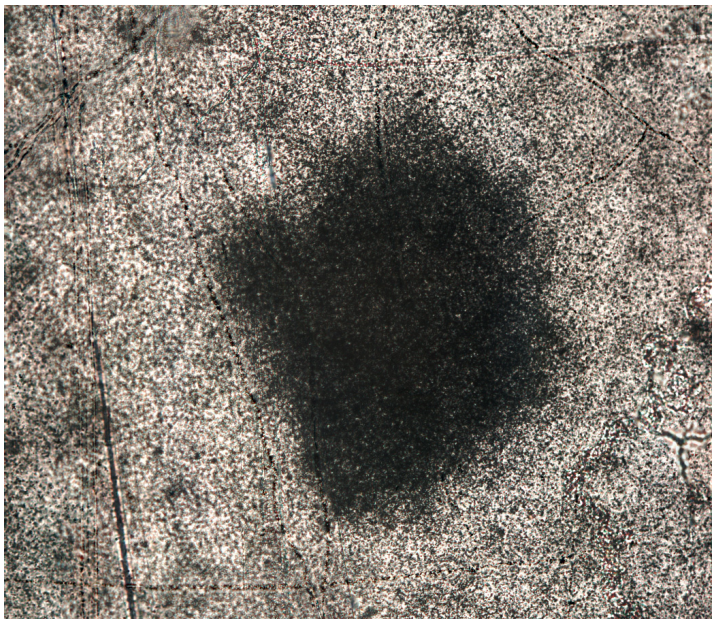

Figure 9.2.7: Microscopic image of the dust grain trace of Fig. 9.2.6

software does not find the correlation for the corresponding part of the film; as a result, the software erroneously considers the fast element as a flaw. In order to avoid this problem, the tool *F_DirtRemoval* is able to grasp the motion in the image sequence and to compensate the it in order to find the correlation. However, the compensation can be accomplished only in the case of simple motion (e.g. uniform linear motion); in the case of several elements moving in different directions, the compensation is impossible. The dance movement of the motion picture under consideration was a too complex motion to be compensated, and the tool intervened erroneously and produced artifacts. The detail of Figure 9.2.8 presents artifacts in the version restored with STIA; in fact, the shoes of the dancers are moving quite fast in a complex manner.

The random movement of the film grain was also erroneously detected by STIA; in fact, the grain is changing its position from frame to frame, and actually, STIA often considered it as a flaw. A careful analysis of the restored images shows that STIA washed out the grain; in this respect, it is important to point out that, by adopting a higher resolution during the image acquisition, the erroneous detection of film grain is even more problematic; in fact, with a higher resolution the grain moves by a larger number of pixels, and the correlation between adjacent frames is more compromized.

The spatio-temporal image analysis is completely effective only on quite homogeneous areas and often fails in correspondence to borders with high contrast; the dust grain at the summit of the woman's head in Figure 9.2.9 is an example of flaw unlikely detectable by STIA.

In correspondence to a region characterized by a high optical density, the direction-computational

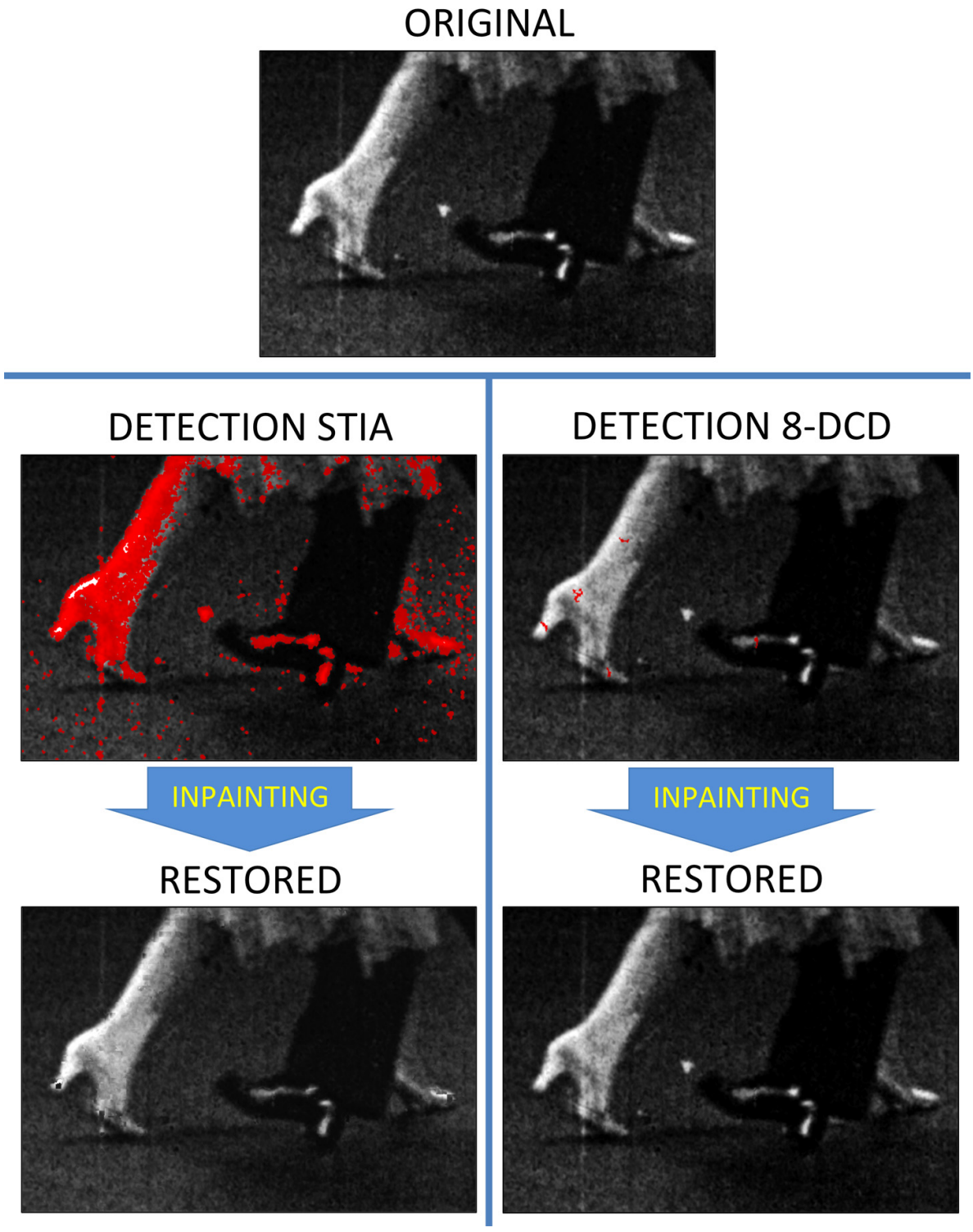

Figure 9.2.8: Comparison between STIA and 8-DCD - the case of fast elements

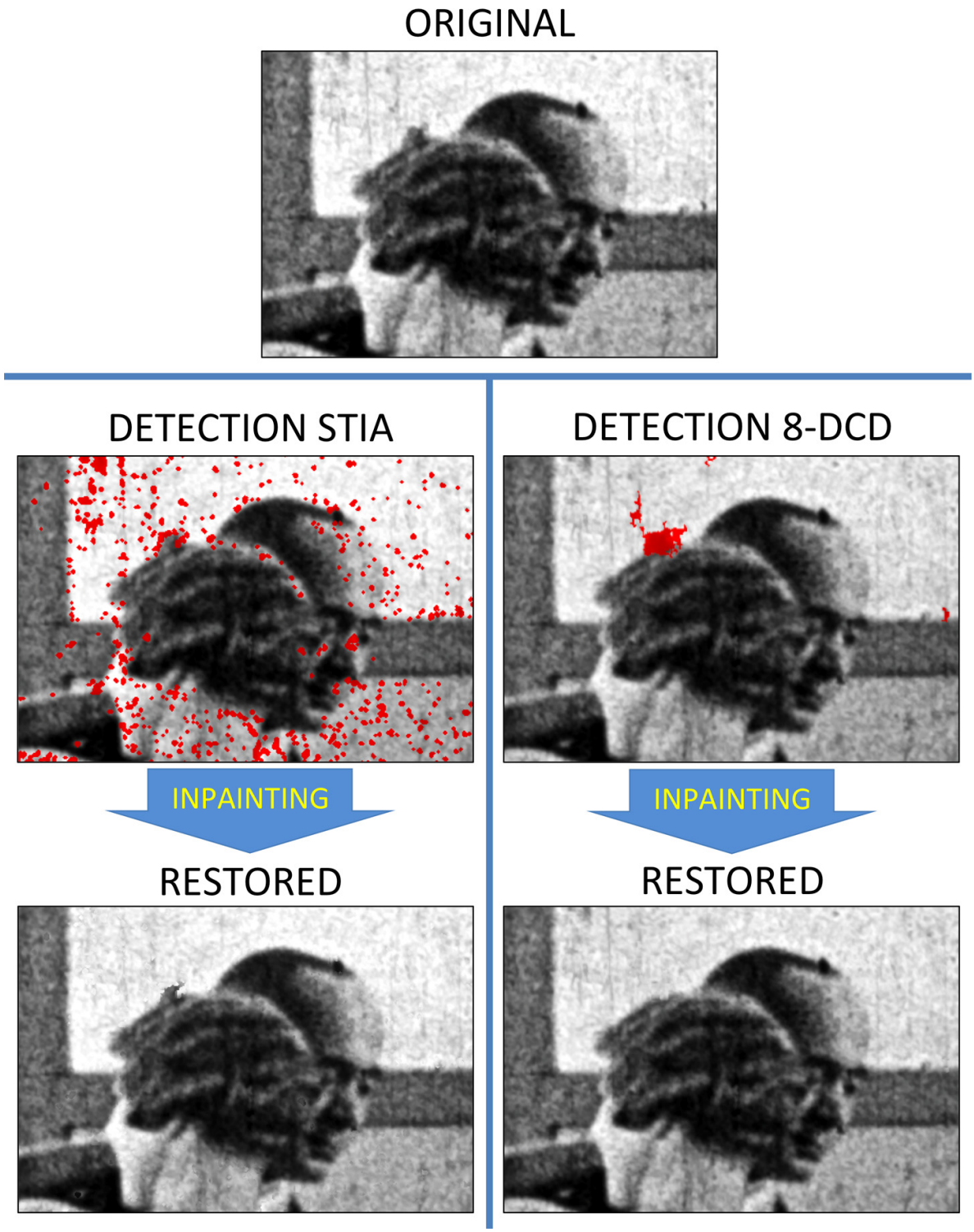

Figure 9.2.9: Comparison between STIA and 8-DCD - the case of high contrast borders

detection may be prevented due to the covering effect of the absorbing silver layer. This is the case of Figure 9.2.10, in which the vertical scratch is positively detected by the 8-DCD in the bright region, but it is left untouched in correspondence to the dark circular shape. However, this could be considered positive, as a non-penetrating scratch is less visible in a dark background.

A typical flaw of archival material are the vertical scratches due to the transportation of the film in the camera or in projectors; they are often long and appear in the same place in multiple frames. In this cases STIA is deceived, while 8-DCD works effectively (Fig. 9.2.11).

Pros and cons are found for both methods. With the 8-DCD method the false detections are almost completely avoided.

The restoration of an archival film must distort as least as possible the images of the motion picture [35]; it is opportune to alter the original information only in case the degradation compromises the proper fruition of a film. The inpainting operation seeks for pleasing and visually plausible interventions; nevertheless, it introduces arbitrary information. In this respect, missed detections is the lesser evil and they have to be preferred to false detections; the experiments presented in this chapter showed that the direction-computational detection, in spite of some missed detections, entails a lot less false detections than the spatio-temporal image analysis.

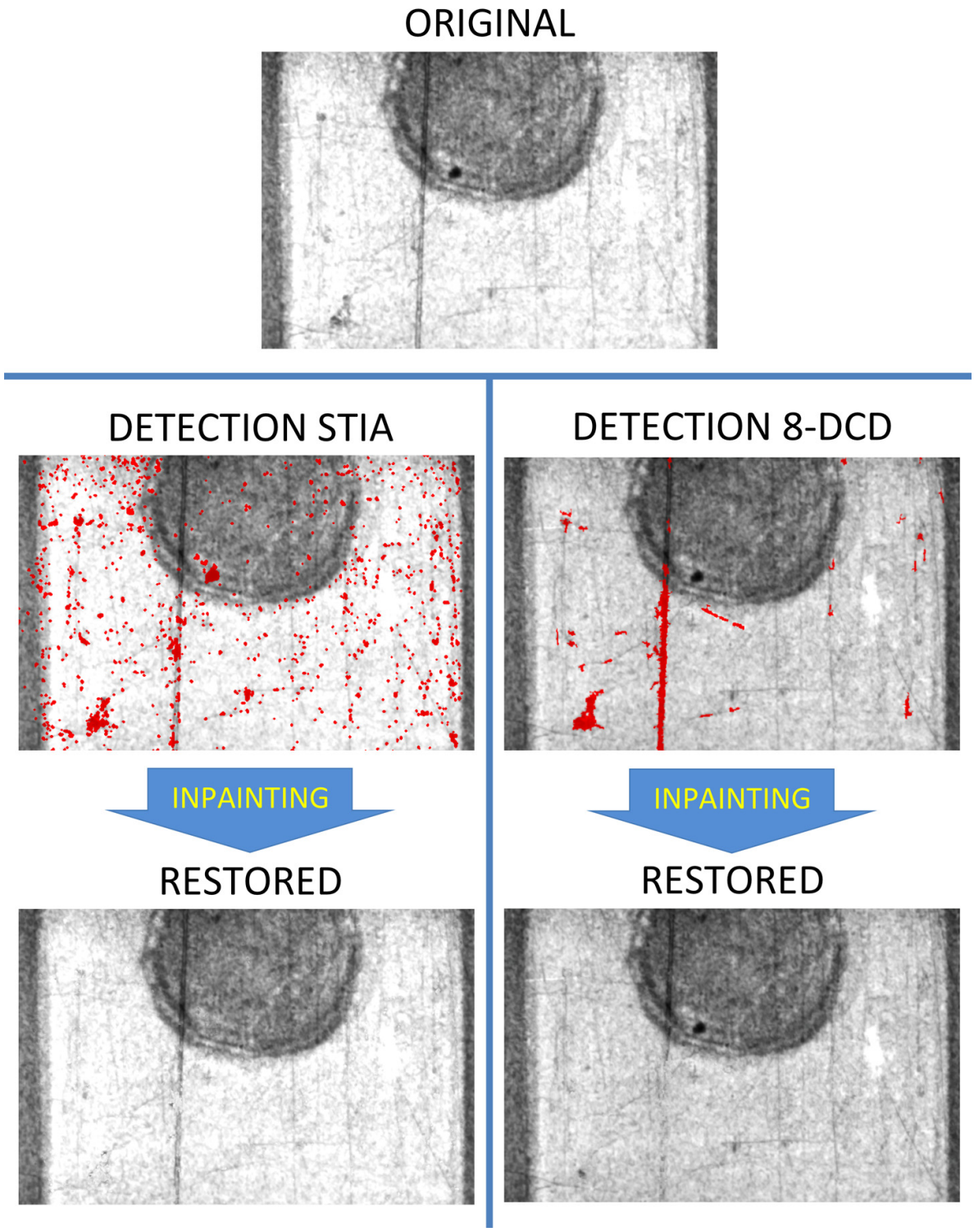

Figure 9.2.10: Comparison between STIA and 8-DCD - the case of the covering effect

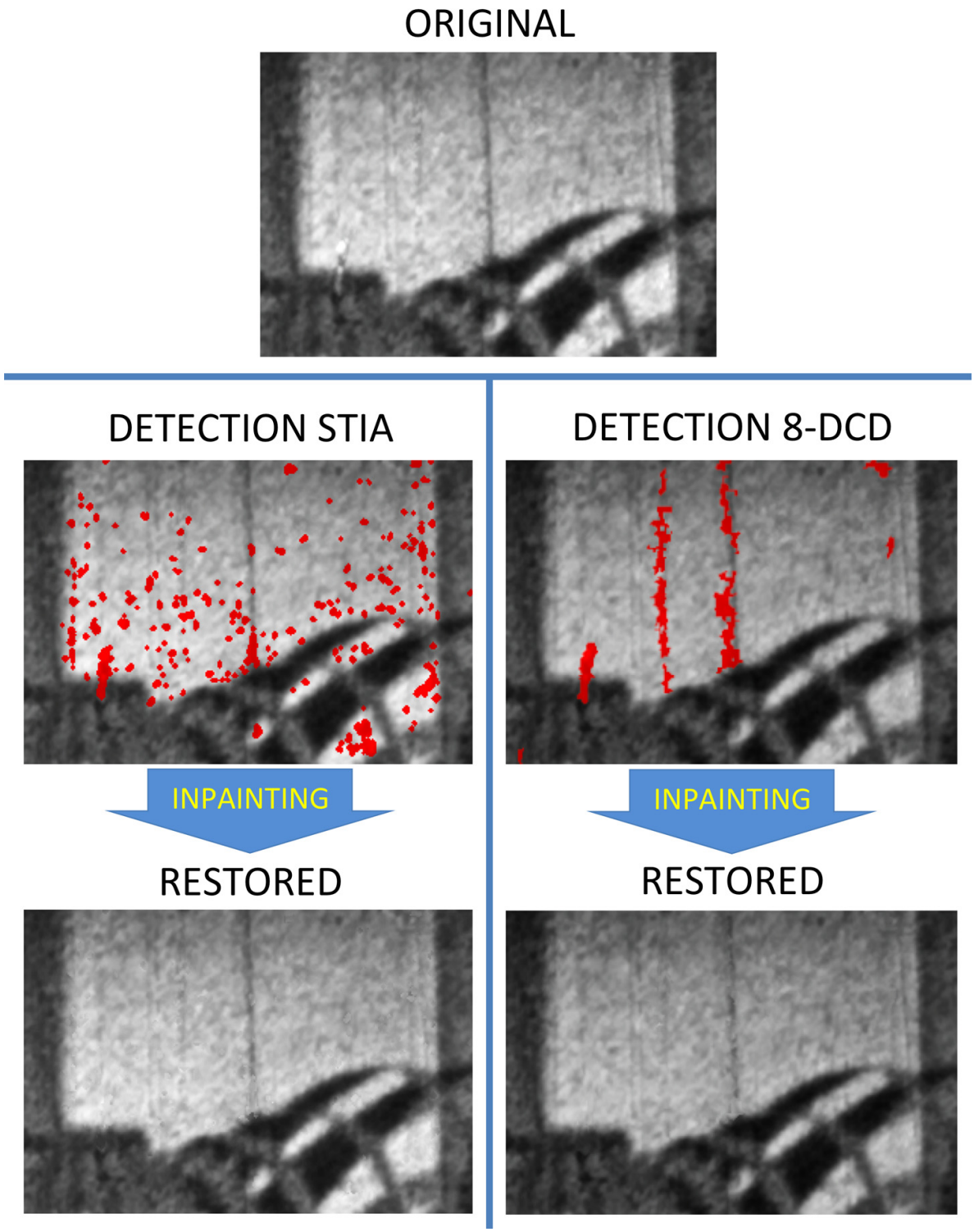

Figure 9.2.11: Comparison between STIA and 8-DCD - the case of vertical scratches

Chapter 10

Conclusions

The present study was set out to develop an effective method for the automatic detection of dust and scratches on digital reproductions of photographic film.

In today's digital restoration, the most effective methods for flaw detection use infrared radiation (e.g. Digital ICE) and spatio-temporal image analysis. The usage of infrared radiation has the advantage of being effective both for still images and motion pictures, but it has the disadvantage that it only works for dye-based material. The spatio-temporal image analysis is quite cheap, as no special scanning hardware is required; it works on all kind of one-frame flaws (the method is not deceived by copied flaws, but it is deceived by vertical scratches, as these appear in the same place in multiple frames). However, this method is not applicable on still images, it is only completely effective on quite homogeneous areas of the scene, and it is limited due to motion in the scene.

In the present thesis, we defined and analyzed in detail a group of methods for 'optical' flaw detection applicable on any type of transparent photographic material (silver-based as well as dye-based material, still images as well as moving images). The term 'optical' refers to the fact that the methods we considered seek physical evidence of the presence of foreign bodies or irregularities on the film. This makes it possible to avoid the typical digital artifacts produced by 'non-optical' methods, for which certain elements of the scenes are obliterated just because they resemble dust grains or scratches. In the case of flaws impressed in the new film during the process of copying, however, it has to be taken into account that these flaws are not in any case detectable with an optical method.

A deep understanding of the optical phenomena involved in the interaction between photographic film and light provided the scientific background necessary to develop effective optical methods. With this in mind, we devoted a considerable part of the laboratory activity to defining an appropriate model of the film-light interaction. We investigated the possible types of illumination of a film, exploring different light qualities and geometric illumination manners, and we analyzed the directional properties of the emerging fraction for

the reflective, transmissive and scattering components. This was the occasion to appreciate the countless different appearances of the photographic film and the different features that could be emphasized according to the illumination technique adopted. We made a particular effort to investigate the Callier effect (the variation in contrast and sharpness of different images of a photographic film produced with different degrees of light collimation), which was studied quite extensively in the first half of the 20th century, but then fell into obscurity in the second half.

In the context of *Heritage science*, the present dissertation places itself among *Optics* and *Digital technologies*; a considerable part of the research activity was focused on the development of effective image processing for our purposes. Moreover, *Computational photography* methods were explored to extend the capabilities of 'classical' digital photography.

Eventually, three different effective methods were identified for automatic flaw detection on photographic film. We called them:

- *Polarized Dark-Field* (**PDF**)
- *Collimation-Computational Detection* (**CCD**)
- *Direction-Computational Detection* (**n-DCD**)

PDF detects the flaws using an image acquired in a polarized dark-field setup. The combination of polarizing filters with dark-field illumination for digital film restoration had never been proposed before 2010 [11].

CCD entails the acquisition of two images in directed and diffused bright-field setups and the extraction of the differences between the images. This method has some conceptual similarities with a method patented in 2007 [44], but the setup of the acquisitions and the elaboration of the images are totally different.

n-DCD entails the acquisition of **n** images in dark-field setups with different directions of illumination and the extraction of the differences between the images. No documentation reports the use of a similar method for dust and scratch detection on photographic film.

A specific experiment was made to evaluate and compare the performances of the three methods identified; the experiment showed that flaw detection was quite successful for all the three methods, although it was better for **CCD** and **n-DCD** than for **PDF**. The results of this last experiment, together with our reflections on the state-of-the-art of digital restoration, led us to consider **n-DCD** as the most innovative and promising technique among those presented.

The **n-DCD** was then compared with the most effective traditional methods: namely, Digital ICE and spatio-temporal image analysis (STIA). For these experiments, an eightfold acquisition was adopted for the direction-computational detection (**8-DCD**).

The comparison with Digital ICE showed that the traditional method works better for dust grains, while **n-DCD** works better for scratches (sometimes it is even too sensitive to superficial scratches); in particular, when a scratch is very deep, Digital ICE often fails, while on the other hand, **n-DCD** generally correctly detects the scratch.

The comparison with STIA highlighted the main weakness of every optical method (like **8-DCD** is): whenever a flaw is a copied flaw, a missed detection is inescapable. In addition, the comparison highlighted the main weakness of STIA: when the motion in the scene is too complex to be compensated, the software produces artifacts. Moreover, STIA is deceived by the random movement of film grain from frame to frame, and as a result, the film grain is erroneously washed out.

There are pros and cons for both STIA and **8-DCD**. However, it is important to note that **8-DCD** avoids false detections better; in the framework of archival film restoration, it is important to keep alterations to the original information to a strict minimum, and thus missed detections are preferable to false detections.

In summary, the experimental part demonstrated that the Direction-Computational Detection (**n-DCD**) is a very effective method for automatic detection of flaws in the digital reproductions of photographic film, and it works well on any type of transparent photographic material. However, it is impossible to find a solution that is effective for all types of local flaws; a comprehensive automatic flaw detection needs to involve and cleverly combine different methods, each of them detecting a specific class of flaws.

Appendix A

Principal Component Analysis

Principal Component Analysis is a statistical technique that provides the linear transformation to be performed on a certain data set in order to minimize its redundancy (measured as covariance) and maximize the amount of its information (measured as variance). This allows representing data in a more efficient way, highlighting simple underlying structures from complex data sets. One of the most important features of PCA is that of being completely non-parametric: given a certain data set, the outcome is unique and independent of the user. PCA has been successfully used in image processing, particularly in pattern recognition and compression; its typical procedure in image processing is described briefly in the following text.

Let us assume to have a set of M digital images with the same format and the same pixel dimension ($a \star b = N$ pixels) representing different acquisitions of the same subject. According to the characteristics of the image acquisitions, each image represents a certain attribute of the subject which is observed; the images are rendered in 1-D vectors by concatenating their a rows one after the other. The values of the N pixels of the M images are then arranged in a NXM matrix (A.0.1). Precondition for the validity of PCA is that the number of observations N has to be a lot higher than the number of attributes M.

$$\mathbf{A} = \begin{bmatrix} a_{1,1} & a_{1,2} & \dots & a_{1,M} \\ a_{2,1} & a_{2,2} & & \\ a_{3,1} & a_{3,2} & & \\ \vdots & & \ddots & \vdots \\ a_{N,1} & & \cdots & a_{N,M} \end{bmatrix} \tag{A.0.1}$$

The covariance matrix is then calculated; this is the symmetric square M-by-M matrix that contains the covariances between the images.

$$\mathbf{C} = \begin{bmatrix} var_1 & cov_{1,2} & \dots & cov_{1,M} \\ cov_{2,1} & var_2 & & \vdots \\ \vdots & & \ddots & \\ cov_{M,1} & \cdots & & var_M \end{bmatrix} \tag{A.0.2}$$

Afterwards, the covariance matrix is diagonalized; this entails finding the square M-by-M matrix $\mathbf{P}$ such that

$$\mathbf{P}^{-1}\mathbf{C}\mathbf{P} = \begin{bmatrix} \lambda_1 & 0 & \cdots & 0 \\ 0 & \lambda_2 & 0 & \vdots \\ \vdots & 0 & \ddots & 0 \\ 0 & \cdots & 0 & \lambda_M \end{bmatrix} \tag{A.0.3}$$

The matrix $\mathbf{P}$ (A.0.4) that diagonalizes the covariance matrix $\mathbf{C}$ (A.0.2) can be found through an Householder reduction to tridiagonal form [85] and a QL algorithm with implicit shifts [86]. The M columns of the matrix $\mathbf{P}$ express the eigenvectors:

$$\mathbf{P} = \begin{bmatrix} EV1_1 & EV2_1 & \cdots & EVM_1 \\ EV1_2 & EV2_2 & & \vdots \\ \vdots & & \ddots & \\ EV1_M & \cdots & & EVM_M \end{bmatrix} \tag{A.0.4}$$

The eigenvectors ($\mathbf{EVi}$) are mutually orthogonal and their elements are the weights of the linear combination of the observed attributes which accounts for a maximal amount of variance in the data set. The data set $\mathbf{A}$ (A.0.1), which is expressed with the observed attributes, can be else expressed in the new reference system defined by the eigenvectors. The new values $\mathbf{D}$ are given by

$$\mathbf{D} = (\mathbf{P}^*\mathbf{A}^*)^* \tag{A.0.5}$$

For example the data projected on the first eigenvector are given by

$$\mathbf{D1} = \begin{bmatrix} \mathbf{EV1_1} \star \mathbf{A_{1,1}} + \mathbf{EV1_2} \star \mathbf{A_{1,2}} + \cdots + \mathbf{EV1_M} \star \mathbf{A_{1,M}} \\ \mathbf{EV1_1} \star \mathbf{A_{2,1}} + \mathbf{EV1_2} \star \mathbf{A_{2,2}} + \cdots + \mathbf{EV1_M} \star \mathbf{A_{2,M}} \\ \vdots \\ \mathbf{EV1_1} \star \mathbf{A_{N,1}} + \mathbf{EV1_2} \star \mathbf{A_{N,2}} + \cdots + \mathbf{EV1_M} \star \mathbf{A_{N,M}} \end{bmatrix} \tag{A.0.6}$$

As every projection of the data on the eigenvectors is, $\mathbf{D1}$ is a 1-D vector with dimension N and can be transformed in a 8-bit image by arranging its values in a rows and b columns ($a \star b = N$ pixels), by shifting and rescaling them between 0 and 255 and by rounding the values to the closest integer.

$$\mathbf{I1}_j = round\left(\frac{\mathbf{D1}_j - min(\mathbf{D1})}{max(\mathbf{D1}) - min(\mathbf{D1})} * 255\right) \tag{A.0.7}$$

But let us consider again the matrix $\mathbf{P}$ (A.0.4) and the corresponding diagonal matrix $\mathbf{P}^{-1}\mathbf{CP}$ (A.0.3); the values $[\lambda_1, \lambda_2 ... \lambda_M]$ in the diagonal of $\mathbf{P}^{-1}\mathbf{CP}$ are the eigenvalues of the eigenvectors $[\mathbf{EV1}, \mathbf{EV2} \ldots \mathbf{EVM}]$. By sorting the eigenvectors in order of decreasing eigenvalue, we obtain a rank of importance; the eigenvectors on top of the list are called "Principal Components" of the observed data set. The first principal component accounts for as much of the variability in the data as possible and each succeeding component accounts for as much of the remaining variability as possible.

In case PCA is used to reduce the dimensionality of the data set, a sub-set of eigenvectors is selected, considering the information of the remaining eigenvectors of little importance or just noise.

$$\mathbf{Q} = \begin{bmatrix} EV1_1 & \cdots & EVR_1 \\ EV1_2 & & \vdots \\ \vdots & \ddots & \\ EV1_M & & EVR_M \end{bmatrix} \tag{A.0.8}$$

In this case, rather than the matrix $\mathbf{P}$ (A.0.4), the smaller matrix $\mathbf{Q}$ (A.0.8) with the R selected eigenvectors as columns is used to express the data set.

$$\mathbf{E} = (\mathbf{Q}^* \mathbf{A}^*)^* \tag{A.0.9}$$

The matrix $\mathbf{E}$ (A.0.9) defines R images, which is a sub-set of the M images defined by $\mathbf{D}$: namely, the sub-set with the highest variance.

Appendix B

Contribution of the IVRG-EPFL

The project 'Dust BW: Detection of dust and scratches on photographic silver-halide (black/white) material by polarized dark-field illumination' was carried out with the partnership of the Images and Visual Representation Group of the EPFL (Ecole Polytechnique Fédérale de Lausanne); the present chapters reports the results of this important contribution to the research project [16].

B.1 Description of the dataset

A processed 35mm silver-based film with a speed of $400ASA$ was selected. Two frames of the film were exposed with the same complex test scene and, after processing, they have been artificially scratched and spread with dust on their wet surface (ensuring that the dust grains stick to the surface); at the end of this procedure, one sample was 'severely damaged' and the other was 'slightly damaged'.

A cardinal acquisition was carried out for the two samples recto and verso, in a P-polarized and a S-polarized dark-field setup, using three different angles between the collimated light beam and the optical axis (namely $15°$, $45°$ and $75°$), and using three different types of sources (namely a red, a green and a blue LED); the total number of acquired polarized dark-field images is 288. The two samples were also acquired recto and verso in bright-field.

B.2 Description of the method

The experiment was arranged following the criteria described in sections 6.2.2 and 8.2, in order to find the parameters of the setup (side of the film, color and polarization of light, as well as incident angle) that create the most favorable conditions for subsequent

flaw detection and removal. By the nature these images have been taken, there might be misalignments between the cardinal images (only S, N, and E, W, are aligned), and the direct light image. Once aligned, we apply a Principal Component Analysis (PCA) to the four cardinal images. By computing various thresholds on (combinations of) the first four eigenvectors, we identify flaws. Comparing our detection-mask with a manually created ground-truth, allows us to find the physical parameter combination that yields the most promising (physical) parameter combinations. In the following, we detail the different parts of the method.

Image registration

The input to our method is always a (potentially unaligned) quadruple of images (cardinal images) that were taken using the same parameters, only changing the direction of light provenance (N, S, E, and W). The images were taken such that it is likely that the S, N and E, W images, as well as the direct light image, are not aligned because the camera and film were moved in between. In order to align all the images, we first compute a transformation matrix $T_{E,S}$ that transforms the E and W image to the reference S (the N image is already aligned with S). We then compute another transformation matrix $T_{S,D}$ that transforms the four aligned cardinal images to the direct light image. We compute both transformation matrices using scale-invariant feature transform (SIFT) including outlier rejection (RANSAC). In other words, the transformation matrices are homographies, which are nicely suited to this type of problem.

Principal Component Analysis

Now that all images are aligned, we perform a principal component analysis (PCA) on the four cardinal images, and compute the eigenvectors. The idea behind this is that ideally, the only difference between the four images is the shadows because of the different directions of light. The first eigenvector expresses the spatial variability of the image. The second to fourth eigenvector emphasize the differences between the cardinal images due to the flaws present on the film surface.

Detection-mask

The next step is to create the detection-mask. We do so by computing three different masks, that are then combined together.

The first one is based on the first eigenvector, in which most of the flaws due to dust are very bright. By computing the location to the right of the large peak in the histogram of the first eigenvector, we are able to mark those flaws.

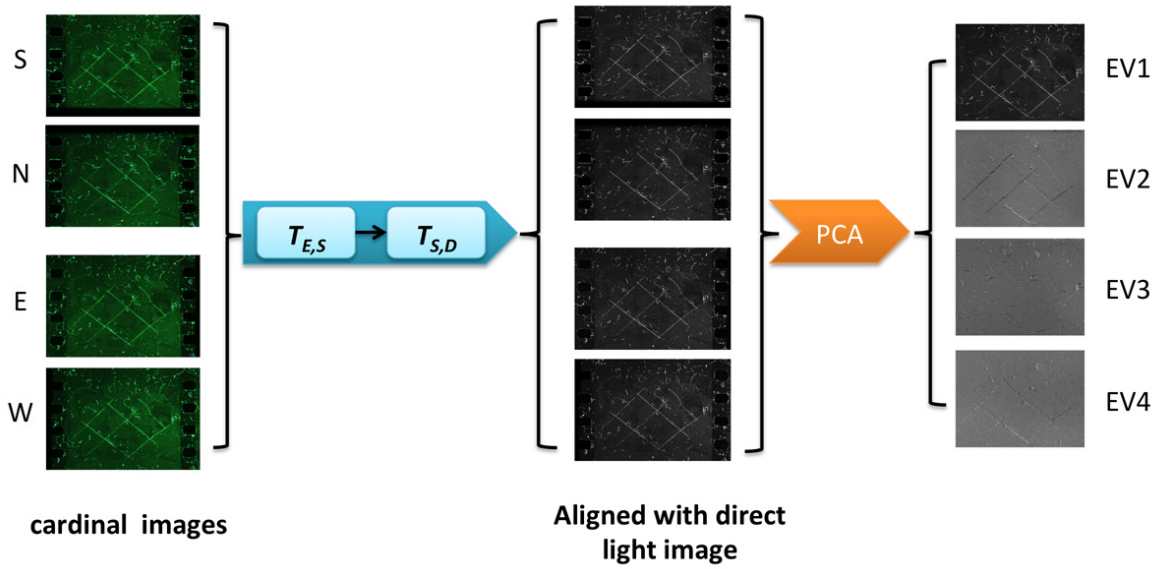

Figure B.2.1: Image registration and PCA

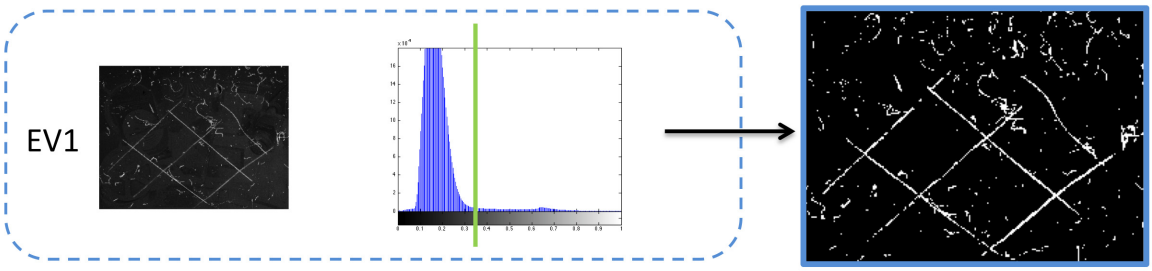

Figure B.2.2: Creation of the first partial detection-mask

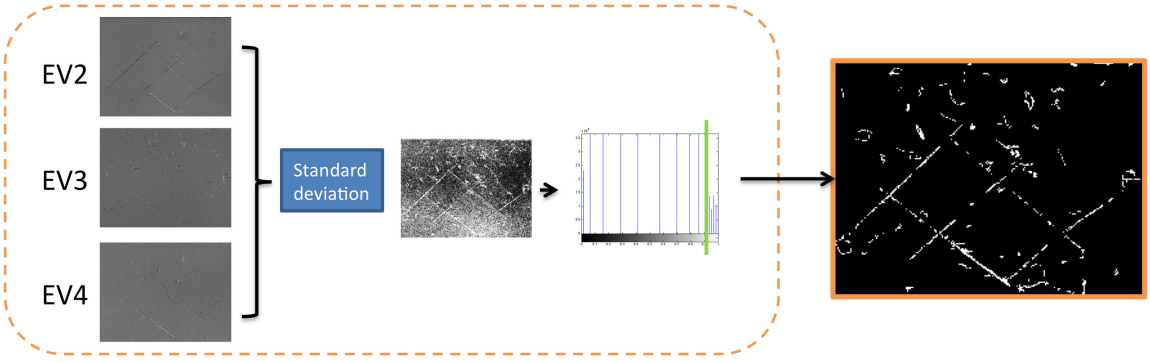

Figure B.2.3: Creation of the second partial detection-mask

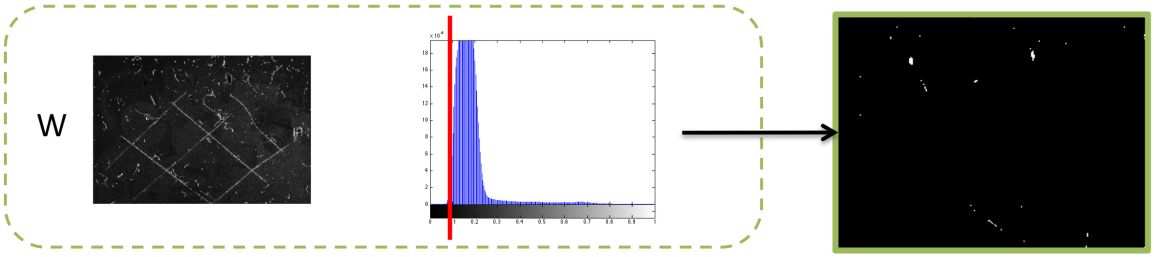

Figure B.2.4: Creation of the third partial detection-mask

For the second mask, we compute the standard deviation between the second to the fourth eigenvector. We then equalize the histogram and put the threshold at a normalized value of 0.95, and label everything as "flaw" that is larger than this value. It is expected that this threshold will vary depending on the input image.

The third threshold is used to capture the flaws where the whole photo-reactive layer of the film has been scratched off, which appears black in any of the cardinal images. We are able to detect those flaws by putting a threshold on the left of the peak in the histogram.

The last step is to put the three partial detection-masks together to the final detection-mask:

Evaluation

In order to evaluate the computed detection-masks, we manually labeled ground-truths of the film. We compare our detection-masks on a pixel-by-pixel basis with the ground-truth. It is worth mentioning that we are not primarily interested in the overall accuracy, but rather in the percentage of true positives we find, while keeping the false positives as low as possible. The reason for this is that the flaws make only a small part of the image, and hence not labeling anything as "flaw" would result in a very high accuracy (over 95 % for severely scratched images).

Best parameters

We applied our method on all cardinal images. Below, we show the plots of the true positives found for the recto images, both slightly and severely damaged. On the x-axis, we show the Red, Green, and Blue light, and on the y-axis the angle of incident light in descending order, both for horizontal and vertical polarization, and the z-axis shows the percentage of true positives found.

One can see that the results are generally worse using red light. Another, maybe surprising fact is that the results are significantly worse for the slightly damaged images. The reason

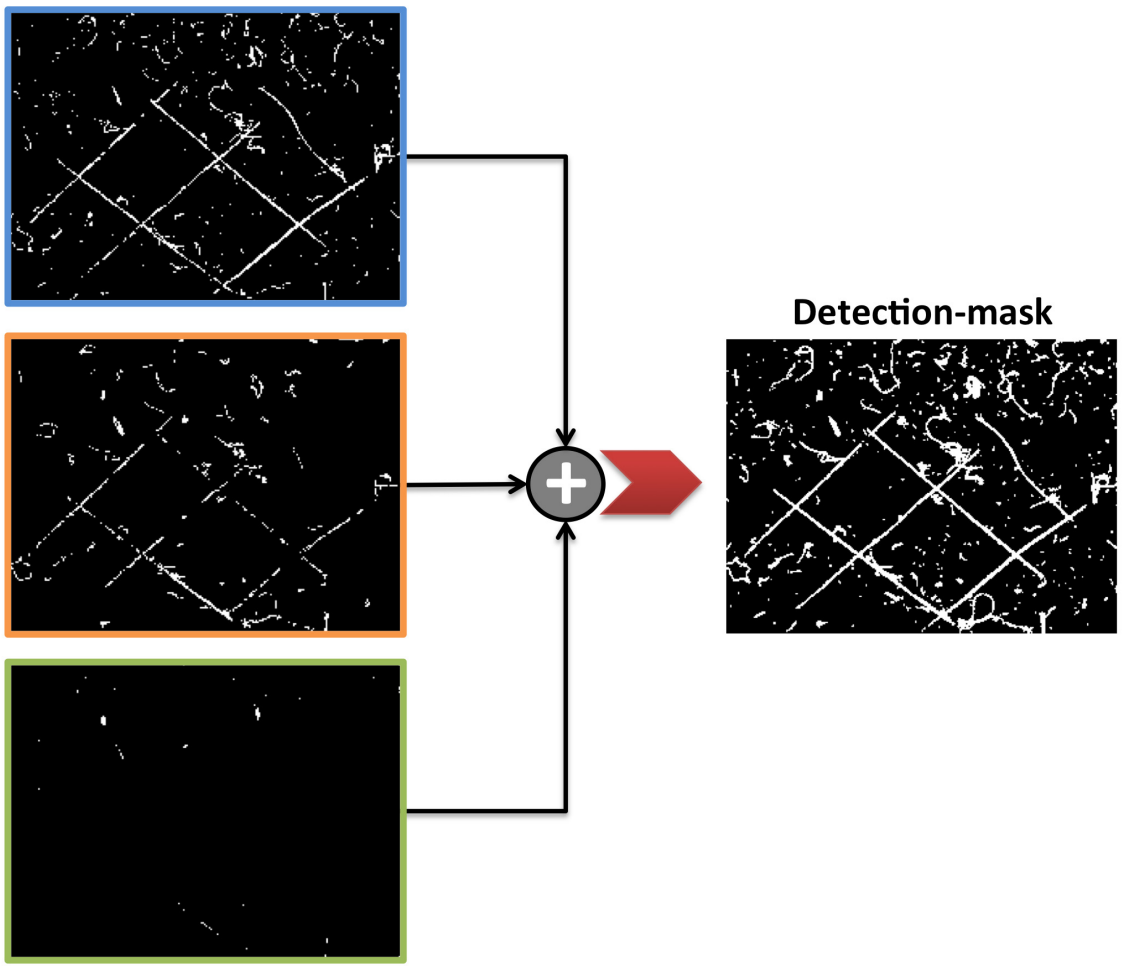

Figure B.2.5: Creation of the final detection-mask

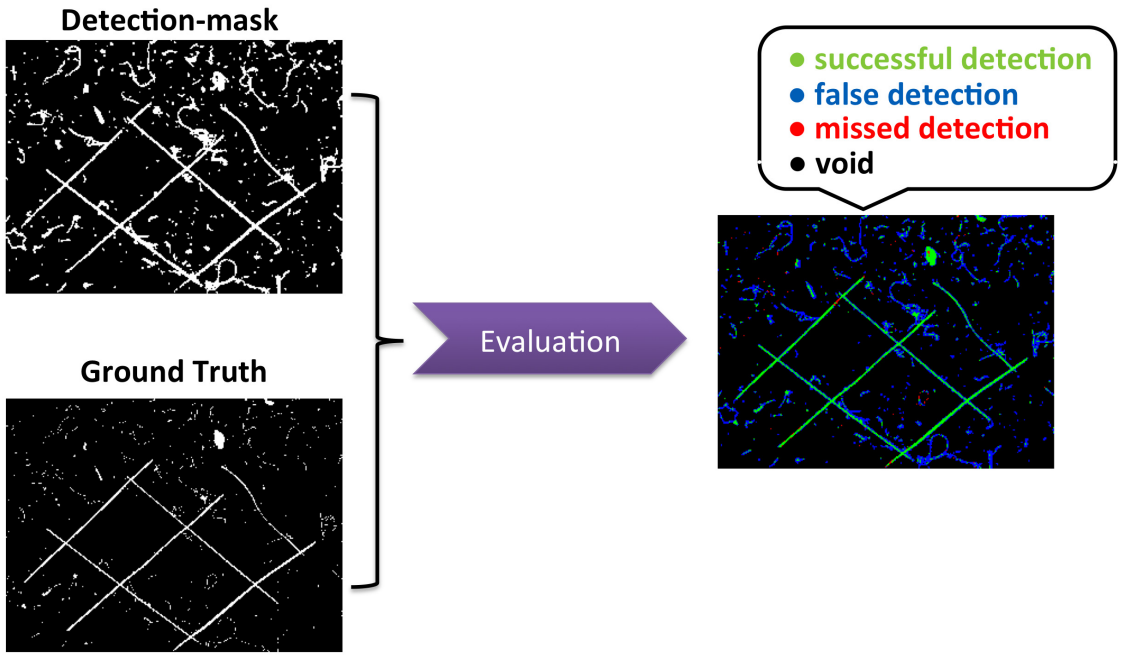

Figure B.2.6: Evaluation of detection

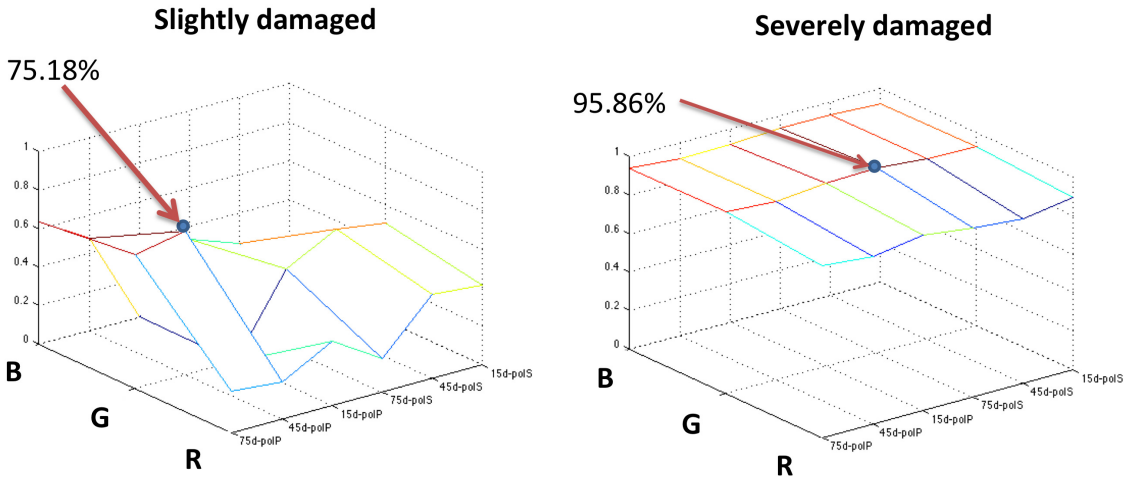

Figure B.2.7: Identification of the best parameters

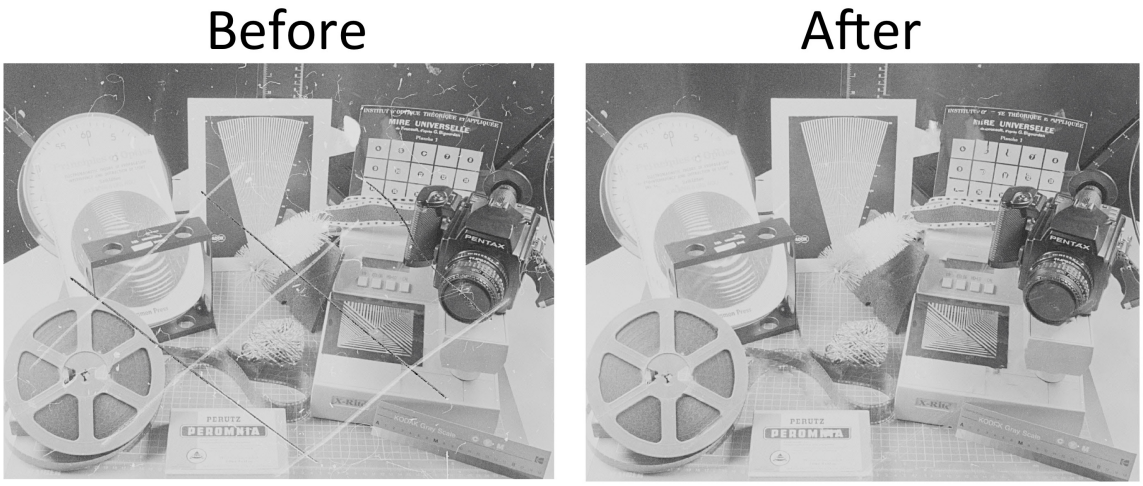

Figure B.3.1: Inpainting

for this is that there are very few flaws in that image, and we are missing some very thin, long flaws that account for a big part of the flaw. In general, best results are obtained for green light, and incident angle of 45 or 75 degrees. As for the side (recto or verso), we need more images in order to see whether this influences the result.

B.3 Outlook

Different flaw detection

We used a very simple thresholding method for detecting the flaws. The reason is that for this first experiment, the physical set-up was primarily tested. In the next step, we will evaluate more sophisticated methods once we have more images.

Inpainting

The detection-mask we obtained in the last part will be used to identify the parts that need to be corrected. We will investigate several inpainting methods in order to find the one that is best suited to our needs; for demonstration, we used the detection-mask with the highest true positive percentage and used Adobe Photoshop CS5's inpainting method (content aware filling) in order to remove the flaws.

Appendix C

Glossary

Attenuance - Physical quantity that defines the image impressed in the emulsion. J_0 is the luminous flux measured by a light detector in the absence of the film and J_1 is the luminous flux measured in the presence of the film. The attenuance is defined as $D = \log {}^{J_0}/_{J_1}$. The measured light is attenuated due to the depletion of the rays into the film (absorption) and due to their deviation in directions that the image detector cannot collect (scattering).

Bidirectional Scattering Distribution Function (BSDF) - For a fixed point x of a surface, let dE_i be the irradiance arriving on the surface from an infinitesimal cone $d\sigma$ around a particular direction ω_i ($L_i(\omega_i)\, d\sigma^{\perp}(\omega_i)$) and let dL_0 be the consequent radiance leaving the surface in another direction ω_0 ($dL_0(\omega_0)$). For a given combination of ω_i and ω_o, under normal circumstances, the ratio between the leaving radiance dL_0 and the incident irradiance dE_i is constant: the BSDF is the function that defines the ratio $\frac{dL_0}{dE_i}$ for all the pairs ω_i and ω_o.

Callier effect - When a condensed bright-field illumination setup is used, a crisp image is obtained, in which film grain is emphasized together with dust and scratches. On the other hand, when a diffused bright-field is adopted, the image has less sharpness and contrast, however blemishes on the film are much less visible. The variation of the appearance of images produced by a photographic film with different manners of illumination, is known as '*Callier effect*'.

Collimation-Computational Method - A method for flaw detection developed in this thesis. The method consists in acquiring two images of a photographic film (one

in a condensed bright-field setup and another one in a diffused bright-field setup) and then extracting their differences through Principal Components Analysis.

Computational photography – The acquisition of multiple images of the same subject, and the combination and manipulation of them in order to extend the capabilities of digital photography.

Connected component labeling – Connected groups of pixels that all have the same value in a binary image are individually labeled, so they can be separately manipulated, displayed, or modified.

Dark-field – Special illumination geometry used in microscopy. The sample is illuminated obliquely so that no directly transmitted light is collected by the optical system; light is collected only for elements of the sample that scatter light. Such an arrangement is useful to emphasize structures, shape irregularities and impurities in a sample.

Depolarization – Electromagnetic scattering by small particles can produce light with polarization characteristics different from those of the incident beam. In particular, when illumination is fully linearly polarized, the scattered light may become partially or totally unpolarized; the 'depolarization' can occur even if the scattering particles are not optically active.

Detection-mask – The outcome of flaw detection, which is a binary image that expresses the 'hard' classification of the pixels into the two categories "normal" or "flawed".

Digital ICE – Technology for flaw detection on color films. Acquisition of an additional infrared channel together with the visible color channels; over 850 nm, dye-based photographic film is mostly transparent to infrared radiation (no matter what image the film contains) and, conversely, dust and scratches often entail opacity; therefore, these flaws are recorded in the IR channel as definite marks on an homogeneous background.

Direction-Computational Method – A method for flaw detection developed in this thesis. The method consists in acquiring a set of images of a photographic film with different directions of illumination and then extracting the differences through Principal Components Analysis.

Flaw detection - Locating the flaws in the digital reproduction by converting the image data into descriptive labels that classify all the pixels as "normal" or "flawed". The classification is said to be "hard" if it only creates two categories, while is said to be "soft" if it attributes a credibility value to each pixel. The categorization assists the reconstruction stage by indicating exactly where the restoration is necessary and thus preventing elements of the photographic image of the emulsion from being obliterated. The result of the 'hard' classification is a binary image referred to as the 'detection-mask'.

Flicker - Unintended visible variation in the global brightness or color of a motion picture film from one frame to the next.

Ground-truth - Binary image that indicates the "true" flaws of a film.

Image registration - The transformation necessary to guarantee that, when images of the same subject have different viewpoints and their data need to be compared or integrated, equivalent pixels in the different images correspond to the same point of the subject (i.e. they have the same coordinate system).

Matthews Correlation Coefficient - Number that measures the quality of a binary classification. This number spans from -1 to 1 and takes into consideration the number of successful, missed and false detections. The higher the MCC, the better the detection.

Optical detection - Often qualified as "hardware-assisted", as it requires the acquisition of a particular image with a special setup. Optical detection of flaws is carried out by relying on physical evidence of the presence of foreign bodies or irregularities on the film.

Polarized light analysis - Technique used in imaging to enhance specific elements of the sample. Two polarizing filters are used in polarized setups: one in front of the illuminating source (polarizer) and another in front of the imaging device (analyzer); the directions of polarization of the two filters are orientated orthogonally.

Prime-image - Term used to indicate the unprocessed images (single or multiple) acquired in the context of applying the procedures for flaw detection described in the thesis. A subsequent image processing transforms the prime-image(s) into the detection-mask.

Principal Component Analysis - Statistical technique that finds the linear transformation that has to be performed on a certain data set in order to minimize redundancy and maximize the amount of information.

Spatio-temporal Image analysis - In motion pictures, the illusion of movement is created by the fact that contiguous frames differ slightly; therefore, the high correlation between contiguous frames allows for detecting dust grains, dirt spots and similar flaws that appear on a single frame. When an element of a specific frame is not present in either the previous or in the subsequent frame, it is considered a flaw. The information from the adjacent frames can be used to fill in the detected flaw and, therefore, this method provides an effective solution for both detection and reconstruction.

Bibliography

[1] "The digital dilemma 2." The academy of motion pictures arts and sciences, Hollywood, CA-USA, 2012.

[2] 20 minutes, "Ilford serait sur le point de déposer le bilan." http://www.20min.ch/ro/, July 2013.

[3] M. J. de La Merced, "Eastman kodak files for bankruptcy." http://dealbook.nytimes.com, January 2012.

[4] R. Wright and A. Williams, "Archive preservation and exploitation requirements," survey, PRESTO - Preservation Technologies for European Broadcast Archives, 2001.

[5] J. Aldred, "Disney's snow white: The story behind the picture," *The Newsletter of the Association of Motion Picture Sound*, vol. 24, pp. 8–9, December 1993.

[6] P. van Roosmalen, J. Biemond, and R. Lagendijk, "Restoration and storage of film and video archive material," *Signal Processing for Multimedia*, pp. 167–191, 1999.

[7] S. Tilie, L. Laborelli, and I. Bloch, "Blotch detection for digital archives restoration based on the fusion of spatial and temporal detectors," in *Information Fusion, 2006 9th International Conference on*, pp. 1–8, 2006.

[8] K. Honeycutt, "Metropolis goes back to the future," *Hollywood Reporter*, 2010.

[9] CTS, "La restauration numérique des films cinématographiques," tech. rep., Commission Supérieure Technique de l'Image et du Son, 1997.

[10] B. Besserer and S. Boukir, "La restauration numérique des films cinématographiques," *Dossiers de l'audiovisuel*, no. 93, pp. 38–43, 2000.

[11] R. Gschwind, "Dust BW," in *JTS 2010 - Digital challenges and digital opportunities in audiovisual archiving*, (Oslo, N), Joint Technical Symposium, 2010.

[12] G. Trumpy, A. Wassmer, and R. Gschwind, "Dust BW: Detection of dust and scratches on photographic silver halide material by dark field illumination and crossed polarization," in *Proceedings of Electronic Imaging & the Visual Arts*, (Berlin, D), EVA, 2011.

[13] G. Trumpy, A. Wassmer, and R. Gschwind, "Detection of dust and scratches on photographic material by combining dark field illumination and crossed polarization," in *8th EOS Topical Meeting on Diffractive Optics*, (Delft, NL), European Optical Society, 2012.

[14] G. Trumpy and R. Gschwind, "Computational photography for dust and scratch detection on transparent photographic material," in *SMPTE 2012 Annual Technical Conference & Exhibition*, (Hollywood, CA-USA), Society of Motion Picture and Television Engineers, 2012.

[15] G. Trumpy, "Multi-directional illumination for automatic flaw detection on photographic film: the importance of being many," in *Proceedings of the Colour and Visual Computing Symposium 2013 (CVCS 2013)*, (Gjøvik, N), Institute of Electrical and Electronics Engineers, 2013.

[16] D. Rüfenacht, G. Trumpy, R. Gschwind, and S. Süsstrunk, "Automatic detection of dust and scratches in silver halide film using polarized dark-field illumination," in *2013 IEEE International Conference on Image Processing*, IEEE Signal Processing Society, 2013.

[17] M. Osterman, *The Focal Encyclopedia of Photography*, ch. History and evolution of Photography, pp. 23–176. Elsevier Inc., 4th ed., 2007.

[18] E. Theisen, "The history of nitrocellulose as a film base," *J. SMPTE*, vol. 20, pp. 259–262, March 1933.

[19] T. James, *The Theory of the Photographic Process*. Macmillan Publishing Co., 4th ed., 1977.

[20] J. A. C. Yule, *Principles of color reproduction, applied to photomechanical reproduction, color photography, and the ink, paper, and other related industries*. Wiley, 1967.

[21] J. Reilly, "Storage guide for color photographic materials." State University of New York Press, Albany, NY-USA, 1998.

[22] T. Vitale, "Film grain, resolution and fundamental film particles," October 2009.

[23] NFPF, *The film preservation guide: the basics for archives, libraries, and museums*. San Francisco, CA-USA: National Film Preservation Foundation, 2004.

[24] J.-L. Bigourdan, "Vinegar syndrome: An action plan." https://www.imagepermanenceinstitute.org, 2000.

[25] G. Di Pietro, *Silver Mirroring on silver gelatin glass negatives*. PhD thesis, University of Basel, 2002.

[26] R. Gschwind and F. Frey, "Restoration of faded color photographs by digital image processing," in *IS&T's 46th Annual Conference*, pp. 281–283, Society for Imaging Science and Technology, 1993.

[27] A. Swan, "Conservation of photographic print collections," *Library Trends*, vol. 30, no. 2, pp. 267–296, 1981.

[28] J. Sassoon, "Photographic meaning in the age of digital reproduction," *Archives & Social Studies: A Journal of Interdisciplinary Research*, vol. 1, March 2007.

[29] W. Benjamin, "Das kunstwerk im zeitalter seiner technischen reproduzierbarkeit: Drei studien zur kunstsoziologie." Suhrkamp Verlag, Frankfurt am Main (D), 1963.

[30] A. Kokaram, *Motion picture restoration: digital algorithms for artifact suppression in degraded motion picture film and video*. Springer, 1998.

[31] R. Bergman, R. Maurer, H. Nachlieli, G. Ruckenstein, P. Chase, and D. Greig, "Comprehensive solutions for removal of dust and scratches from images," *J. Electron. Imaging*, vol. 17, no. 1, p. 013010, 2008.

[32] R. Gschwind, L. Rosenthaler, A. Wittmann, W. Graff, and A. Gunzinger, "Restoration of old movie films by digital image processing," in *Care of Photographic, Moving Image & Sound Collections Conference* (S. Clark, ed.), (York, UK), pp. 150–155, 1998.

[33] M. Bertalmìo, "Strong-continuation, contrast-invariant inpainting with a third-order optimal pde," *IEEE Trans. Image Process.*, vol. 15, pp. 1934–1938, July 2006.

[34] V. Kwatra, I. Essa, A. Bobick, and N. Kwatra, "Texture optimization for example-based synthesis," *ACM Trans. Graph., SIGGRAPH 2005*, vol. 24, August 2005.

[35] FIAF, "Code of ethics." http://www.fiafnet.org, July 2013.

[36] P. Read and M. P. Meyer, *Restoration of Motion Picture Film*. Woburn, MA-USA: Butterworth-Heinemann, 2000.

[37] ARRI, "Wet gate." http://www.arri.com.

[38] L. Joyeux, O. Buisson, B. Besserer, and S. Boukir, "Detection and removal of line scratches in motion picture films," in *Proceedings of CVPR'99, IEEE Int. Conf. on Computer Vision and Pattern Recognition, Fort Collins*, pp. 548–553, 1999.

[39] R. Storey, "Electronic detection and concealment of film dirt," Tech. Rep. BBC RD 1985/4, BBC, February 1985.

[40] P. Schallauer, A. Pinz, and W. Haas, "Automatic restoration algorithms for 35 mm film," *J. of Computer Vision Research - MIT*, vol. 1, no. 3, pp. 60–85, 1999.

[41] O. Buisson, S. Boukir, and B. Besserer, "Motion compensated film restoration," *Mach. Vision Appl.*, vol. 13, pp. 201–212, 2003.

[42] N. P. Galatsanos and R. T. Chin, "Digital restoration of multichannel images," *IEEE Trans. Acoust., Speech, Signal Processing*, vol. 37, no. 3, pp. 415–421, 1989.

[43] A. D. Edgar, "System and method for image recovery." U.S. Patent No. 5,266,805, November 1993.

[44] T. W. Mead, "Optical scatter correction for film scanners." U.S. Patent No. 2007/0076275 A1, April 2007.

[45] R. J. D. Tilley, *Colour and Optical Properties of Materials*. Chichester, UK: John Wiley & Sons, 1999.

[46] C. F. Bohren and D. R. Huffman, *Absorption and Scattering of light by small particles*. New York, NY-USA: John Wiley & Sons, 1983.

[47] H. C. Van De Hulst, *Light scattering by small particles*. Mineola NY-USA: Dover Publications, 1981.

[48] M. Born and E. Wolf, *Principles of optics*. Oxford: Pergamon press, 1980.

[49] H. DeVoe, "Optical properties of molecular aggregates. I. classical model of electronic absorption and refraction," *J. Chem. Phys.*, vol. 41, no. 2, 1964.

[50] E. Zubko, D. Petrov, Y. Grynko, Y. Shkuratov, H. Okamoto, K. Muinonen, T. Nousiainen, H. Kimura, T. Yamamoto, and G. Videen, "Validity criteria of the discrete dipole approximation," *J. Appl. Optics*, vol. 49, no. 8, pp. 1267–1279, 2010.

[51] H. Dahl, H. J. Metz, and T. Wriedt, "Light scattering of silver halide crystals," in *Proceedings of the 3rd Workshop on Electromagnetic and Light Scattering* (T. Wriedt and Y. Eremin, eds.), Electromagnetic and Light Scattering – Theory and Applications III, (Bremen, D), pp. 51–58, Universität Bremen, 1998.

[52] M. Jonasz, *Principles, Methods and Application of Particle Size Analysis*, ch. Size, shape, composition, and structure of microparticles from light scattering. Cambridge University Press, 1991.

[53] M. Polyanskiy, "Refractive index database." http://refractiveindex.info, July 2013.

[54] J. Gu, R. Ramamoorthi, P. Belhumeur, and S. Nayar, "Dirty Glass: Rendering Contamination on Transparent Surfaces," in *Proceedings of Eurographics Symposium on Rendering*, June 2007.

[55] E. Veach, *Robust monte carlo methods for light transport simulation*. PhD thesis, Stanford University, CA-USA, December 1997.

[56] T. Kozasa, J. Blum, H. Okamoto, and T. Mukai, "Optical properties of dust aggregates," in *Astronomy and Astrophysics*, vol. 276, ch. Angular dependence of scattered light, pp. 278–288, EDP Sciences, 1993.

[57] M. Mishchenko and L. Travis, *Light Scattering from Microstructures*, ch. Polarization and depolarization of light, pp. 159–175. Springer-Verlag, 2000.

[58] N. Ghosh, A. Pradhan, P. K. Gupta, S. Gupta, V. Jaiswal, and R. P. Singh, "Depolarization of light in a multiply scattering medium: effect of the refractive index of a scatterer," *Phys. Rev. E*, vol. 70, pp. 066607–1–7, December 2004.

[59] S. E. Braslavsky, "Glossary of terms used in photochemistry, 3rd edition," *J. Pure Appl. Chem.*, vol. 79, no. 3, pp. 293–465, 2007.

[60] J. Altman, *The Theory of the Photographic Process*, ch. 17 - Sensitometry of black-and-white materials. Macmillan Publishing Co., 4th ed., 1977.

[61] "Preservation and reuse of film material for television," Tech. Rep. 3289, European Broadcasting Union, Geneva, CH, May 2001.

[62] A. Hornberg, *Handbook of Machine Vision*. Wiley, 2006.

[63] D. Keeling, "Optical design and aberrations," *Brit. J. Phot.*, vol. 119, no. 5837, 1972.

[64] C. Tuttle, "The relationship between diffuse and specular density," *J. Opt. Soc. Am.*, vol. 12, no. 6, pp. 559–565, 1926.

[65] J. G. Streiffert, "Callier q of various motion picture emulsions," *J. Soc. Mot. Pict. Engrs.*, vol. 49, pp. 506–522, December 1947.

[66] A. Callier, "Absorption and scatter of light by photographic negatives," *J. Phot.*, vol. 33, 1909.

[67] E. Hecht, *Optics*. Addison-Wesley, 2nd ed., 1987.

[68] G. Fossati, *From grain to pixel - The archival life of film in transition*. Amsterdam, NL: Amsterdam University Press, 2009.

[69] T. Zelenka, "Verfahren und vorrichtung zur erkennung von fremdkörpern und oberflächendefekten auf einer transparenten vorlage sowie zur korrektur von dadurch verursachten bildfehlern einer abbildung der vorlage." Deutsches Patent und Markenamt No. DE 101 37 340 A 1, February 2003.

[70] A. E. Battles, D. M. Bloom, D. K. Campbell, O. R. Herrera E., and D. J. Stavely, "Film scanner with dust and scratch correction by use of dark-field illumination." U.S. Patent No. 5,969,372 A, October 1999.

[71] R. Wallis, "An approach to the space variant restoration and enhancement of images," in *Proceedings of Symposium on Current Mathematical Problems in Image Science*, (Monterey, CA-USA), pp. 329–340, Naval Postgraduate School, November 1976.

[72] R. Pintus, T. Malzbender, O. Wang, R. Bergman, H. Nachlieli, and G. Ruckenstein, "Photo repair and 3d structure from flatbed scanners using 4- and 2-source photometric stereo," in *Computer Vision, Imaging and Computer Graphics. Theory and Applications*, vol. 68 of *Communications in Computer and Information Science*, Springer Berlin Heidelberg, 2010.

[73] B. Xiao, "Principal component analysis for feature extraction of image sequence," vol. 1, Computer and Communication Technologies in Agriculture Engineering (CCTAE), 2010.

[74] L. Shapiro and G. Stockman, *Computer Vision*, ch. 3- Binary Image Analysis. Upper Saddle River, NJ-USA: Prentice-Hall, 2001.

[75] P. Soille, *Morphological Image Analysis*. Berlin, D: Springer, 2003.

[76] P. Baldi, S. Brunak, Y. Chauvin, C. A. Andersen, and H. Nielsen, "Assessing the accuracy of prediction algorithms for classification: an overview," *Bioinformatics*, vol. 16, pp. 412–424, May 2000.

[77] R. C. Gonzalez, R. E. Woods, and S. L. Eddins, *Digital Image Processing Using MATLAB*, ch. Geometric Transformations and Image Registration, pp. 278–317. Gatesmark Publishing, 2nd ed., 2009.

[78] "Film specifications," tech. rep., Eastman Kodak.

[79] F. Heitger, L. Rosenthaler, R. von der Heydt, E. Peterhans, and O. Kübler, "Simulation of neural contour mechanisms: from simple to end-stopped cells," *Vision Res.*, vol. 32, pp. 963–981, November 1992.

[80] D. Coffin, "DCRAW version 9.19." http://www.cybercom.net/ dcoffin/dcraw/dcraw.c, June 2013.

[81] Knight Optical, "Polaroid type hn38 linear polarizer for visible radiation." http://www.knightoptical.co.uk, August 2013.

[82] G. B. Airy, "On the diffraction of an object-glass with circular aperture," *Cambridge Phil. Soc. Trans.*, vol. 5, pp. 283–291, 1835.

[83] J. Sanz, F. Merkle, and K. Wong, "Automated digital visual inspection with dark-field microscopy," *J. Opt. Soc. Am. A*, vol. 2, no. 11, pp. 1857–1862, 1985.

[84] K. Kreimeier, *The Ufa Story: A History of Germany's Greatest Film Company, 1918-1945*. Los Angeles, CA-USA: University of California Press, 1999.

[85] W. Press, S. Teukolsky, W. Vetterling, and B. Flannery, *Numerical Recipes in C*. New York, NY-USA: Cambridge University Press: The Art of Scientific Computing, 2nd ed., 1992.

[86] W. Press, S. Teukolsky, W. Vetterling, and B. Flannery, eds., *Numerical Recipes in Fortran 77: The Art of Parallel Scientific Computing*, vol. 1, pp. 472–475. New York, NY-USA: Cambridge University Press, 1992.